

2019-04-25

Megaripple Stripes

Gough, Tyler Robert

Gough, T. R. (2019). Megaripple Stripes (Master's thesis, University of Calgary, Calgary, Canada). Retrieved from <https://prism.ucalgary.ca>.

<http://hdl.handle.net/1880/110217>

Downloaded from PRISM Repository, University of Calgary

UNIVERSITY OF CALGARY

Megaripple Stripes

by

Tyler Robert Gough

A THESIS

SUBMITTED TO THE FACULTY OF GRADUATE STUDIES

IN PARTIAL FULFILMENT OF THE REQUIREMENTS FOR THE

DEGREE OF MASTER OF SCIENCE

GRADUATE PROGRAM IN GEOGRAPHY

CALGARY, ALBERTA

APRIL, 2019

© Tyler Robert Gough 2019

Abstract

This thesis incorporates field measurements, satellite imagery, and numerical modeling to explain the formation and evolution of a poorly understood and relatively undocumented longitudinal aeolian bedform pattern. The pattern consists of alternating streamwise corridors of megaripples separated by corridors containing smaller bedforms. This pattern, referred to herein as megaripple stripes, is observed at sites on Earth and Mars. Measurements from satellite imagery indicate a strong positive relation between the crosswind and downwind wavelengths of megaripple corridors. Field measurements of stripe morphology and grain size indicate a consistent pattern whereby the surface texture of the megaripple corridors is coarser than the intervening corridors of smaller bedforms. The amplitude and wavelength of features in the megaripple corridors are larger than the features in the smaller bedform corridors. The three-dimensional morphology and sediment sorting pattern of megaripple stripes was reproduced in a numerical model that incorporated two aeolian transport species: saltons and reptons. Simulations suggest striped pattern development is a self-organizing process resulting from grain size and topographic feedbacks that are sensitive to the bulk concentration and erosion probability of reptons. In the simulations, regular megaripples emerge from a high bulk concentration of reptons and impact ripples develop from a very low bulk concentration of reptons. Megaripple stripes emerge when the bulk concentration is intermediate between megaripple and impact ripple formation. Therefore, it is hypothesized that megaripple stripes develop in unimodal transport environments with supply-limited reptons. The nature and dynamics of reptons are largely determined by the wind regime, the grain size distribution, and by the grain density distribution in some environments. Repton behaviour, spanwise transport, and other relevant aeolian processes are discussed in relation to megaripple stripes.

Preface

This thesis is original, unpublished, independent work by the author, Tyler Gough.

Acknowledgements

Thank you to all who have helped me along the winding path of completing a thesis. First, thanks to Dr. Chris Hugenholtz for his encouragement and guidance. Chris, your enthusiasm for research and suggestions have made this process a valuable learning experience and a good deal of fun (most days). Second, thanks to Thomas Barchyn and Elena Favaro for providing ideas and tools which have been essential to this thesis. This thesis would not be complete without MGD, and I am grateful to Tom for developing the program and for his suggestions related to this research. Elena, your encyclopedic knowledge of department and University policies, as well as your willingness to take hours to talk out ideas with me have been invaluable. Third, many thanks to Paul Nesbit for his serving as tour guide, photogrammetry expert, and American English translator (“where is the washroom?”) during field work in California. Fourth, thanks to all others in the 922 research group for being outstanding colleagues and friends: Thomas, Maja, Andrew, Mo, Clay, Brynn, Adam, Eleanor, and Sarah. Fifth, thanks to my friends and family for being so understanding and supportive despite having only the roughest idea of what exactly it is I have been doing for the past two years. Finally, thanks to my partner, Hannah, whose patience and kindness I am eternally in awe of and grateful for.

Table of Contents

Abstract	ii
Preface	iii
Acknowledgements	iv
Table of Contents	v
List of Tables	viii
List of Figures	ix
List of Abbreviations, Symbols, and Nomenclature	xiv
Chapter 1: Introduction	1
1.1. Motivation and Objectives	1
1.2. Literature Review	1
1.2.1. Aeolian Research	1
1.2.2. Impact Ripples	3
1.2.3. Megaripples	5
1.2.4. Aeolian Sediment Transport Fundamentals	7
1.2.5. Aeolian Sediment Transport Thresholds	8
1.2.6. Spanwise Transport	11
1.3. Megaripple Stripes	12
1.3.1. Oceano Dunes and Dillon Beach, California, USA	13
1.3.2. Abra Pomez, Argentina	15
1.3.3. Paracas Peninsula and Ica Desert, Peru	15
1.3.4. Lut Desert, Iran	18
1.3.5. Longyanxia Reservoir, China	18
1.3.6. Walvis Bay, Namibia	18
1.3.7. Rabe Crater Dunes, Mars	23
1.4. Research Approach and Working Hypotheses	23
Chapter 2: Methodology	27
2.1. Overview	27
2.2. Morphometrics	28
2.2.1. Wavelength Measurements	28
2.2.2. 3D Reconstructions	29
2.3. Grain Size Measurements and Analyses	30
2.3.1. Oceano Dunes, California	31
2.3.2. Abra Pomez, Argentina	33

2.3.3. Grain Size Analyses	34
2.4. Numerical Modeling	38
2.4.1. Model Parameters	40
2.4.2. Evaluation of Model Verisimilitude and Comparison to Natural Megaripple Stripes	45
Chapter 3: Results	47
3.1. Overview	47
3.2. Wavelengths	47
3.3. Grain Size	49
3.3.1. Oceano Dunes, California	49
3.3.2. Abra Pomez, Argentina	53
3.4. Bedform Heights and Planform Morphology	58
3.5. Numerical Modelling	61
3.5.1. MGD Megaripple Stripes and Parameter Constraints	61
3.5.2. Parameters Affecting Megaripple Stripe Formation in MGD	62
3.5.3. Summary of Megaripple Stripe Formation in MGD	68
3.5.4. Spatial Autocorrelation and Megaripple Stripe Development	74
3.5.5. Morphometric Comparison of MGD and Oceano	77
3.6. Summary of Results	80
Chapter 4: Discussion	82
4.1. Overview	82
4.2. Megaripple Stripes – Corridor Types	82
4.3. Modelling of Megaripple Stripes	84
4.4. Repton Sources for Megaripple Stripes	86
4.5. Sorting Mechanisms	89
4.5.1. Sorting Mechanisms Observed in MGD	91
4.5.2. Quantifying Sorting Effects: A Random Walk and Markov Chain Approach	94
4.6. Megaripple Stripe Destruction: Oceano Case Study	102
4.7. Summary of Megaripple Stripe Formation and Development	103
4.8. Megaripple Stripe Classification	105
Chapter 5: Conclusion	108
5.1. Summary of Site Observations and Hypotheses	108
5.2. Future Work	110
References	112
Appendix A: Oceano Dunes Sample Grain Size Data	121
Appendix B: Repton Score	123

B.1. Meteorological Data.....	123
B.2. Repton Score Model.....	123
B.3. Repton Score Results	124

List of Tables

Table 1.1: Megaripple stripe locations. Terrestrial coordinates acquired from Google Earth based on the WGS84 datum. Martian location acquired from the HiRISE database, which uses the Mars 2000 GCS and MOLA for elevation.	12
Table 2.1: Example of MGD parameters used to reproduce megaripple stripes.	41
Table 2.2: Probabilities of a repton with $P(\theta)$ of 2/3 being at a given spanwise position after a given number of steps.	44
Table 3.2: Mean values from wavelength measurements of megaripple stripes from the field (Oceano Dunes) and imagery (all other locations).	48
Table 3.3: Aggregated grain size statistics from LPSA data for Oceano Dunes samples. All grain sizes presented are in μm . *Transition area samples were acquired at only two of four sampling sites. Although the grain sizes for the transition areas are smaller than the smaller bedform corridors in aggregate, the transition areas are coarser than the smaller bedform corridor samples from their respective sampling sites.	50
Table 3.3: Descriptive statistics of megaripple and smaller bedform corridors from photosieving of surface grains in Abra Pomez.	54
Table 3.4: Morphometrics acquired from measurements of the structure-from-motion DSMs generated at the Oceano Dunes megaripple stripes. *Note that the wavelength measurements for Oceano reported here do not match those reported in Table 3.1 because these measurements were acquired from different samples and by a different methodology.	58
Table 3.5: Morphometrics acquired from photogrammetry of the Oceano Dunes megaripple stripes and the MGD model outputs. *The wavelength measurements for Oceano reported here do not match those reported above because these measurements were acquired from different samples and by a different methodology.	80
Table 3.6: Relative metrics of wavelength and height for the Oceano Dunes and the MGD model.	80
Table 4.1: Generalized bedform formation table based on the type of aeolian transport occurring. Megaripple stripes are hypothesized to occur only when the transport environment is conducive to megaripple development, but reptons are in limited supply.	88
Table A.1: Summary of all 70 samples acquired from the Oceano Dunes. Grain sizes in μm	121

List of Figures

- Figure 1.1:** **A)** Photo of megaripple stripes, looking crosswind, at Oso Flaco at the southern end of the Oceano Dunes. Photo: Raleigh Martin. **B)** Megaripple stripes in Rabe Crater, Mars. Image: HiRISE PSP_002824_1355, NASA/JPL/University of Arizona. Arrows indicate assumed dominant direction of transport. 2
- Figure 1.2:** **A)** Overview of the northern portion of the Oceano Dunes Natural Preserve. The dominant winds come from the west-northwest. A large beach and foredune system are directly to the west of the dunes. **B)** Megaripple stripes and the field site visited in 2017. Numbers denote the four locations at which physical samples were acquired (see §2.3.1.). 14
- Figure 1.3:** Striped megaripples at Abra Pomez. Arrow indicates direction of dominant wind. As the pattern initiates upwind in **A**, megaripple crests extend almost entirely crosswind and the striped pattern is not yet very distinct. The striped pattern becomes more evident in **B**, and the megaripples have a distinct cusped shape. In **C**, the megaripple corridors begin to thin until further downwind the striped pattern fades almost entirely. 16
- Figure 1.4:** **A)** Large field of megaripples and megaripple stripes in the Ica Desert, Peru. Megaripple stripes are common in this region. Arrow indicates direction of dominant wind. **B)** Inset photo. The bottom of the image shows megaripples developing into stripes downwind. Note the cusped shape of the megaripples in the stripes. 17
- Figure 1.5:** **A)** Megaripple stripes in Iran develop in a large field of yardangs. Arrow indicates direction of dominant wind. **B)** As with megaripple stripes in Argentina and Peru, the stripes thin downwind and become smaller megaripples or impact ripples. **C)** The cusped shape of the megaripples and the regularity of the pattern in the Lut Desert closely matches that observed at the other locations. 19
- Figure 1.6:** **A)** Striped features in the Lut Desert identified as TAR analogs by Hugenholz and Barchyn (2017). **B)** These features do not have the cusped shape seen at other locations. The scale of these bedforms is also larger than other locations and there are no obvious bedforms in the corridors between larger bedforms. The crosswind corridor patterning suggests these features may be megaripple stripes. 20
- Figure 1.7:** **A)** Field of barchanoid dunes near the Longyanxia Reservoir, China. Megaripple stripes are found on many of the stoss slopes of the dunes. **B)** Inset image. The width of the megaripple stripes decreases downwind as the megaripples climb the dune. 21
- Figure 1.8:** **A)** Megaripple stripes develop on the stoss of several barchanoid dunes 8 kilometres south of Walvis Bay, Namibia. **B)** The pattern can be seen emerging into corridors after beginning as megaripples at the base of the dune and thinning out almost entirely at the crest of the dune. 22
- Figure 1.9:** **A)** Rabe Crater Dune Field, Mars. The bottom of the image is a large field of metre-scale bedforms. A large field of barchanoid dunes is present in the rest of the image, with several megaripple stripes present throughout the dune field. These megaripple stripes show a striking similarity to those found on Earth. **B)** Example of the megaripple stripe pattern with several alternating corridors of small and large bedforms. Figure 1.1B shows a close-up of these same features. As with the terrestrial locations, the megaripple corridors can be seen thinning out downwind. **C)** Example of individual corridors of megaripples, suggesting a differential grain size between these stripes and the surrounding bedforms. Image: HiRISE PSP_002824_1355, NASA/JPL/University of Arizona. 24

Figure 2.2: **A)** Overview of megaripple stripe pattern in the Rabe Crater dune field, Mars. Arrow indicates assumed dominant direction of transport. **B)** Inset photograph showing alternating pattern of megaripple corridors, C, and smaller bedform corridors, F. A spanwise wavelength, λ_s , is defined as the width of a pair of corridors. The two downwind transects show λ_c , where the transect spans three wavelengths, and λ_F , where the transect spans ten wavelengths over the same distance. (Image: HiRISE PSP_002824_1355, NASA/JPL/University of Arizona). 30

Figure 2.3: Example locations of sample acquisition for megaripple corridors (black), smaller bedform corridors (white), and transitional areas (grey) for sample acquisition. As noted in the text, several bedforms were used to gain a sufficient sample mass and representative sample. 32

Figure 2.3: **A)** Locations of the 43 images used for photosieving (23 from megaripple corridors and 20 from smaller bedform corridors). **B)** Example of a buffer and polygon-drawing method used for photosieving of a megaripple stoss slope image with a buffer diameter of 200 pixels. 35

Figure 3.4: Crosswind and downwind (megaripple corridor) wavelengths of megaripple stripes on Earth and Mars. A two-to-one crosswind-downwind wavelength ratio appears to exist for megaripple stripes. 49

Figure 3.5: **A)** Average D50 of depth samples acquired at four sampling sites at the Oceano Dunes. **B)** D50 values from 42 depth samples acquired from the megaripple and smaller bedform corridors at the Oceano Dunes. D50 values for each sample were rounded to the nearest multiple of 50. 51

Figure 3.3: Grain size curves for a series of megaripple stripe samples at the Oceano Dunes, California. **A)** Three samples acquired at depth from the stoss slopes and crests of bedforms from the megaripple corridors, smaller bedform corridors, and transitional area. Their combined distribution is also shown. **B)** Two samples acquired at the surface of bedforms in the same location as A) for the megaripples and smaller bedforms. 52

Figure 3.4: Probability density of grain sizes from photosieving for the megaripples, smaller bedforms, and all grains combined. 55

Figure 3.5: Distribution of sampling means rounded to nearest 0.2mm for 43 image samples acquired for the megaripple corridors (23 images) and smaller bedform corridors (20 images) at Abra Pomez, Argentina. 56

Figure 3.6: **A)** A global polynomial interpolation shows a downwind fining at Abra Pomez. Individual points represent photo locations and colour scheme represents the grain size (normalized so that 0 represents the mean and ± 1 is a standard deviation). The direction of fining trend closely matches that of the prevailing transport direction. **B)** Scatterplot of grain size as a function of northing for megaripples and smaller bedforms. R^2 values of 0.52 and 0.24 were found for the megaripples and smaller bedforms, respectively. **C)** Scatterplot of sorting index (§2.3.3.1.) as a function of northing. No relationship was found between the relative sorting and northing. 57

Figure 3.7: **A)** Orthomosaic of megaripple stripes at the Oceano Dunes sample site 3. Arrow shows assumed dominant transport direction. **B)** Sample of DSM from megaripple stripe site 3 at the Oceano Dunes. Inset from A). 60

Figure 3.8: **A)** Profile graph of megaripples and smaller bedforms extracted from DSM of stripes at Oceano Dunes, California. Transport direction is left-to-right. Overall, these results show that there are large

differences in ripple height and wavelength between corridor types. **B)** Inset of megaripple profile. The stoss and lee slopes are of approximately the same length. **C)** Inset of smaller bedform profile. The slopes are shallower, and the stoss slope is longer than the lee. Vertical exaggeration in **B)** and **C)** is 2, giving the same relative scale and allowing for easier comparison of their profiles. 61

Figure 3.9: Model space visualizations of simulations with 2–6% initial repton concentrations after 1000, 3000, 5000, 7000, and 9000 iterations. Representations of salton (yellow) and repton (red) slabs on the model surface. Transport is left-to-right. Megaripples do not develop at 2% and simple impact ripples migrate through the model space for the entire simulation. At 3%, a small corridor of megaripples has developed in the bottom of the model space after 9000 iterations. After 5000 iterations with a 4% concentration there is a large megaripple corridor. By the end of the model run, megaripples dominate the model space. With initial bulk concentrations of 5% and 6%, megaripples develop rapidly throughout the model space. 64

Figure 3.10: Percentage of repton slabs on the surface layer of the MGD model space for 10,000-iteration model runs with varying initial repton concentrations. Megaripple stripes developed with initial concentrations of 3, 3.5, and 4% initial concentrations. At 2%, only impact ripples develop. At 5% or greater, megaripples form rapidly and the megaripple stripe pattern does not emerge. These results show a coarsening over time that is consistent with the findings of Yizhaq et al. (2012a). Interestingly, there is a characteristic shape to the curves which resulted in megaripple stripe formation: a rapid initial increase followed by a brief plateau, followed by a second increase. 65

Figure 3.11: Model space visualizations of simulations with 4–36% repton erosion probability after 1000, 3000, 5000, 7000, and 9000 iterations. Megaripples do not develop at 4% and impact ripples migrate over a bed of reptons. Megaripple stripes develop in all other simulations. Larger erosion probabilities increase the rate at which megaripples develop. The simulation for 36% could not be completed because the height of the megaripples exceeded the maximum dimension of the model space after 7150 iterations. All simulations run with identical parameters, except repton erosion probability (Table 2.1). 66

Figure 3.12: Model space visualizations with 0%, 50%, and 100% spanwise transport probability for reptons. Megaripple stripes develop in all simulations. All simulations run with identical parameters, except repton spanwise transport probability (Table 2.1). 67

Figure 3.13: Scatterplot of megaripple stripe emergence in the MGD model space against the probability of spanwise transport for repton slabs. A weak negative relationship with R^2 of 0.20 is found. 67

Figure 3.14: Initial impact ripple development in MGD through 1200 iterations. Repton % reflects the concentration of repton slabs on the surface layer of the model space. **A)** The model begins with a random featureless distribution of reptons and saltons. **B)** After 300 iterations, the percentage of reptons begins to increase. Small features analogous to proto-ripples begin to emerge at this stage. **C)** Well-defined ripples begin to emerge, and small local concentrations of reptons are apparent. **D)** Ripples continue to develop and increase in wavelength. After only 1200 iterations, repton surface concentration has almost tripled. 69

Figure 3.15: Megaripple nucleation site emergence in MGD. **A)** Impact ripples remain the dominant feature of the model space, and repton concentrations have only increased by 0.8% over the past 800 iterations. **B)** Impact ripples continue to migrate in the model space, and repton concentration has increased slightly. **C)** A nucleation site has begun developing in the model space, indicated by the black arrow. The nucleation site has intersected the crestline of the impact ripple. **D)** Two nucleation sites are now present in the model.

The topmost nucleation site has expanded and the formation of a megaripple stripe has begun. 71

Figure 3.16: Megaripple stripe development and expansion in MGD. **A)** Megaripple stripe development continues from Figure 3.15D, and the surface concentration continues to increase. **B)** The megaripple stripe pattern is well developed at this stage, and distinct megaripple-type features have emerged in the model space and have started expanding crosswind. **C)** The crosswind expansion of megaripple stripes continues. **D)** The megaripple features have expanded and nearly overtaken all the smaller ripple features, nearly bringing an end to the megaripple stripe pattern in the model space. The surface repton concentration after 7400 iterations is 7.5 times greater than the initial value. 73

Figure 3.17: Final stages of megaripple stripe simulations in MGD. **A)** The corridor pattern is no longer extant and almost the entire model space is filled with megaripples. **B)** After a 10 000-iteration model run beginning with a featureless model space and only 3.5% reptons on the surface, large megaripples have developed and repton slabs cover a third of the surface layer. 74

Figure 3.18: Logs of the percentage of repton slabs present at the surface and the Moran's I of the surface layer for three MGD simulations. The simulations shown were run with identical parameters (Table 2.1), with the exception of repton spanwise transport. The spanwise transport probabilities used were no spanwise transport (black), 50% spanwise transport (red), and 100% spanwise transport (blue). 75

Figure 3.19: Model space visualizations of slab type and G_i^* for a 10 000-iteration simulation with a bulk concentration of 3.5% reptons. Megaripple stripes emerge when a local concentration of reptons develops. The G_i^* is interpreted a Z-score, where a value of ± 1 indicates a single standard deviation above/below the mean. The scale shown is representative for all outputs. 76

Figure 3.20: **A)** DSM of a megaripple stripe simulation after approximately 1.2 billion individual slab transport events (7500 iterations). **B)** Planview of the surface for the DSM shown in A). As with the megaripple stripes observed in Oceano and Argentina, the lowest point in the simulated megaripple stripes is also the trough of the megaripples. Arrows indicate transport direction. Compare to Figure 3.7. 78

Figure 3.21: **A)** Transect measurements of smaller bedform and megaripple corridors in MGD showing distinct differences in height and wavelength between corridor types. Note that the z dimension of slabs is one-tenth that of the x dimension. **B)** Inset of megaripple profile. The stoss and lee slope have lengths of approximately 30 and 40 slabs, respectively. **C)** Inset of smaller bedform profile. The convex curvature of the ripple is similar to that observed at the Oceano Dunes. Compare to Figure 3.8 above. 79

Figure 4.1: **A)** Barchanoid dunes and megaripple stripes in Rabe Crater. The megaripple stripes and megaripples have emerged in several locations directly downwind of avalanche slopes and/or from dune troughs. The megaripples extend for some distance and then fade. The dune troughs are likely sources of reptons, which rapidly decrease in availability as the megaripples climb the stoss slopes of dunes. Arrow denotes assumed dominant direction of transport. **B)** Inset image with hypothesized downwind decrease in reptons and thinning of the megaripple stripe pattern. These same processes can be seen occurring in the imagery of China (Figure 1.7) and Namibia (Figure 1.8). 88

Figure 4.2: Small-scale processes and sorting mechanisms occurring in the corridors of megaripple stripes. Red arrows indicate assumed rate of transport at different locations. Black arrows indicate spanwise transport caused by reptation. 94

- Figure 4.3:** Example of 10 random-walk slab paths through an idealized model space with no influences other than spanwise transport. 95
- Figure 4.4:** Comparison of an MGD simulation with initial repton concentration of 3.5% (same as shown in Figure 3.17) and Markov chain described in text. In the first 5000 iterations, the Markov chain is within 1.6% of the repton surface concentration measured in MGD. The disagreement between the two after approximately 5000 iterations is associated with megaripple stripe formation in the model space and the point at which topographic and shadow zone effects likely become more significant than the original bulk distribution and erosion probabilities. The Markov chain was adjusted to the MGD results so that one iteration of the chain was associated with 500 iterations in MGD. 101
- Figure 4.5:** **A)** View of the area where megaripple stripes are developing at the Oceano Dunes in 2011. **B)** The same location in 2017. A significant wind event or series of events likely caused the development and expansion of blowouts in the area. Although perhaps due to the different lighting and resolution of the two images, the image from 2017 appears to show fewer megaripple stripes than the 2011 image. **C)** Image of megaripple stripes and the recently developed blowout. **D)** The same blowout facing towards the coast and the foredune. 103
- Figure B.6:** Wind speed thresholds of the observed surface grain size distribution on the megaripple and smaller bedform corridors from photosieved data and the observed maximum daily gusts collected at an anemometer height of 1.6m by Bridges et al. (2015). 126
- Figure B.7:** Wind speed thresholds of the observed surface grain size distribution on the megaripple and smaller bedform corridors from LPSA data gathered from samples at megaripple stripe site C (1cm depth) and the observed maximum daily gusts collected by Bridges et al. (2015). These data offer some similarity to the findings of Adhikari (2017), who observed transport events occurring between 5.18 and 8.49m/s. 127
- Figure B.3:** Cumulative frequency of repton score distribution for the megaripple and smaller bedform data from Argentina. The area between the curves is a ‘behaviour gap’ that represents the difference in the nature of transport between corridor types. 128
- Figure B.4:** Cumulative frequency of repton score distribution for the megaripple and smaller bedform data from Oceano. The rapid rise of the smaller bedform curve shows that the majority of the surface grains in these corridors is likely to have their fluid thresholds exceeded by the maximum daily gusts on more than 90% of days. 129

List of Abbreviations, Symbols, and Nomenclature

- A:** Dimensionless parameter empirically determined by Shao and Lu (2000) which represents the interparticle forces between grains and has a value of 0.111
- CA:** Cellular Automata
- D_P:** Particle diameter
- DSM:** Digital Surface Model
- g:** Acceleration due to gravity
- GCS:** Geographic Coordinate System
- Gi*:** Getis-Ord spatial autocorrelation statistic (Getis and Ord 1992)
- GSD:** Grain Size Distribution
- h:** Bedform height, defined as the vertical distance between bedform crest (summit point) and trough.
- HiRISE:** High Resolution Imaging Science Experiment (camera on board Mars Reconnaissance Orbiter)
- LPSA:** Laser Particle Size Analyzer
- MGD:** Mantled Gravel Dunes model
- Moran's I:** Global spatial autocorrelation statistic (Moran 1950)
- MOLA:** Mars Orbital Laser Altimeter
- P(Er):** User-defined probability of slab erosion/transport in MGD
- P(θ):** User-defined probability of spanwise transport in MGD
- PBR:** Periodic Bedrock Ridge
- TAR:** Transverse Aeolian Ridge
- u*:** Shear velocity
- u*_t:** Threshold shear velocity (fluid threshold)
- u*_{it}^c:** Impact threshold of coarse grain population
- u*_{ft}^f:** Fluid threshold of fine grain population
- u(z):** Wind velocity at given elevation z
- UTM:** Universal Transverse Mercator
- v:** Kinematic viscosity
- w_s:** Terminal settling velocity of a particle
- w_x:** Percentage mass or count of a given grain size bin
- WGS84:** World Geodetic System 1984
- \bar{X}_C :** Sample mean of grain sizes from megaripple images

\bar{X}_F : Sample mean of grain sizes from smaller bedform images

z : Elevation above the bed

z_0 : Roughness parameter (elevation at which interpolated wind speed is 0)

γ : Scaling parameter for interparticle forces

κ : von Kármán constant, assumed to be 0.4

λ : Bedform wavelength, defined as the distance between two bedform crests.

λ_C : Ripple wavelength in the coarser-grained megaripple corridors

λ_F : Ripple wavelength in the finer-grained smaller bedform corridors

λ_S : Crosswind wavelength, defined as the width of one megaripple corridor and one smaller bedform corridor

ρ_f : Fluid density

ρ_p : Particle density

τ : Shear stress

θ : Spanwise angle of transport (in degrees off from parallel to wind direction)

To see a World in a Grain of Sand...

-William Blake, *Auguries of Innocence*

Chapter 1: Introduction

1.1. Motivation and Objectives

This thesis was motivated by observations of a longitudinal aeolian bedform pattern consisting of streamwise corridors of megaripples separated by corridors containing smaller bedforms (Figure 1.1). This thesis will refer to the pattern as megaripple stripes. Megaripple stripes were observed at eight sites on Earth and one site on Mars. Although some publications have acknowledged similar patterns (Newell and Boyd 1953; Haney and Grolier 1991; Durán et al. 2011; Silvestro et al. 2015), these have been anecdotal, each has used different terminology, and no measurements or detailed interpretations have been reported. The overarching objective of this thesis is to develop a more rigorous physical description of megaripple stripes and establish a hypothesis that explains their formation and evolution. This chapter outlines background information about aeolian processes and bedforms to provide context for the scientific approach and research methodology used in this thesis.

1.2. Literature Review

1.2.1. Aeolian Research

Since its inception, the study of aeolian processes has been an interdisciplinary field of research encompassing elements of geomorphology, sedimentology, physics, and other fields (Pye and Tsoar 2009). As a result, aeolian research spans vast spatial and temporal scales and has many approaches. The work of physicists is typically reductionist in approach and seeks to understand and upscale the behaviour of individual grains and small-scale processes. Fluid mechanics has made significant contributions in understanding airflow patterns over features and how the wind is affected by grains in transport. Geomorphologists and geologists have typically been more interested in behaviour at the scale of

bedforms and larger. The disciplinary boundaries in aeolian research are nevertheless fluid, and most work draws from a variety of fields and research traditions. For example, the importance and significance of computational modelling has increased across all sub-disciplines in recent decades and will likely continue to grow. This thesis aims to draw from each of these and takes an interdisciplinary approach.

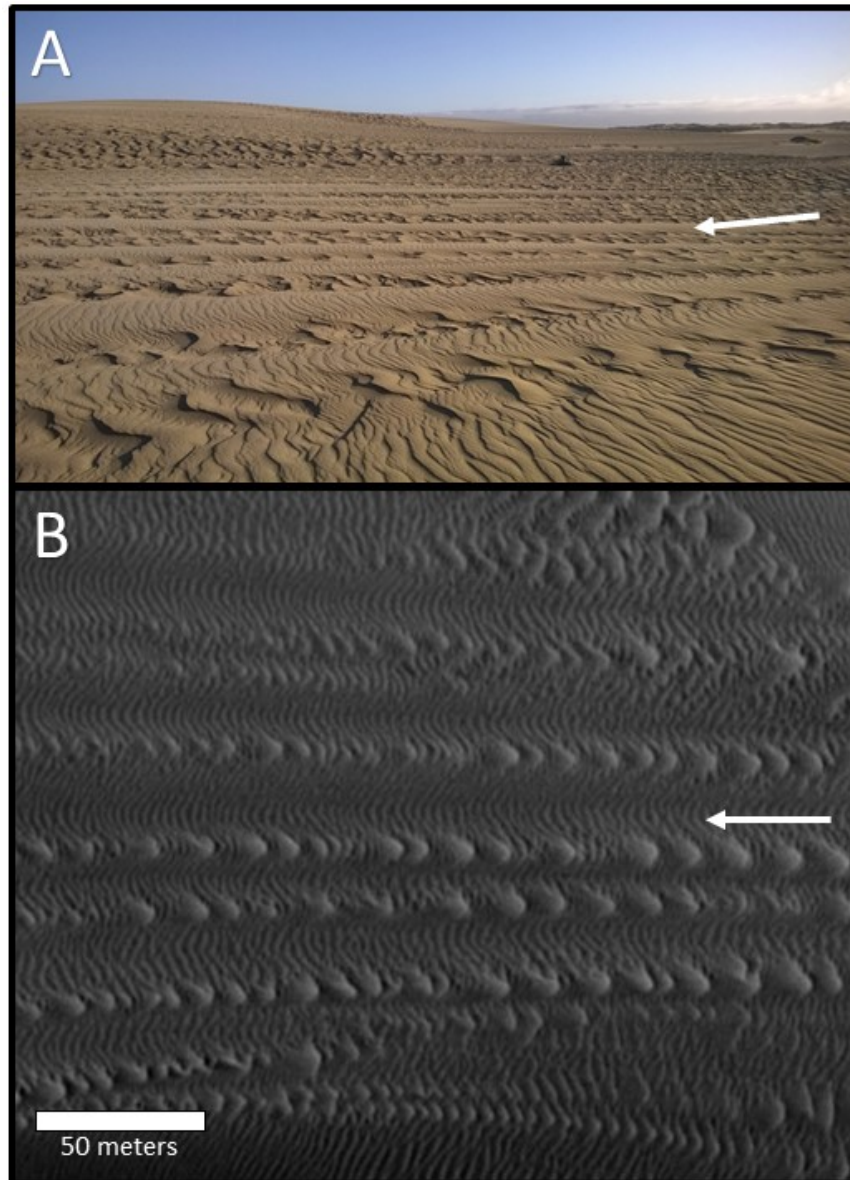


Figure 1.1: *A) Photo of megaripple stripes, looking crosswind, at Oso Flaco at the southern end of the Oceano Dunes. Photo: Raleigh Martin. B) Megaripple stripes in Rabe Crater, Mars. Image: HiRISE PSP_002824_1355, NASA/JPL/University of Arizona. Arrows indicate assumed dominant direction of transport.*

Recent research into aeolian sediment transport has been encouraged by discoveries of aeolian bedforms on other planets and the growing awareness that sediment transport by the wind is relatively common in our solar system (Sagan and Bagnold 1975; Greeley and Iversen 1985). This exploration into aeolian sediment transport on extraterrestrial bodies has also stimulated new research and discoveries on bedform classification (Diniega et al. 2017). Transverse Aeolian Ridges (TARs) and Periodic Bedrock Ridges (PBRs) are examples of previously undocumented bedforms identified on Mars prior to analogs being found on Earth (Balme et al. 2008; Hugenholtz et al. 2015; Hugenholtz and Barchyn 2017). Aeolian research has also created awareness of the different scaling behaviours of sediment transport on other planets because of their different gravitational and atmospheric properties, along with several other factors (Claudin and Andreotti 2006; Almeida et al. 2008; Sullivan and Kok 2017). Despite these differences, aeolian bedforms have similar shapes on Earth as they do elsewhere, suggesting a degree of universality in the form and process of aeolian features. Megaripple stripes are an example of this, and stripes identified on Earth and Mars exhibit similar morphologies. As megaripple stripes are composed of two types of small-scale aeolian bedforms, impact ripples and megaripples, these bedforms will now be discussed.

1.2.2. Impact Ripples

Impact ripples, or ‘ballistic ripples’, are small aeolian bedforms usually composed of well-sorted sand and can vary, within certain bounds, in size and shape. The development of impact ripples is ubiquitous on unvegetated sand surfaces where aeolian transport occurs (Lancaster 1995). Ripples can develop within minutes under a steady wind capable of initiating saltation (Rasmussen et al. 2015). The crests of ripples are perpendicular to the transport direction and generally display relatively little sinuosity, but this can vary significantly in poorly sorted grain size distributions (GSDs) or in environments with multiple prevailing winds (Walker 1981; McKenna Neuman and Bédard 2017). Unlike dunes, impact ripples change and adapt to local wind conditions quickly and reach their maximum size on timescales of minutes (Rasmussen et al. 2015).

Ripple development is the result of the instability of a flat bed subject to the bombardment of particles (Anderson 1987). The saltation of grains over a flat surface creates millimetre-scale bumps on the bed (Walker 1981; Anderson 1990). Even at this small scale the alteration of surface topography changes the probability of impacts on the newly roughened surface. The stoss side of these bumps are then more likely to be subject to impact than the lee, causing the bumps to increase in size (Bagnold 1941). This creates a situation in which the bumps continue to grow until the rate at which grains are being added to the ripple is in equilibrium with the rate at which grains are being removed. The removal of grains is associated with saltation and reptation, and from avalanching of grains down the lee slope, which is at or near the angle of repose (Sharp 1963). Grains are seldom removed directly from the lee slope of ripples by saltation and reptation because of the ripple's sheltering effect, commonly referred to as the 'shadow zone' (Sharp 1963; Schmerler et al. 2016).

The bedforms in the early stages of the development of a ripple field are termed 'proto-ripples' (McKenna Neuman and Bédard 2017). An important process in the maturation of a ripple field is the interaction and collision between ripples of differing sizes (Landry and Werner 1994). These collisions are constructive and lead to further maturation of a ripple field. A mature state of development is realized once the majority of the ripples in a field have reached a similar size and have long uninterrupted crestlines (Anderson 1990).

The morphometry of ripples is typically described by two metrics: wavelength (λ) and height (h). Wavelength is the crest-to-crest distance between ripples and is often reported from a series of transect measurements (Wilson 1972). Wavelength is perhaps the most important descriptor of morphology, and there is a large body of literature describing the processes that determine wavelength for both ripple-scale and dune-scale features (e.g., Bagnold 1941; Anderson 1987; Durán et al. 2014). Height is defined as the difference between the trough and crest of the bedform. The ratio of wavelength-to-height is referred to as the 'ripple index' and typically has a value of 15–20 in impact ripples of well-sorted sand (Anderson 1990).

1.2.3. Megaripples

Megaripples are distinguished from impact ripples by their larger heights and wavelengths, as well as a bimodal or poorly sorted GSD (Yizhaq et al. 2012a; Lämmel et al. 2018). Megaripples that develop in environments with a unimodal transport direction show more sinuosity (in plan view) and variation in their height (in cross-section) than regular impact ripples (Sharp 1963; Zimbelman et al. 2012). This can make the characterization and modeling of megaripples a three-dimensional problem rather than a simpler two-dimensional problem (Yizhaq 2004; Lämmel et al. 2018).

Megaripples have also been referred to as ‘granule ripples’ (Bagnold 1941; Sharp 1963), ‘gravel ripples’ (Ackert 1989), ‘pebble ripples’ (Greeley and Iversen 1985), and ‘coarse-grained ripples’ (Jerolmack et al. 2006). They have been recorded at wavelengths of up to 43 metres on Earth (Milana 2009). Megaripple development is caused by the existence of two distinct portions of the GSD on the bed surface: grains transported by saltation and grains that are predominantly transported by reptation (Bagnold 1941). The latter develop into an armour layer on the ripple crests and allow for megaripples to grow significantly taller than normal ripples (Yizhaq et al. 2012b). The presence of saltating grains and reptating grains creates two characteristic grain trajectories, or hop lengths, in the sediment transport system. As a result of these two length scales, megaripples typically develop more inconsistencies in height and wavelength than ripples on a well-sorted bed. This inconsistency leads to collisions between bedforms of different size. These collisions are an important process in the development of ripple fields, and it is thought that the rate at which these collisions occur does not decrease over time in fields of megaripples (Yizhaq et al. 2012b). Further research suggests that there is likely an inverse correlation between the number of defects in an area of megaripples and the degree to which the GSD is sorted (Yizhaq et al. 2012b).

A more poorly constrained concept is the relative amounts of reptating grains and saltating grains required for megaripple development. Further, the extent to which megaripple development causes a surface distribution to become bimodal versus pre-existing bimodality in the source deposit is a matter

that needs to be carefully considered and researched (Lämmel et al. 2018). Lämmel et al. (2018) suggested megaripples develop under locally erosive conditions, where the removal of fine grains by aeolian transport increases the concentration of coarse grains present at the surface over time. It is therefore consequential to make a distinction between a bimodal surface GSD that develops as a *consequence of* megaripple development and a bimodal surface GSD as a *requirement for* megaripple development. It may be that megaripples are capable of emerging from a unimodal, but poorly sorted GSD, and that it is the process of megaripple formation that causes the surface distribution to become bimodal over time (Lämmel et al. 2018). Regardless, megaripple development requires the formation of a coarse-grained crest and therefore requires a sufficiently large population of coarse grains for these armoured crests to develop.

Whether a significant portion of the GSD is a deflationary lag incapable of being transported is a matter of some interest here. Megaripples are known to source a significant amount of their coarse crest material from grains brought to the surface over time by deflation (Lämmel et al. 2018). However, the majority of these coarse grains can still be transported by reptation. As the surface GSD changes and fine grains are removed on a net erosional surface, the subsurface becomes the supply of sediment to the surface. As fine grains are transported downwind, the amount of coarse grains increases at the surface, affecting the relative proportions of saltating and reptating grains controlling megaripple development. Yizhaq et al. (2012a) observed the emergence of small megaripples in Israel over 16 months and noted increases in the surface concentration of coarse grains during megaripple development. An understanding of megaripple field development is therefore linked not only to the interaction of the wind and the surface GSD, but of the ongoing changes in the surface concentration of coarse and fine grains from upwind and subsurface sources.

In contrast to the minutes required for simple impact ripples to develop, the development timescale of megaripples is on the order of days to years because of their large size and reliance on reptation as a mechanism for growth (Isenberg et al. 2011; Katra et al. 2014). The exact timescales required for their

formation is disputed, especially in the case of the largest megaripples (Milana 2009, 2010; de Silva 2010). As megaripple crest development is driven by reptation, their growth is linked to the wind regime and the relative amounts and types of transport. Megaripple growth is also heavily influenced by the collision and interaction between bedforms occurring well past the early development stages (Yizhaq et al. 2012b). Ripple coalescence is the process by which ripples collide and merge to form larger ripples. Although there exists a correlation between the crest armour grain size and the wavelength of megaripples, the determination of megaripple wavelengths based solely on grain size is more unreliable than in the case of impact ripples (Qian et al. 2012; Yizhaq et al. 2012b; Yizhaq and Kutra 2015).

Megaripples can be destroyed if the surface armour is removed by strong winds and the underlying finer grains are exposed (Isenberg et al. 2011). If the fluid threshold of the largest grains on the surface is exceeded, then the ripples will be flattened if the strong wind continues for long enough to expose the finer grains below the armour layer. This condition was originally referred to by Bagnold (1941) as the ‘ultimate threshold’

1.2.4. Aeolian Sediment Transport Fundamentals

There are three primary modes of aeolian sediment transport: saltation, reptation, and suspension (Bagnold 1941). This thesis interprets reptation in the manner described by Anderson (1987), where reptation also includes the concept of ‘creep’ used by some authors. Saltation is the primary process governing the development of ripples and is generally well understood (Kok et al. 2012). Saltation is the transport of sand-sized particles, or larger in areas with extremely strong winds, by the wind in small hops on the order of 20–30 centimetres (Kok et al. 2012). As addressed, impact ripple development can be understood as a process by which the saltation of grains creates unstable topography on a sand bed and a regular ripple pattern emerges over time as that uneven topography evolves (Bagnold 1941; Durán et al. 2014; Lämmel et al. 2018). Reptation occurs when saltating grains impact the bed and cause grains to hop short distances on the order of a few grain diameters or less (Anderson 1987; Landry and Werner 1994;

Durán et al. 2011). Reptation is an important component of sediment transport and is crucial to megaripple development (Yizhaq et al. 2012; Lämmel 2018). Recent research has suggested that megaripples may be better understood as ‘reptation dunes’ because the primary factor affecting their growth is the reptation of larger grains (Lämmel et al. 2018). Suspension is essential for long-range transport of fine sediments but contributes minimally to the direct formation of ripples.

Anderson (1987) divides transported grains into populations of saltating grains and reptating grains. It is also suggested by Anderson (1987) that spatial variations in reptating grains create the defects observed in ripple fields. This approach of distinguishing between two dominant aeolian transport types has more recently been referred to as a ‘two-species approach’ and separates the population of grains into ‘reptons’ and ‘saltons’ (Andreotti 2004; Lämmel et al. 2012). This two-species approach has also been adopted in modelling ripple stratigraphy (Makse 2000). Saltons can be entrained directly by the wind. Reptons are reliant on impact from other grains as a mechanism for transport because they are too large to be entrained directly by the wind. This two-species approach is used in this thesis to understand how megaripple stripes develop and is incorporated into the model used to simulate them.

1.2.5. Aeolian Sediment Transport Thresholds

A transport threshold is the amount of force that must be exerted on a grain for it to be displaced into saltation. This is determined by the shear stress, τ , the wind exerts on the surface:

$$\tau = \rho_f u_*^2 \quad [1]$$

where ρ_f is the fluid density and u_* is the shear velocity. The transport threshold has traditionally been divided into two distinct thresholds in aeolian research: the fluid threshold and the impact threshold (Bagnold 1941; Martin and Kok 2018). The fluid threshold is the wind speed necessary to initiate transport of grains into saltation. The impact threshold is the wind speed necessary to sustain that saltation transport once it has been initiated, which is ~80% of the fluid threshold (Martin and Kok 2018). A

grain's resistance to transport can be understood as a function of its size, density, the force of gravity, and interparticle forces (Kok et al. 2012). Many equations exist for determining the fluid threshold, but Shao and Lu (2000) provide a simple solution for solving the threshold shear velocity, u_{*t} , at which a grain will be transported:

$$u_{*t} = A \sqrt{\frac{\rho_p - \rho_f}{\rho_f} g D_p + \frac{\gamma}{\rho_f D_p}} \quad [2]$$

where A is a constant with value 0.111 to model interparticle and lift forces as well as the Reynolds number of the flow, ρ_p is the particle density, g is the acceleration due to gravity, D_p is the particle diameter, and γ is a parameter to scale the interparticle forces with particle size. As shown by Jerolmack et al. (2006), once the fluid threshold for a grain of a given diameter has been determined the 'law of the wall' may be used to determine the wind speed necessary for transport:

$$u(z) = \frac{u_*}{\kappa} \ln\left(\frac{z}{z_o}\right) \quad [3]$$

where u is the wind velocity, z is the elevation above the bed, and z_o is the roughness length. Once $u_* > u_{*t}$, a grain may be lifted from the bed. Saltating grains entrained directly by the wind are ejected at high-angles from the bed and then follow low-angle trajectories at a velocity approximately equal to that of the wind (Pye and Tsoar 2009). A grain's trajectory is a function of the drag force exerted upon it by the wind and its settling velocity, w_s , (Ferguson and Church 2004):

$$w_s = \frac{((\rho_f/\rho_p) - 1)gD_p^2}{18\nu + \sqrt{0.75((\rho_f/\rho_p) - 1)gD_p^3}} \quad [4]$$

where w_s is the settling velocity, ν is the kinematic viscosity, and 18 is a theoretical constant determined by Ferguson and Church (2004). Borrowing from Shao and Lu (2000), saltation can be defined as the condition where the transport threshold of a grain is exceeded and $w_s/u_* > 5$. Short-term suspension

occurs when this ratio is between 1 and 5 because turbulence affects the particle's trajectory. Long-term suspension occurs when the ratio is < 1 .

The average saltation trajectory has a characteristic shape that varies relatively little with changing grain size, provided the wind still exceeds the transport threshold of the grains (Kok and Renno 2009). Saltating grains typically reach approximately the same velocity as the wind carrying them (Yizhaq et al. 2004; Pye and Tsoar 2009). There is thus little spatial variability in the trajectory of saltating grains on a well-sorted bed. This led Anderson (1987) to the conclusion that reptation and 'grain splash' must be the primary control on the behaviour of aeolian ripples.

In some aeolian environments, it can be expected that there is some portion of the GSD that is typically only capable of being transported by reptation. This portion of the GSD would be largely immobile if not for the impact energy provided by other grains during collision. Therefore, a precondition for transport by reptation is that there is a portion of the GSD capable of saltation to initiate reptation. The GSD in fields of megaripples, and by extension megaripple stripes, are thought to meet these conditions (Lämmel 2018). If the GSD is divided into two populations, those grains capable of being transported by saltation (saltons) and those reliant on reptation (reptons), then Jerolmack et al. (2006) show that the transport environment requisite for megaripple formation can be constrained by the inequality:

$$u_{*it}^c > u_* > u_{*ft}^f \quad [5]$$

where u_{*it}^c is the impact threshold of the coarse grain population and u_{*ft}^f is the fluid threshold of the fine grain population. The impact threshold of the coarse grains places the upper limit on the environment necessary for megaripple formation (Jerolmack et al. 2006). As addressed above, an exceedance of the fluid threshold of the coarse material would result in the removal of the armour layer on the ripple crests, and lead to the destruction of megaripples if this wind lasted for an extended period (Isenberg et al. 2011; Yizhaq and Kutra 2015). Finally, as the wind regime and GSD are variable between locations, these species definitions are applicable to a wide range of grain sizes according to the transport regime in any

given environment. For example, reptons may be medium-to-coarse sands in some environments and fine gravels in environments with stronger winds.

1.2.6. Spanwise Transport

Most sediment transport models only account for the downwind movement and height of saltating and reptating grains. Because of this, it is typically assumed that the saltation of individual grains has virtually no crosswind component and that transport is aligned with the wind direction. As the net transport is downwind, there may be no consequence to making this simplifying assumption in most cases. The frequent omission of a spanwise component in bedform modelling may not be due to a lack of awareness of the process, but simply because incorporating a third transport dimension in a modelling effort would introduce a layer of complexity and/or computational demand that would be unwieldy for most models. This difficulty was addressed by Yizhaq et al. (2004): “The main difficulty that is encountered in modelling two-dimensional ripple fields is that there are no available experimental results on the angular form of the splash function” (pp. 222–223). Nevertheless, a relatively small literature has developed in recent years to describe this spanwise component of aeolian sediment transport.

In the case of reptating grains, Yizhaq et al. (2004) incorporated spanwise transport into their theory for quantifying reptation flux. However, due to the lack of experimental data, they state that the distribution of spanwise angles is “currently not known, either from experiments or theory” (p. 211). Only recently have experimental data on the spanwise transport of individual grains been reported in the literature (O’Brien and McKenna Neuman 2016; O’Brien and McKenna Neuman 2018). These studies made use of particle tracking velocimetry to measure spanwise transport behaviour. O’Brien and McKenna Neuman (2016) found that only 12% of grains transported under a unidirectional wind had trajectories within $\pm 1^\circ$ of the wind. Further, the study found that “At high [spanwise] angles, the primary mode of transport appears to shift from saltation to reptation” (p. 137, O’Brien and McKenna Neuman 2016). This suggests that the spanwise component of transport is most important in reptation, and that

reptating grains have more variability in their transport behaviour than saltating grains (O'Brien and McKenna Neuman 2018). The importance of spanwise reptation in environments where there is a small population of grains that can be driven only by reptation has not yet been determined experimentally, and it is possible that spanwise transport plays an important role in megaripple development.

1.3. Megaripple Stripes

Megaripples stripes are a longitudinal pattern of streamwise corridors of longer-wavelength, higher-amplitude bedforms that alternate in the crosswind direction with corridors containing shorter-wavelength, lower-amplitude bedforms (Figure 1.1). The latter may be impact ripples or smaller megaripples. A preliminary inventory of megaripple stripes was performed using high-resolution satellite imagery to provide additional context for this pattern. Nine sites were identified: eight on Earth and one on Mars. There are likely many more locations with stripes on both planets that have yet to be discovered. Table 1.1 provides the locations of megaripple stripes found to date. Megaripple stripes appear to develop on the stoss slope of barchan dunes (Oceano, Dillon Beach, Rabe Crater, China, Namibia) or on relatively flat beds of sediment near abraded bedrock features (Argentina, Peru, Iran). The following sections provide additional details about the sites and stripe characteristics.

Table 1.1: *Megaripple stripe locations. Terrestrial coordinates acquired from Google Earth based on the WGS84 datum. Martian location acquired from the HiRISE database, which uses the Mars 2000 GCS and MOLA for elevation.*

Location	Coordinates	Elevation (m)
Oceano Dunes, California, USA	35.0908°N, 120.6278°W	4
Dillon Beach, California, USA	38.2366°N, 122.9597°W	7
Rabe Crater, Mars	44.00°S, 34.54°E	-4200
Abra Pomez, Argentina	26.8319°S, 67.6213°W	3902
Paracas Peninsula, Peru	13.8892°S, 76.2797°W	30
Ica Desert, Peru	14.5391°S, 75.5161°W	377
Lut Desert, Iran	30.8338°N, 57.869771°E	239
Longyanxia Reservoir, China	35.8767°N, 100.3650°E	3181
Walvis Bay, Namibia	23.0332°S, 14.4855°W	8

1.3.1. Oceano Dunes and Dillon Beach, California, USA

Oceano Dunes is an active coastal dune field on California's Central Coast. Megaripple stripes are found at the southern end of the dunes at Oso Flaco (Figure 1.1A) and at the Oceano Dunes Natural Preserve (Figure 1.2). Prevailing winds in the area are onshore from the west-northwest, perpendicular to the dune crestline orientation (Namikas 2003; Gillies and Etyemezian 2014; Adhikari 2017). Adhikari (2017) estimates that two-thirds of annual aeolian transport potential in this region occurs from March through June. The stripes at the Oceano Dunes Natural Preserve were visited during a field campaign in November 2017. The majority of the stripes were located on the stoss slopes of barchan dunes. Megaripple stripes at this site form directly downwind of a beach and foredune system. The megaripple stripes found at the Oceano Dunes are the smallest scale megaripple stripes identified to date. Nevertheless, they closely match the pattern found at other sites.

Megaripple stripes were also found in a similar environment to Oceano at a small dune field in Dillon Beach, California, USA, north of San Francisco. These stripes were located on the stoss slope of a dune. Silvestro et al. (2015) described the stripes from Dillon Beach, but provided no measurements or details beyond a brief visual characterization.

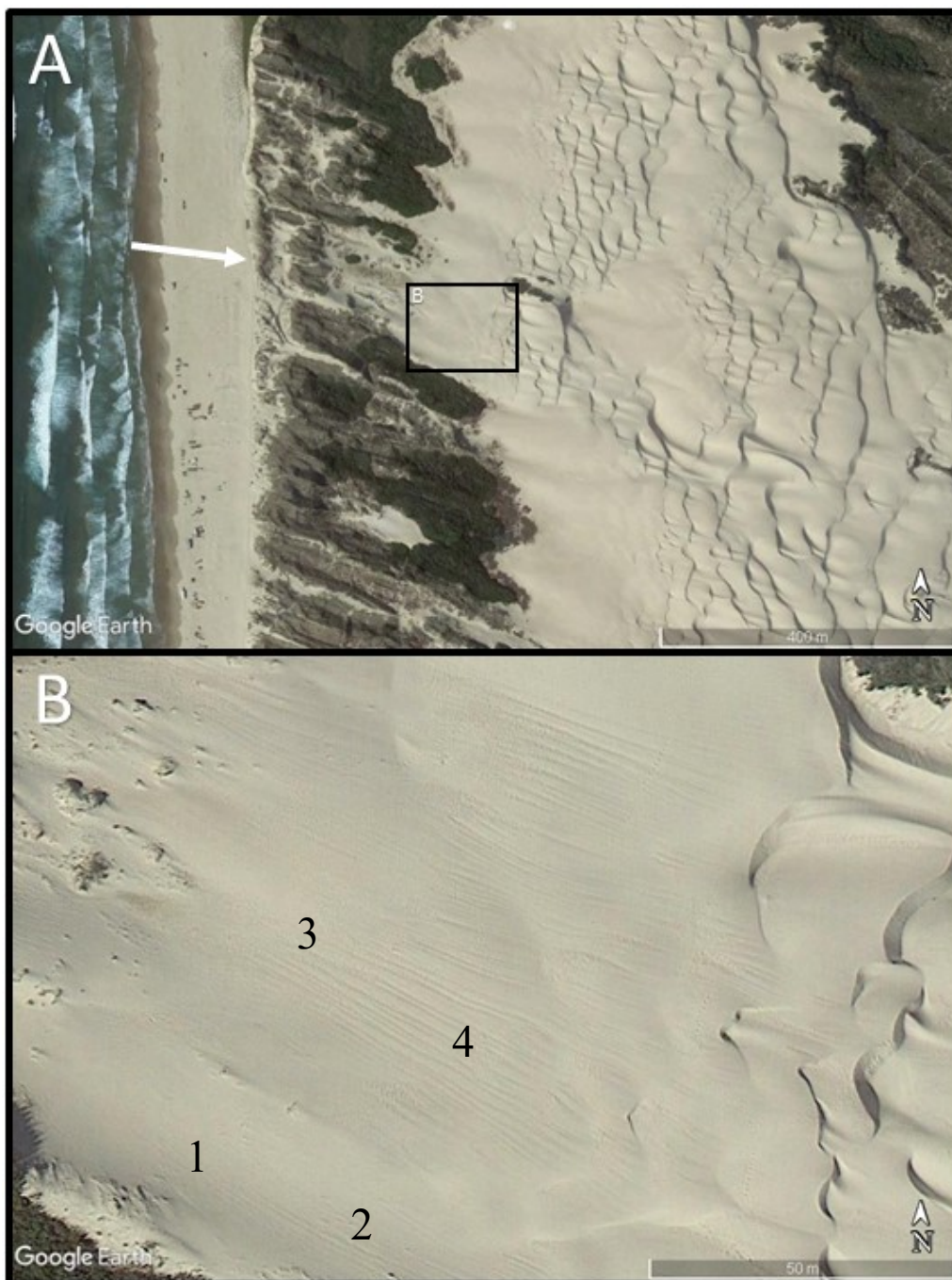


Figure 1.2: *A) Overview of the northern portion of the Oceano Dunes Natural Preserve. The dominant winds come from the west-northwest. A large beach and foredune system are directly to the west of the dunes. B) Megaripple stripes and the field site visited in 2017. Numbers denote the four locations at which physical samples were acquired (see §2.3.1.).*

1.3.2. Abra Pomez, Argentina

Megaripple stripes in the Andes Mountains of northwestern Argentina were identified in satellite imagery and visited in 2014 and 2015 (Figure 1.3). The stripes are located in a valley (Abra Pomez) approximately 53 kilometres southwest of the village of El Peñón. The surficial geology of this region reflects a legacy of volcanic activity (de Silva 1989). Megaripples and yardangs are pervasive throughout the region (Milana 2009; de Silva et al. 2013; Hugenholtz et al. 2015; Barchyn and Hugenholtz 2015). The surface sediment on the megaripples consists of pumice, basalt, andesite, and a variety of other lithics from upwind sources (de Silva et al. 2013; Báez et al. 2015; Hugenholtz et al. 2015). Greene (1995) and Favaro et al. (2017) suggest that the main aeolian sediment transport direction is northwesterly, as evidenced by the orientation of yardangs and aeolian rat tails carved from the ignimbrite. The stripe orientation suggests development under the influence of northerly wind. During field visits in 2014 and 2015 no physical samples were retrieved from the stripes, but close-range photographs were acquired to characterize the surface sediment texture of the megaripples and the adjacent corridors. Excavations did not reveal a link between the megaripples and underlying bedrock topography, as noted elsewhere in the region by Milana (2009) and Hugenholtz et al. (2015). The features at this site provide several insights into the pattern. For example, it is apparent that the megaripple corridors become progressively thinner downwind (Figure 1.3A–C).

1.3.3. Paracas Peninsula and Ica Desert, Peru

Stripes have been identified at many coastal desert sites in Peru, but are particularly extensive on the Paracas Peninsula, approximately 220 kilometres south of Lima, and along the Pan-American Highway 56 kilometres southeast of Ica (Figure 1.4). These stripes were briefly described by Haney and Grolier (1991) as well as Silvestro et al. (2015). The prevailing wind direction on the Paracas Peninsula is southerly, although further inland the wind steers to the west (Gay Jr. 2005). Haney and Grolier (1991) noted that some of the Paracas stripes are within a field of yardangs and that the orientation of the yardangs matches that of the stripes, further suggesting a unimodal transport regime in the area. Newell

and Boyd (1955) acquired grain samples from megaripples in the Ica Desert in Peru and reported a mean grain size of 2–4 mm, with the coarsest grains in the 4–8 mm range.

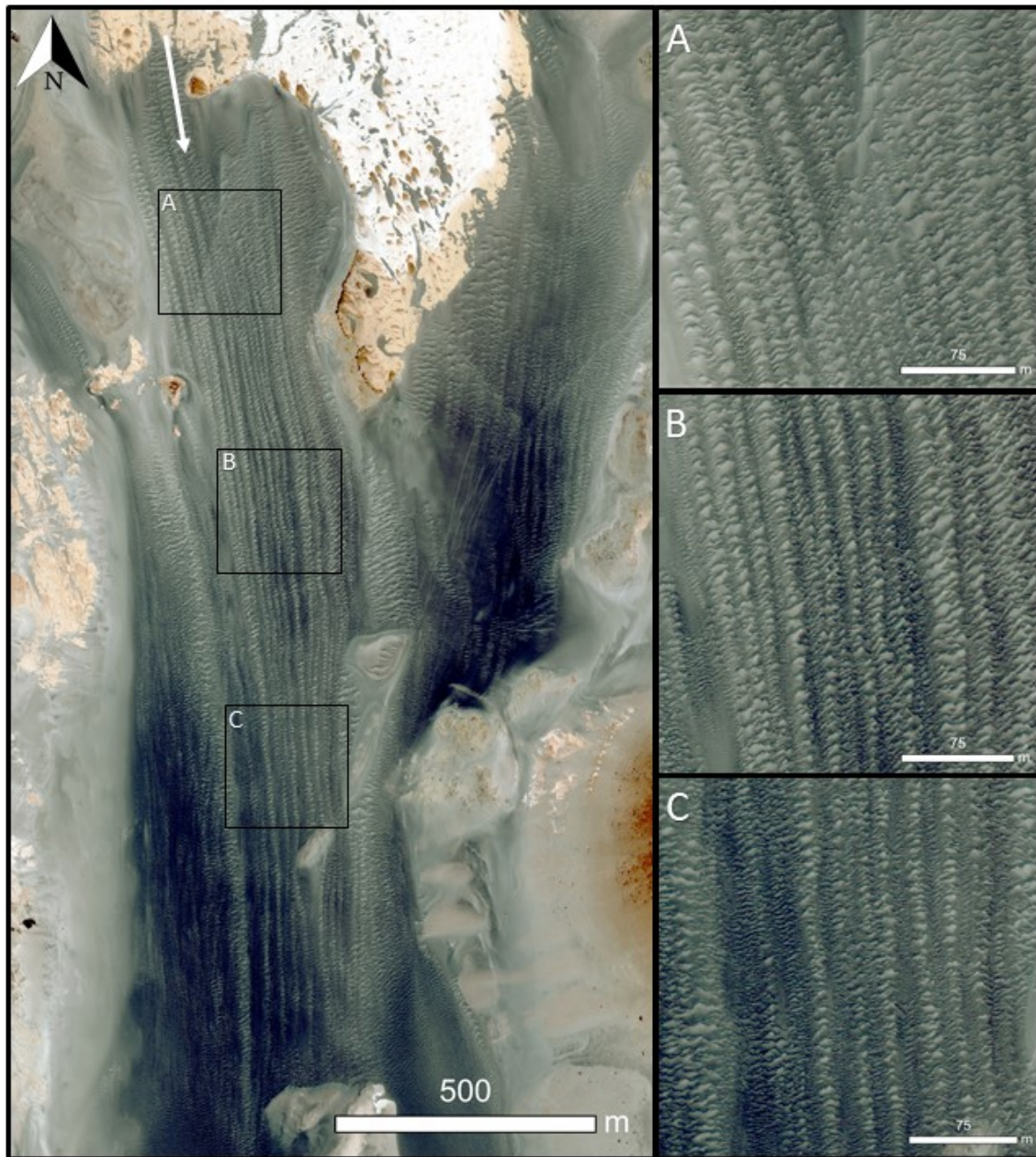


Figure 1.3: *Striped megaripples at Abra Pomez. Arrow indicates direction of dominant wind. As the pattern initiates upwind in A, megaripple crests extend almost entirely crosswind and the striped pattern is not yet very distinct. The striped pattern becomes more evident in B, and the megaripples have a distinct cusped shape. In C, the megaripple corridors begin to thin until further downwind the striped pattern fades almost entirely.*

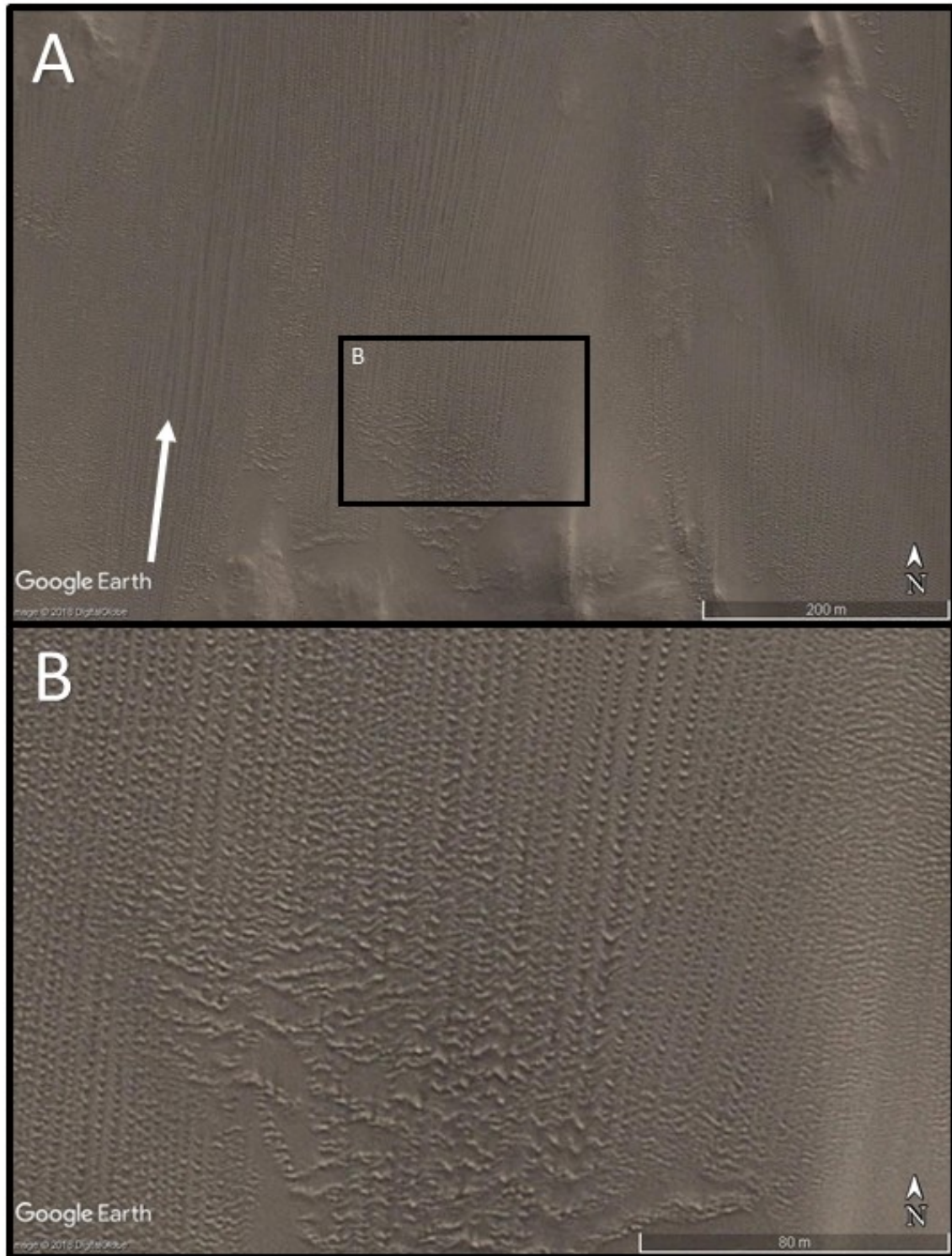


Figure 1.4: *A) Large field of megaripples and megaripple stripes in the Ica Desert, Peru. Megaripple stripes are common in this region. Arrow indicates direction of dominant wind. B) Inset photo. The bottom of the image shows megaripples developing into stripes downwind. Note the cusped shape of the megaripples in the stripes.*

1.3.4. Lut Desert, Iran

Stripes observed in the Lut Desert of Iran are located on the northern margin of a large field of yardangs (Figure 1.5). The orientation of the stripes is aligned with the orientation of yardangs, suggesting development from northwesterly wind. Megaripples dominate the terrain in other parts of the Lut Desert and bear strong morphological similarity to TARs on Mars (Hugenholtz and Barchyn 2017). One such set of TAR features on the eastern margin of the Lut Desert with characteristics very similar to those observed at other locations were also measured (Figure 1.6). It is unclear whether these features have the same origin and characteristics as other megaripple stripes, as they are of a slightly larger scale, have bedform crests with little curvature, and have no discernible bedforms in the corridors between the larger TAR bedforms.

1.3.5. Longyanxia Reservoir, China

Stripes in China were identified with satellite imagery in a dune field west of the Longyanxia Reservoir along the Yellow River (Figure 1.7). This is an area with active dunes and much of this region is undergoing desertification because of increasing temperatures, wetland drainage, and overgrazing (Hu et al. 2013). The orientation of the barchan dunes on which the stripes develop suggests a dominant northwesterly transport direction in the region.

1.3.6. Walvis Bay, Namibia

Stripes were identified in a field of barchanoid dunes south of Walvis Bay, Namibia (Figure 1.8). The stripes occur in the upwind portion of the dune field. Fryberger et al. (1992) described megaripple deposits in this area and found that the prevailing wind direction is southwesterly. These stripes, like those found in Oceano, China, and Mars, form on the stoss slopes of dunes.

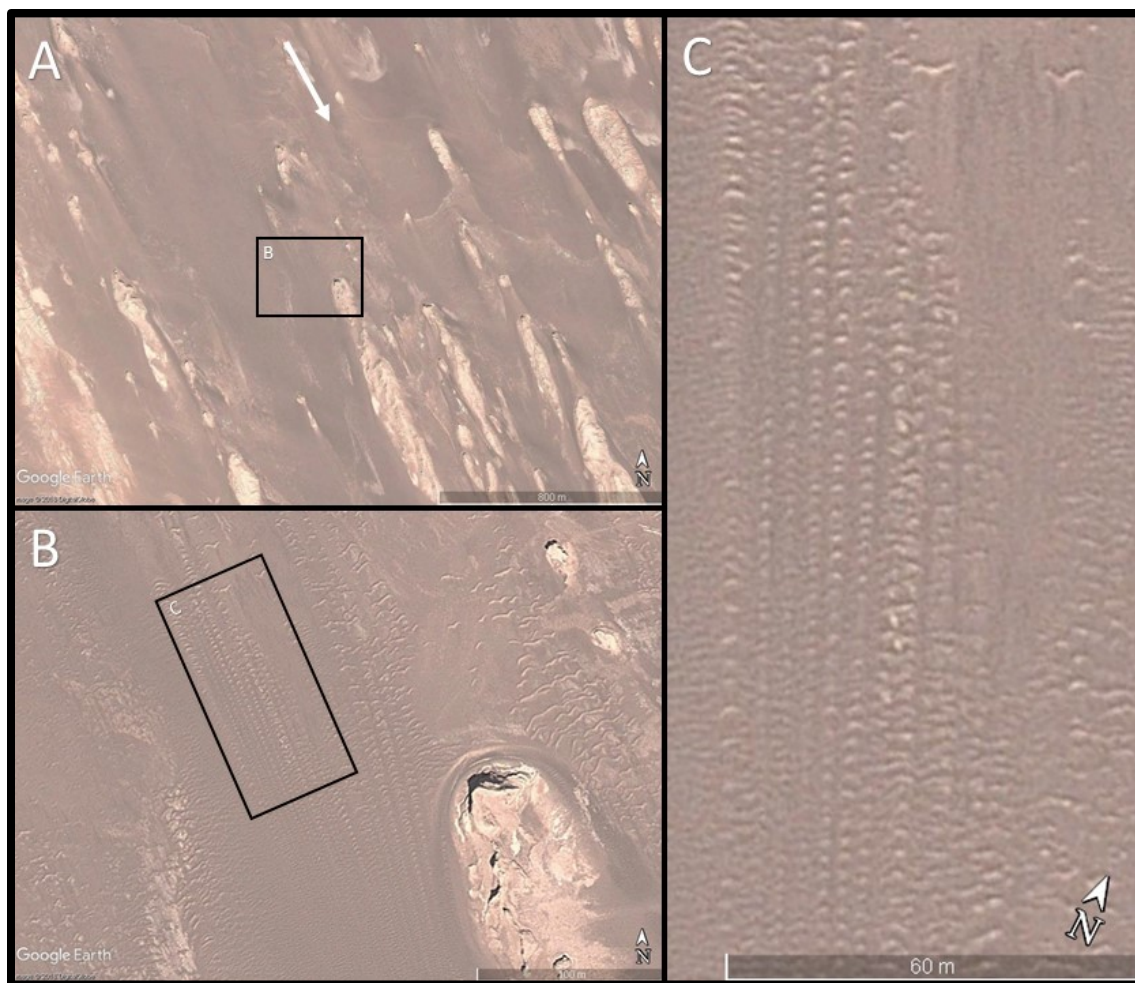


Figure 1.5: *A) Megaripple stripes in Iran develop in a large field of yardangs. Arrow indicates direction of dominant wind. B) As with megaripple stripes in Argentina and Peru, the stripes thin downwind and become smaller megaripples or impact ripples. C) The cusped shape of the megaripples and the regularity of the pattern in the Lut Desert closely matches that observed at the other locations.*

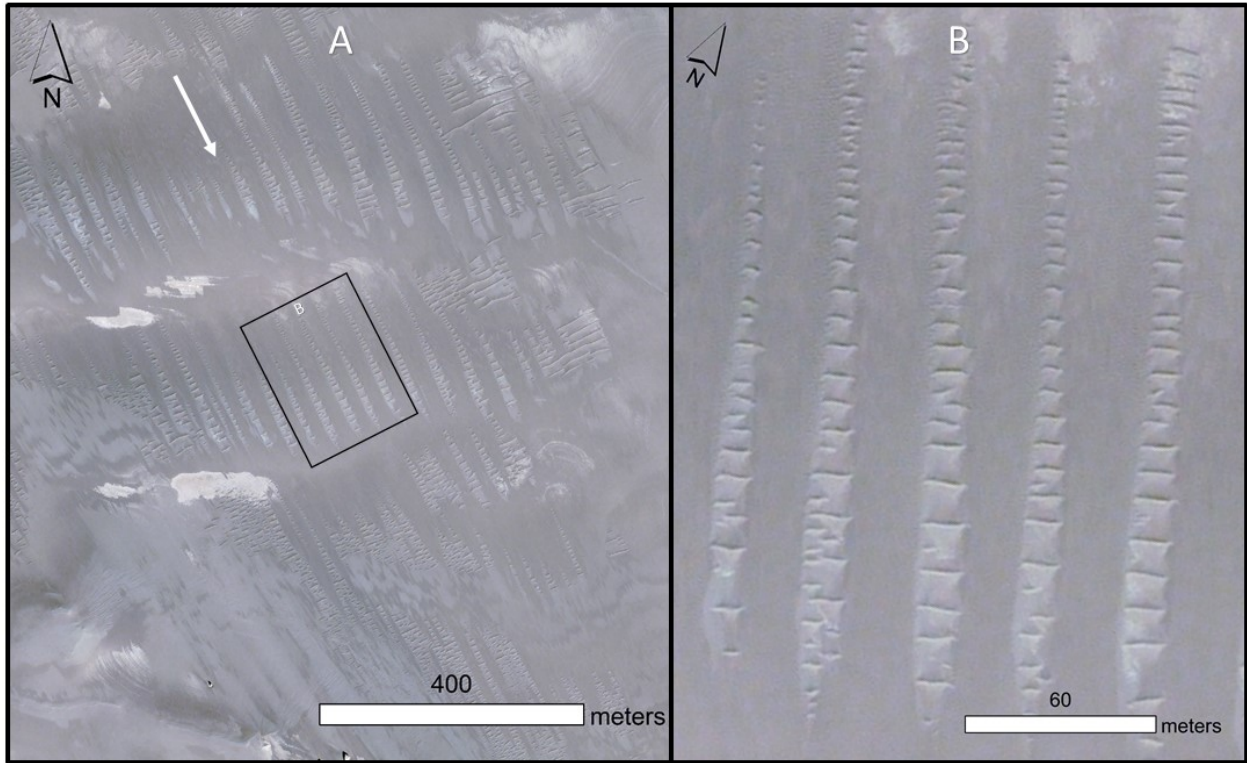


Figure 1.6: *A) Striped features in the Lut Desert identified as TAR analogs by Hugenholtz and Barchyn (2017). B) These features do not have the cusate shape seen at other locations. The scale of these bedforms is also larger than other locations and there are no obvious bedforms in the corridors between larger bedforms. The crosswind corridor patterning suggests these features may be megaripple stripes.*

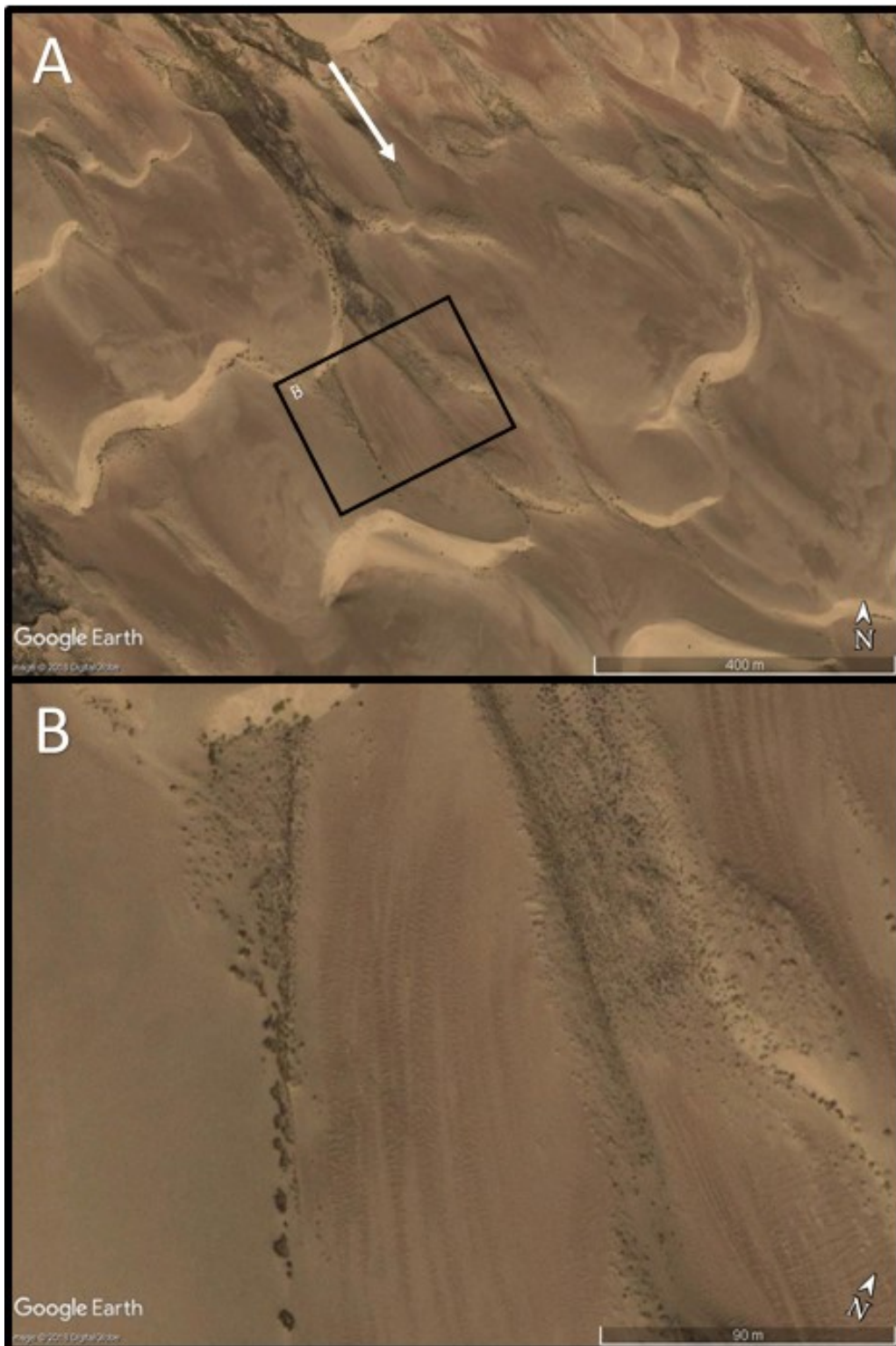


Figure 1.7: *A) Field of barchanoid dunes near the Longyanxia Reservoir, China. Megaripple stripes are found on many of the stoss slopes of the dunes. B) Inset image. The width of the megaripple stripes decreases downwind as the megaripples climb the dune.*

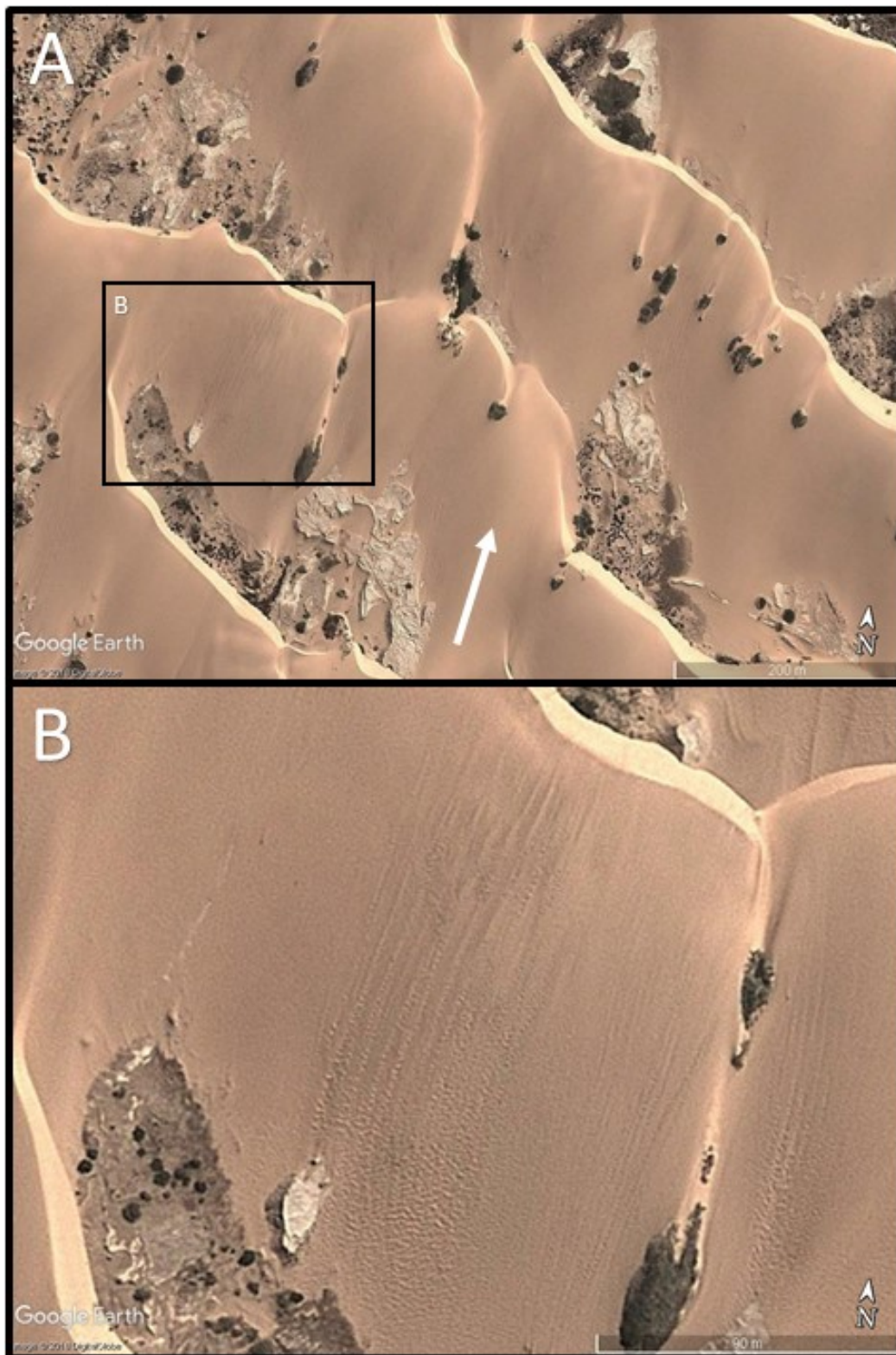


Figure 1.8: *A) Megaripple stripes develop on the stoss of several barchanoid dunes eight kilometres south of Walvis Bay, Namibia. B) The pattern can be seen emerging into corridors after beginning as megaripples at the base of the dune and thinning out almost entirely at the crest of the dune.*

1.3.7. Rabe Crater Dunes, Mars

The Rabe Crater dune field is 1750 km² and is composed primarily of barchanoid dunes. The dominant transport direction in the crater is from the southeast, and the dunes have been documented migrating in a northwesterly direction (Fenton 2006). The Rabe Crater dunes are notable for their unique dark sediment whose source is a matter of some significant discussion in the literature but is likely transported from a source local to the crater (Fenton 2006; Tirsch et al. 2011). The presence of corridors of metre-scale bedforms (presumably megariipples) with different wavelengths is apparent and matches closely the stripe patterns observed on Earth (Figure 1.9).

1.4. Research Approach and Working Hypotheses

The foregoing discussion of aeolian sediment transport, megariipples, and megaripple stripes provides essential context for the research approach developed for this thesis. The literature indicates the processes responsible for forming megariipples are closely linked to the GSD; sediment too coarse to saltate is left behind to accumulate on the surface as smaller sediment transported more readily is carried downwind. Coarse grains move by reptation and slowly organize into megariipples. However, this simple mechanistic explanation does not explain the co-existence and co-evolution of two bedform length scales that organize into narrow, alternating streamwise corridors. The formation of two bedform length scales in close proximity is unlikely the result of lateral variations of wind flow, although feedbacks once the bedforms develop probably influence their evolution. Without context it is also tempting to cite topographic features as a plausible mechanism for seeding the pattern upwind, but there are no visible signs of any regularly spaced obstacles upwind at each of the sites described in §1.3. that could explain the regularity of the pattern.

The main driver of the research activities outlined in this thesis is to determine where and why megaripple stripes occur. The first research priority was to develop a detailed physical characterization of megaripple stripes by examining their morphology, pattern metrics, and GSD. The second priority was to

leverage empirical measurements and background context about megaripples to examine why the striped pattern emerges.

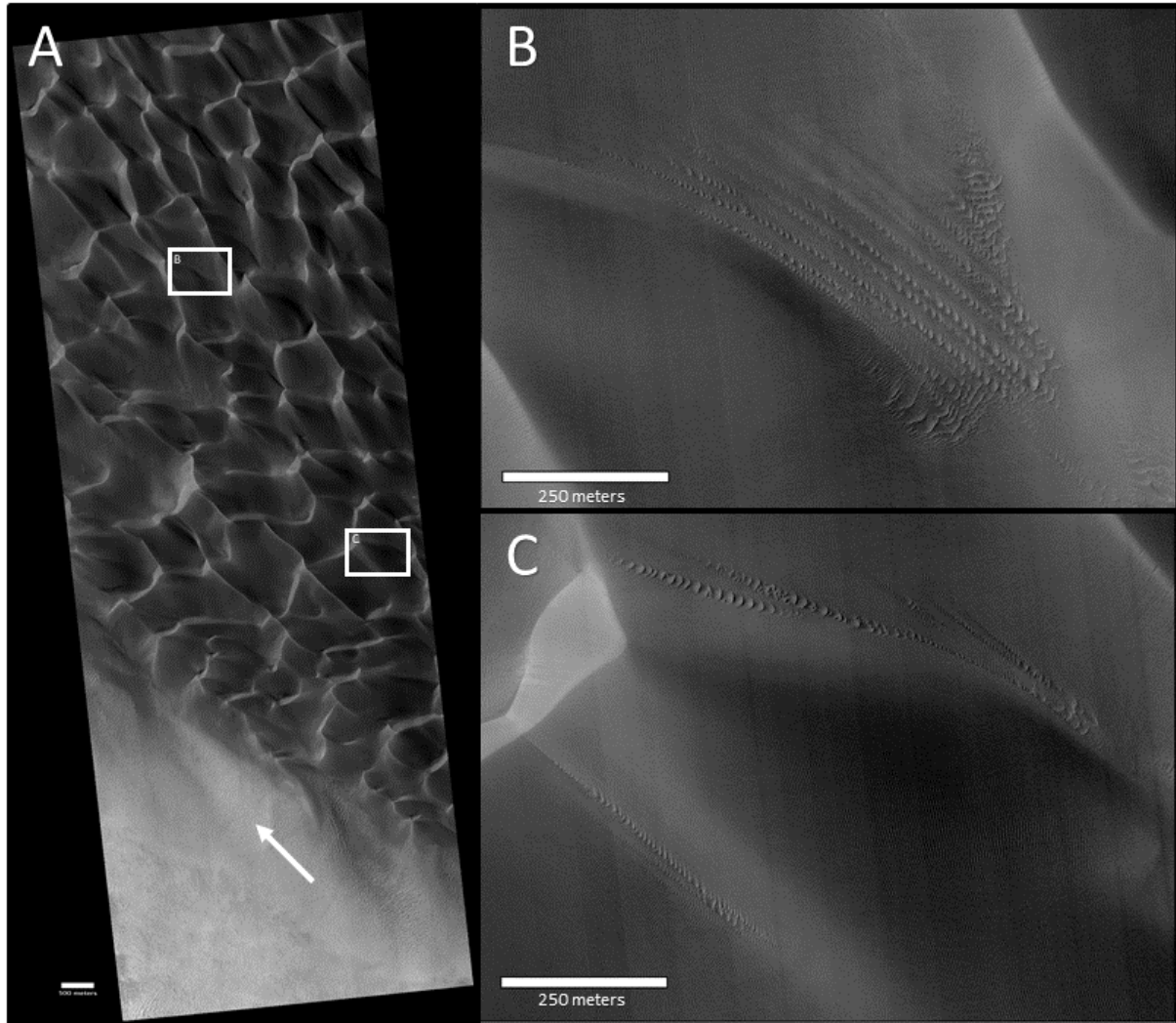


Figure 1.9: *A) Rabe Crater Dune Field, Mars. The bottom of the image is a large field of metre-scale bedforms. A large field of barchanoid dunes is present in the rest of the image, with several megaripple stripes present throughout the dune field. These megaripple stripes show a striking similarity to those found on Earth. B) Example of the megaripple stripe pattern with several alternating corridors of small and large bedforms. Figure 1.1B shows a close-up of these same features. As with the terrestrial locations, the megaripple corridors can be seen thinning out downwind. C) Example of individual corridors of megaripples, suggesting a differential grain size between these stripes and the surrounding bedforms. Image: HiRISE PSP_002824_1355, NASA/JPL/University of Arizona.*

To guide research activities, two working hypotheses were developed:

- (a) Megaripple stripes are characterized by crosswind variations of surface sediment texture—megaripple corridors have larger grains on the surface than the adjacent corridors containing smaller bedforms.
- (b) The development of megaripple stripes is contingent on the proportion of repton in the source deposit and on the surface. If the proportion of repton is too high, megaripples develop, but not stripes.

The first hypothesis proposes that grain size plays a role in the crosswind variations of bedform sizes in megaripple stripes. Katre and Yizhaq (2015) showed that the downwind wavelength of megaripples increases as the surface sediment size increases. Megaripple corridors should thus have coarser sediment than the adjacent corridors containing smaller bedforms. Of course, the most confounding aspect about sites with megaripple stripes is the restricted development of the megaripples. If the wind regime and environment is conducive to megaripple development, why do they not cover the entire site? It is far more common for megaripples to develop in fields with no systematic streamwise or crosswind patterning, as evidenced by research in Israel (Yizhaq et al. 2009), Argentina (Milana 2009; Hugenholtz et al. 2015), China (Qian et al. 2012), and Iran (Hugenholtz and Barchyn 2017). Observations suggest that if the proportion of repton in the source deposit is low, there may be an insufficient coarse fraction to exclusively form megaripples (e.g., Durán et al. 2011). The second hypothesis therefore targets the formation of megaripples and suggests that megaripple stripes develop in environments with a limited supply of repton.

Measurements of grain size and bedform morphometrics are appropriate for testing the first hypothesis. However, a direct physical experiment and measurements are unsuitable for the second hypothesis due to the timescale required for megaripple formation (2–5+ years according to Milana et al. 2010 and Yizhaq et al. 2012a). Therefore, a numerical modeling approach was developed based on

previous successes simulating the development of related landforms: dunes and sorted stripes on hillslopes (Werner 1995; Kessler and Werner 2003).

Chapter 2: Methodology

2.1. Overview

This chapter describes the methodology used to measure megaripple stripe morphometrics and grain size, as well as the model and parameters used to simulate their development. Very little is known about megaripple stripes and only a few anecdotal reports of their properties have been published (e.g., Newell and Boyd 1953; Haney and Grolier 1991; Durán et al. 2011; Silvestro et al. 2015). To fill this knowledge gap and test the first hypothesis outlined above, a set of morphometric measurements and grain size analyses were performed. These measurements include the wavelengths, in crosswind and downwind directions, of the megaripple corridors at sites described in §1.3. Additionally, to understand and make a distinction between the corridors of megaripples and corridors of smaller bedforms, grain size analyses were performed for the megaripple stripes at the Oceano Dunes, California, USA, and at Abra Pomez, Argentina. Field measurements at these locations mainly focused on the surface GSD, but observations and measurements provided additional context about the patterns and bedform morphology. The stripes at Oceano Dunes were also small enough to develop digital surface models (DSMs) using close-range photogrammetry. Together, these three approaches allow for a more complete physical description and understanding of megaripple stripes than is currently available in the literature.

To test the second hypothesis and better understand the development of megaripple stripes, a cellular automata (CA) model was used to simulate their development and evolution. This CA model builds on the Werner (1995) approach by including two species of cells, or ‘slabs’, to represent saltons and repton. Slabs are representations of some volume of sediment and do not represent individual grains. The incorporation of two slab types allowed for the development of megaripple-type features in the model space. The concentration of repton, the erosion likelihood of slabs, and the amount of spanwise transport for the two slab types were modified in the model to test their effects on model outputs. Changes in model output caused by adjusting these parameters were observed to constrain the parameters that produce

megaripple stripes. Outputs from the model were compared to field-based measurements of megaripple stripes in order to evaluate model verisimilitude.

2.2. Morphometrics

2.2.1. Wavelength Measurements

The morphology and pattern of megaripple stripes were poorly resolved in previous reports. To address this gap, measurements and observations were undertaken with high-resolution satellite imagery from Google Earth and were complemented with field measurements and observations of stripes at Abra Pomez, Argentina, and the Oceano Dunes, California. The satellite imagery provided an overview of the striped patterns, but the spatial resolution was, in all terrestrial cases, insufficient to resolve specific details about the morphologies of the smaller bedform corridors. The high-resolution imagery and size of the features at Rabe Crater, Mars allowed all the features in both corridor types at this location to be measured. The only sites for which no morphometrics whatsoever could be resolved with enough detail from the satellite imagery were the Oceano Dunes and Dillon Beach, California. The larger bedforms at these locations were below the spatial resolution of available satellite imagery.

One of the most distinct characteristics of megaripple stripes is the somewhat regular crosswind spacing of the corridors. To measure this, an approach developed for quantifying the spacing of sorted stripes on hillslopes was adapted for measuring the crosswind, or spanwise, wavelength (Francou et al. 2001). Figure 2.1 illustrates the dimensions representing the crosswind and downwind wavelengths of the megaripple stripes. With the exception of the megaripple stripes at Oceano Dunes, which were measured in the field with a tape measure, wavelength measurements were made using satellite images from Google Earth and a HiRISE image of Mars. Images were imported into ArcMap© and georeferenced using 15–23 tie points and coordinates from Google Earth (WGS84). To limit bias, a random sampling approach was applied in which a polygon sampling area was drawn over the megaripple stripes and random points were generated within the sampling area. Sample points ranged from 24 for the site with the least extensive

megaripple stripes (Namibia) to 103 for the site with the most extensive megaripple stripes (Argentina). Transects were then drawn to measure crosswind and downwind wavelength. Downwind transects were created perpendicular to the crestline orientation, beginning at the crest of the feature closest to the sampling point and ending at the crest of a feature downwind in the same corridor as the first feature. The downwind wavelength was measured as the length of the transect divided by the number of crestlines crossed by the transect, not including the first. All transects began and ended on a crestline. Crosswind transects were drawn parallel to the orientation of megaripple crestlines such that they intersected the sampling point and crossed the spanwise width of several megaripple stripes. Crosswind wavelength was measured as the length of the transect divided by the number of pairs of megaripple and smaller bedform corridors intersected. Many of the sampling points fell in locations where the wavelength could not be determined. In these cases, the nearest location that could be resolved was used. The mean wavelength for each location was calculated by dividing the sum length of all transects by the sum number of wavelengths counted for all transects.

2.2.2. 3D Reconstructions

3D reconstructions of stripes at the Oceano Dunes were created in order to examine vertical characteristics of stripes in detail. The DSMs were developed using images from a consumer-grade DSLR camera and Pix4D© software. Five reconstructions, each using 200–600 overlapping photos taken during the November 2017 field campaign, were created to generate DSMs and cross-sectional measurements of ripple profiles. Pix4D© uses principles of structure-from-motion photogrammetry to generate matching points in overlapping imagery (Westoby et al. 2012). Using known ground control points in the photographs, these point cloud outputs can be scaled to produce orthoimages and DSMs. The DSMs were also used to evaluate verisimilitude of the model simulations. This involved the creation of transect profiles of megaripple and smaller bedform corridors from the DSM using the 3D Analyst package in ArcGIS©.

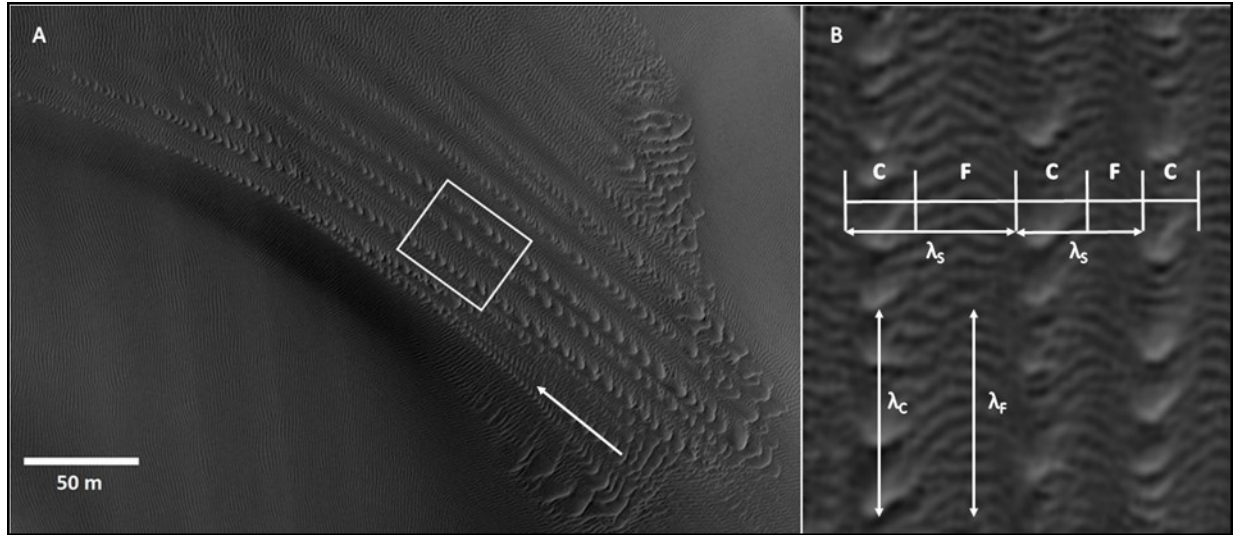


Figure 2.1: *A) Overview of megaripple stripe pattern in the Rabe Crater dune field, Mars. Arrow indicates assumed dominant direction of transport. B) Inset image showing alternating pattern of megaripple corridors, C, and smaller bedform corridors, F. A spanwise wavelength, λ_s , is defined as the width of a pair of corridors. The two downwind transects show λ_c , where the transect spans three wavelengths, and λ_F , where the transect spans ten wavelengths over the same distance. (Image: HiRISE PSP_002824_1355, NASA/JPL/University of Arizona).*

2.3. Grain Size Measurements and Analyses

Understanding the GSD of aeolian bedforms is crucial because grain size is a primary factor governing morphometrics and transport behaviour. It is generally understood that, assuming equal grain densities and other properties, larger grains produce proportionately larger bedforms. Of course, these relationships are typically non-linear and further depend on the nature of the transport. Despite these complications, quantifying grain size remains essential to aeolian research. In the case of megaripple stripes, quantifying the grain size difference between the corridors of megaripples and smaller bedforms is central to the hypotheses outlined above.

There are several methods for quantifying grain size. Each is used depending on whether a physical sample is available or not, and the nature and size of that sample. Grain size measurements for megaripple stripes were based in two locations: the Oceano Dunes, California, and Abra Pomez, Argentina. For the Oceano Dunes, a laser diffraction analysis method was used on physical samples

collected in the field. For Abra Pomez, Argentina, a photo-based method was used from photographs taken during field campaigns at the site, because collecting physical samples was not practicable.

2.3.1. Oceano Dunes, California

Sediment samples were acquired for grain size analysis from the Oceano Dunes in November 2017 at four sampling sites (shown in Figure 1.2B). Samples were acquired from the crests of bedforms in both corridor types and in the transitional areas between the two (Figure 2.2). Ripple crests were targeted for sampling because this is where surface grain size is typically coarsest. In total, 17 samples were obtained from megaripple corridors, 13 samples from smaller bedform corridors, and five from transitional areas. Surface samples (< 0.5 cm) and depth samples (1–5 cm) were acquired to assess the armour grain size and bulk grain size of the bedforms. The surface samples were collected by scraping the near-surface sediment with a spoon, penetrating no farther than approximately a half centimetre below the surface. Bulk samples were acquired to a depth of one to five centimetres (from the crest of the ripple to its base) using a spoon. Sample mass ranged from 38 to 110 grams at each location, and each sample contained material from several bedforms, typically five to twenty, in the same corridor. In total, nine surface samples and 26 depth samples were acquired.

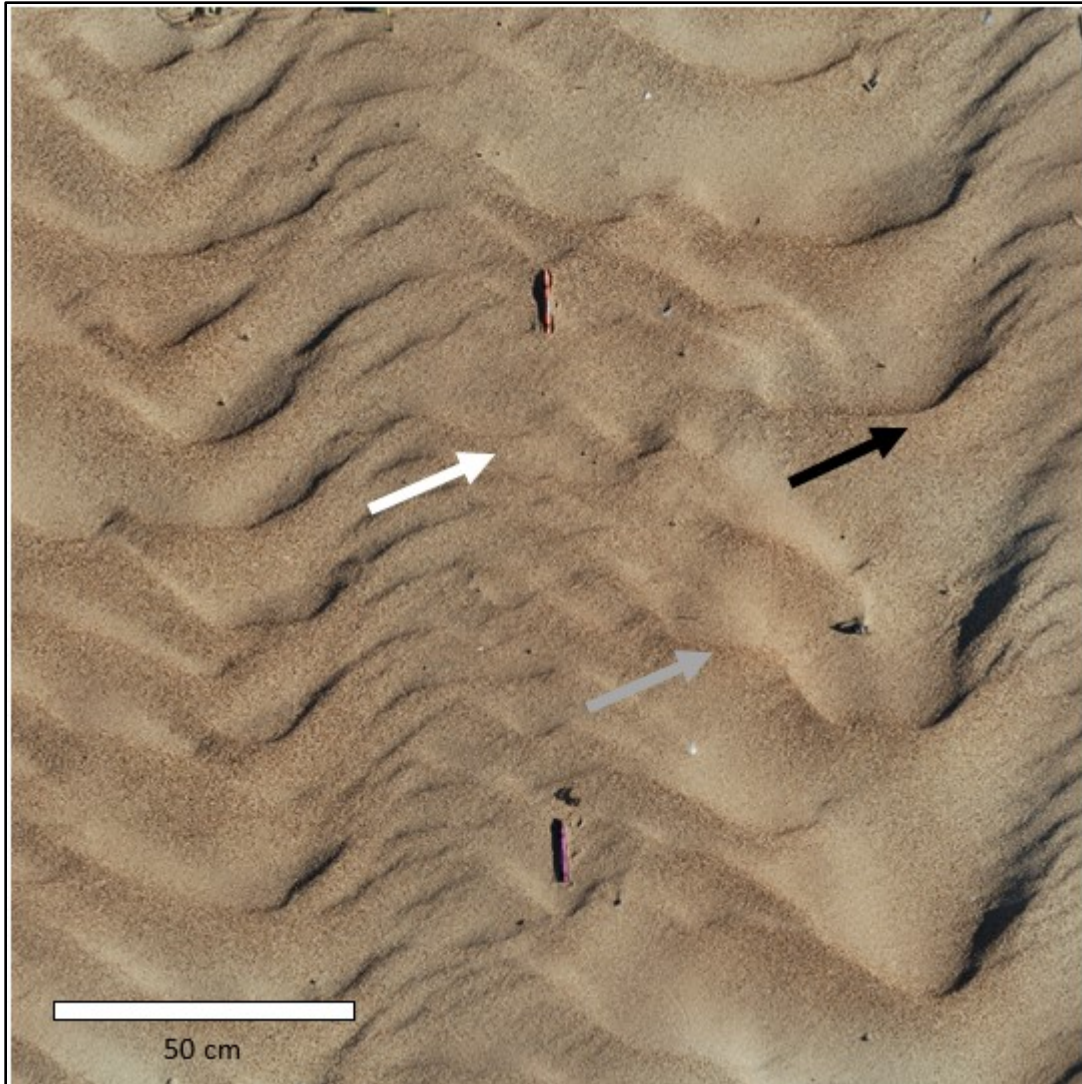


Figure 2.2: Example locations of sample acquisition for megaripple corridors (black), smaller bedform corridors (white), and transitional areas (grey) for sample acquisition. As noted in the text, several bedforms were used to gain a sufficient sample mass and representative sample.

In the lab, each sample was riffled and two subsamples from each sample were measured using a Hydro 2000G sample dispersion unit and a Malvern Mastersizer 2000© laser particle size analyzer (LPSA) with a standard operating procedure (Viton and Sadler 1997). Prior to measurement, organic material was removed from each sample using a hydrogen peroxide solution and was deflocculated using a sodium hexametaphosphate solution. Although there was virtually no organic material or particles smaller than a very fine sand, these steps were taken to ensure that guidelines were followed for all

samples. The Mastersizer 2000© LPSA is capable of measuring particles up to two millimetres. No grains larger than two millimetres were present in any of the samples. Grain sizes are calculated by the LPSA volumetrically and binned into narrow grain size ranges. This generates a probability density for each grain size range from which GSD properties are determined.

2.3.2. Abra Pomez, Argentina

No physical samples were acquired from megaripple stripes at the Argentina site. However, close-range images of the surface sediment on megaripples and on smaller bedforms in the intervening corridors were acquired with a consumer-grade camera in 2014 and 2015. The images were acquired at a height of approximately 20 cm above the surface and slightly stossward of the crests to limit geometric distortion. A ruler was positioned in each image for scaling. Each image was calibrated using OpenCV image calibration software to correct for the slight fisheye effect inherent in most consumer-grade digital cameras. The locations of each of the images from Abra Pomez are shown in Figure 2.3A. The method of extracting measurements of grain diameter from images is referred to as ‘photosieving’ (Ibbeken 1986). There are many different photosieving techniques, including some that are fully automated (e.g., Rubin 2004; Buscombe 2013). However, these automated methods have error ranges that were considered intolerable for this research. In this study, a manual technique was applied in which grain boundaries, or perimeters, visible in the imagery were digitized.

To minimize sampling bias in the photosieving process, a random sampling approach was used for which random points were generated on each image and a buffer was generated around each point. Grain perimeters were digitized if any portion of the grain was located inside the buffer area (Figure 2.3B). The radius of the buffers was set to 75 pixels for images from smaller bedform corridors and 100 pixels for images from megaripple corridors. Three to ten buffers were used per image. Total grains digitized per image ranged from 95 to 743. In total, 43 images were used for digitizing: 34 images from

the 2015 photo survey and 9 from the 2014 photo survey. This method generated a dataset of 9780 grains: 5518 grains from megaripple corridors and 4262 grains from smaller bedform corridors.

Grain dimensions were extracted from the polygons using ArcGIS© software. The grain size being reported is the width of the minimum bounding rectangle capable of containing the digitized polygon. The length of the rectangle can be interpreted as describing the primary axis of the grain and its width the secondary or b-axis. As grain size is typically measured as the latter (i.e., sieve size) by most methods, this is reported as grain size here.

The photosieving method used here is more complex than many other manual methods. Most methods task the user with simply estimating the intermediate axis with a digitized line. However, drawing polygons and automating the axis calculation likely eliminates a significant portion of user bias and is capable of outputting other geometric features of the grains, including their long axis, surface area, and the orientation of the axes. These geometric features could be used to generate estimates of roundness or orientation of grains that may be of value in other applications.

2.3.3. Grain Size Analyses

2.3.3.1. Statistical Methods for Evaluating Grain Size

Descriptive statistics for the grain size data were calculated for both the LPSA data and the photosieved data. These two datasets are of a different nature. The LPSA data are a volumetric probability density and the photosieving data are a distribution of discrete grain sizes. A two-sample difference of means t-test was used to compare the grain sizes of corridor types at the Oceano Dunes and Argentina. This simple statistical test is used establish the difference in grain size between corridor types observed in the field and to test the first hypothesis presented above. In addition, because of the bimodal and non-normal distributions of many samples, a non-parametric equivalent Mann-Whitney U test was also used on the datasets from both locations to reassess this statistical distinction. Finally, the sampling mean

distributions were determined for both the Oceano Dunes and Abra Pomez as another way to show the sorting between corridor types.

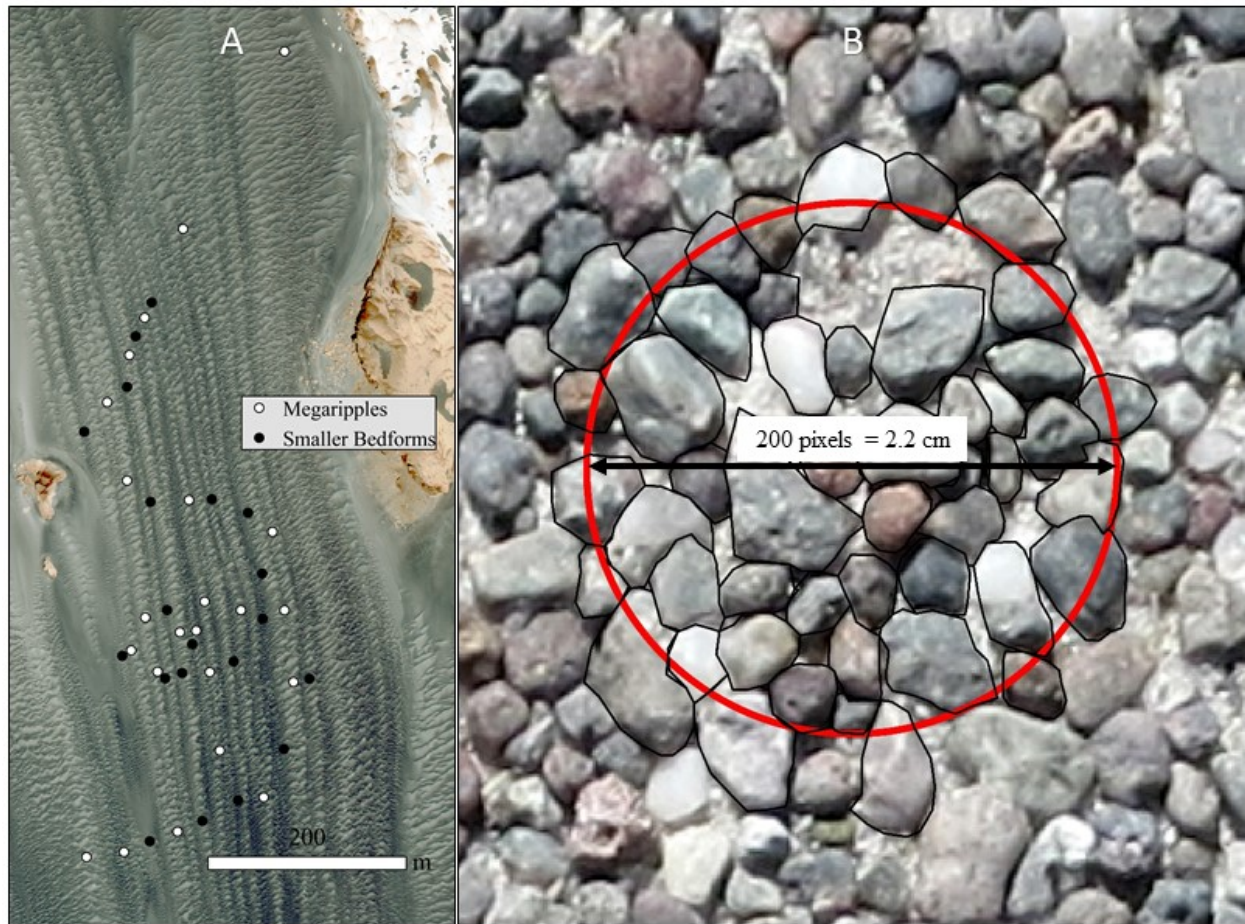


Figure 2.3: *A) Locations of the 43 images used for photosieving (23 from megaripple corridors and 20 from smaller bedform corridors). B) Example of a buffer and polygon-drawing method used for photosieving of a megaripple stoss slope image with a buffer diameter of 200 pixels.*

The spatial distribution of the images sampled from Abra Pomez allowed for the use of a limited set of geostatistical analyses. The objective of these analyses was to test if there is a detectable downwind fining of grain size or other spatial trends in the data. To accomplish this, the mean grain size of each image was paired to the location of the image. Simple linear regression was performed where the northing, in UTM coordinates, of the image was used as the independent variable and the mean grain size

sampled from that image was used as the dependent variable. As the megaripple stripes have a general north-south trend, the northing served as an adequate proxy for the dominant transport direction. Two regressions were performed: one using the megaripple corridor images ($n = 23$) and another using the smaller bedform corridor images ($n = 20$).

A simple measure of the separation in grain size between corridor types was developed. Each image from a megaripple corridor was paired to the nearest image from a smaller bedform corridor. The following normalization calculation was applied to all images from megaripple corridors to determine a relative sorting index between corridor types:

$$Sorting\ Index = \frac{\bar{X}_C - \bar{X}_F}{\bar{X}_C} \quad [6]$$

where \bar{X}_C is the sample mean of the megaripple corridor image and \bar{X}_F is the sample mean of the smaller bedform corridor image. As with grain size, a simple linear regression was performed with the UTM northing and this sorting index to determine if there is a spatial trend in the relative sorting between corridor types.

A global polynomial interpolation, using a simple first-order polynomial (i.e., a plane), was performed using the Geostatistical Analyst tools in ArcGIS©. A ‘grain size score’ was calculated for all sample images relative to the mean of their given corridor type in order to normalize the differences in grain sizes so that all images could be used in a single calculation:

$$Grain\ Size\ Score = \frac{\bar{X} - \mu}{\sigma/\sqrt{n}} \quad [7]$$

where \bar{X} is the sample mean of the given image, μ is the mean of all sampled grains from the given corridor type, σ is the standard deviation of all sampled grains from the given corridor type, and n is the number of images from the given corridor type. The resulting grain size scores were then used to perform the global polynomial interpolation on all megaripple corridors and the data to test for a downwind fining

trend. The grain size score may be interpreted as a standard score based on the standard error of the mean, where ± 1 is indicative of 1 standard error above or below the mean, respectively.

2.3.3.2. Commensurability of Photosieving Data

It is important to clarify that grain size data derived from photosieving are an approximation of true grain size. Digitized grain boundaries are not the actual grain boundaries because there are several confounding factors: shadowing, pixel size, imbrication of grains, packing, and several other issues (e.g., O'Brien and McKenna Neuman 2018). Therefore, photosieved grain size is relative. It is recognized that the use of photo-based and laser diffraction methods in combination makes the direct comparison between grain size at the two field sites difficult. However, the objective of this research is to quantify only the relative difference between corridor types at individual sites; cross-site comparisons of grain size are a future research objective. As the method used for comparing corridor types is consistent at each site, concerns about establishing the relative difference in grain size between corridor types at each individual site are abated.

A secondary benefit to using a photo-based method is that it allowed for an evaluation of photo-based grain size analysis, as these methods are growing in popularity and increasingly being used to quantify grain size on Mars (e.g., Jerolmack et al. 2006, Weitz et al. 2018). As in Jerolmack et al. (2006), the GSDs presented for Abra Pomez are based on grain counts rather than mass or volume. This was done because estimating the mass distribution of the grains in Argentina is impossible due to the varying densities of the surface grains. The complex geology of the region means that the grains being transported are of varying densities, including pumices $< 1000 \text{ kg/m}^3$ and basalt grains $\sim 3000 \text{ kg/m}^3$ (de Silva et al. 2013). This presents an enormous complication in understanding the nature of aeolian transport in the region (Hugenholtz et al. 2015), and equations such as those presented in Chapter 1 use a single density value. The complexity of aeolian transport in areas with multiple lithologies is under-researched, and the simplifying assumption of equal densities is often made despite the inaccuracies that such an assumption

introduces. For this reason, even if physical samples were available from megaripple stripes in Argentina, a direct comparison between the primarily quartz samples from Oceano and those collected in Argentina would not be feasible because of the different grain densities in each sample. Finally, although the photosieving method used may be incommensurable with other methods, it does provide an estimate of the surface grain size, preserves the original orientation and structure of the bedform surface, and is essential for evaluating a GSD when no other data or samples are available (Buscombe 2013).

2.4. Numerical Modeling

Aeolian bedform modelling is a well-developed research domain, and modelling efforts can be broadly separated into two branches: analytical and numerical. Analytical modelling approaches can be understood as the development of a system of equations describing the properties of a fluid or fluid-sediment system, which are solved for some unknown property (Jackson and Hunt 1975; Yizhaq et al. 2004; Narteau et al. 2009). Ripples can be modeled analytically by use of functions that represent their properties and the processes that cause them to emerge (Anderson 1987; Yizhaq et al. 2004; Durán et al. 2014). Numerical modelling has similar goals to analytical modelling but takes a stochastic approach to understanding bedform evolution. Numerical models in aeolian research are often based on cellular automata, which have discrete units that move in a model space according to a fixed set of rules (Werner 1995; Nield and Baas 2008). The degree of complexity of these rules is usually kept to a minimum to make model outputs easier to interpret. These models can be beneficial for understanding bedform evolution as they often allow for visualizations to be output during the model run. Further, numerical modelling can incorporate probabilistic elements that cause different outputs to emerge from the same initial state (Werner 1995). This makes CA modelling far less deterministic than analytical modelling and allows for variation in bedform evolution, which arguably make CA models better replicas of bedform-scale geomorphic processes (Baas 2007). CA models are an excellent exploratory tool and serve as an important method in taking a reduced-complexity approach to bedform modelling (Barchyn and Hugenholtz 2012). They have been used to successfully reproduce ripples and dunes, and they have

produced new insight into aeolian bedform evolution and morphodynamics (Anderson and Bunas 1993; Werner 1995; Kocurek and Ewing 2005).

An unpublished numerical model developed by Thomas Barchyn, University of Calgary, was used for this component of the thesis project. The ‘Mantled Gravel Dunes’ (MGD) model draws on concepts embedded in previous CA models to reproduce bedforms and aeolian processes. As with previous aeolian CA models, MGD uses a rule-based, probabilistic approach with user-defined parameters to avoid the complex physics and intensive computational demand of discrete element (i.e., individual grain) and analytical modelling. Despite these simplifications, with the appropriate parametrizations MGD is capable of reproducing aeolian bedforms formed by saltation and reptation processes with a high degree of verisimilitude. At the bedform scale Werner (1995) showed that variations in grain-scale processes and small variations in fluid flow are ‘slaved’ to larger scale processes that can be readily represented by slabs. This is a primary reason why MGD, which is also based on the concept of slabs, was used to simulate the formation of megaripple stripes.

The MGD model uses a three-dimensional grid space of user-defined x , y , and z dimensions. Each grid cell in the model can be occupied by either a slab or empty space. Slabs are the base unit of the model and represent packages of sediment with x , y , z dimensions of 1, 1, 0.1. All model outputs described below are reported in these slab units. For example, a z elevation of 0.7 is simply reported as ‘7 slabs’. The user can create multiple slab types, set the proportion of each type in the model, and specify the properties and behaviours of each slab type. The base of the model space behaves as a non-erodible substrate. The grid space represents arbitrary dimensions and the model space can thus be understood as representing fine-scale impact features or dune-scale features. In all simulations, transport always occurs in a single direction (left-to-right) throughout the model run in order to replicate the unimodal transport environment thought to be necessary for megaripple stripe formation and development.

The model workflow loop begins by selecting a random x , y location in the model space. The x represents the downwind direction and y represents the crosswind direction. The highest z -value (surface)

slab at that location is selected. If a slab is selected, it is transported according to its ‘erosion likelihood’ value. For example, a cell with an erosion likelihood of 0.5 will be transported half the time it is selected. In this way, ‘erosion likelihood’ serves as a proxy for grain size. Additionally, the erosion likelihood value is automatically set to 0 if the x, y coordinate falls in the shadow zone, which is defined as a cell that falls in the area of a 15-degree (from horizontal) downward line traced downwind from any topography (Werner 1995). If transport is initiated, the model calculates a ‘deposition jump’ path through the model space for that slab. This path is user-defined for every slab type and includes x, y , and z coordinates for each step through the model space so that the slab may be intercepted by any topography before its trajectory is completed. The model also incorporates an avalanche function that causes slabs to be moved if a transport event causes a slope to exceed the angle of repose (30 degrees). After all movement has ceased, the model repeats the workflow loop for a user-specified number of iterations. One iteration is defined as a round of x times y workflow loops in the model space (e.g., one iteration in a 400 x 400 model space is 160 000 workflow loops). Model outputs include a plan-view visualization of the model space, a log of the surface distribution of slab types, a log of surface elevation (z) at each x, y coordinate, and can also include transect views through the model space in the downwind or crosswind direction.

2.4.1. Model Parameters

MGD offers users a high degree of customizability, and multiple types of slabs can be specified. MGD operates using three customizable files: the ‘slabfile’, the ‘cubeconfig’, and the ‘simfile’. Each of these files allows the user to set the properties of the slabs, the size of the model space, and the behaviour and length of the simulation, respectively.

The customizability of MGD allowed for several hundred modelling iterations to be run to test the effects of different parametrizations. Central to the modelling was the adaptation of the two-species approach, which has been shown to be essential to megariipple development (Lämmel et al. 2018). It was

considered that if the two-species approach is important for megaripple development, it must also be important for megaripple stripes. Accordingly, two slab types were defined: ‘saltons’ and ‘reptons’. The objective was to create simple rules that would cause these slab types to behave similarly to reptons and saltons in the natural environment. These behaviours include a very short transport length and low transport probability for reptons, and a long transport length and high transport probability for saltons. Through testing hundreds of parametrizations, it was found that a relatively narrow range of parameters was capable of consistently reproducing megaripple stripes. Parameterizations of saltons and reptons used in a typical simulation that produced megaripple stripes are shown in Table 2.1.

Table 2.1: Example of MGD parameters used to reproduce megaripple stripes.

Parameter	Slab Type (‘Species’)	
	Repton	Salton
% in Model Space (bulk distribution)	3.5	96.5
Advection Distance (cells per hop)	3	30
Erosion Likelihood (%)	20	100
Probability of Spanwise Transport	0.66	0.1

2.4.1.1. Model Space

Transport in the model space is unimodal (left-to-right). A model space, or ‘cubeconfig’ of 400 x 400 x 400 (x , y , and z dimensions) was used for most simulations. This creates 64 million cells in the model. Due to computational limitations, a larger model space was impracticable. An initial uniform unconsolidated sediment depth of 200 slabs was used in the majority of simulations. This means that the model’s initial state is a random, featureless distribution of 32 million slabs below 32 million empty cells. The bottom of the model space serves as a non-erodible substrate and the top of the model is a cap on the model space—if a slab is deposited that would cause the model to exceed a z -value of 400, then the model ceases operations. This hard cap was due to computational limitations, but also served as a useful stopping point for simulations that produced unrealistically large features. In exploratory simulations

testing model behaviours, a smaller or wider model space with fewer slabs was used to more rapidly assess the changes caused by altering parameters or to constrain effects of model space size.

As with the Werner (1995) model, the borders of the model space are continuous, such that if a slab exits the model space it returns to the model space on the opposite boundary. This is the case for both the ‘downwind’ and ‘crosswind’ boundaries. No new slabs are ever removed or introduced into the model space during the simulations, and therefore the total number of extant slabs remains unchanged throughout the model run.

2.4.1.2. Transport Lengths

It is understood that the transport length of a saltating grain is significantly larger than that of a reptating grain (e.g., Vallance et al. 2015). The minimum practicable hop length of a slab in the model is 3 cells. Consequently, the repton slabs were set to a hop length of 3 cells. To scale the significantly longer hop length of saltating grains, salton slabs were given a hop length of 30 cells. Although a ratio of 10:1 may be an underestimation of the difference between these two transport processes in a natural setting, the salton hop length could not be set to a significantly larger value without saturating the model space and allowing for the formation of only one or two bedforms. Further, it will be shown that the ratio of wavelengths of megaripple and impact ripple corridors produced in the model space compare closely to those observed in natural megaripple stripes despite this seemingly low ratio.

2.4.1.3. Percentage of Reptons and Saltons in Model Space

The percentages of reptons and saltons in the model space can be set by the user. For example, there are 1.6 million repton slabs in a model space of 400 x 400 x 400 cells when the percentage of reptons is set to 5% and the unconsolidated sediment depth is set to 200. This would result in an expected initial value of 8000 repton slabs in each layer of the model, including the surface. As ripples develop over time, however, the percentages of reptons present at the surface increases. This coarsening process is

essential to megaripple development (Lämmel et al. 2018). The changing surface concentration of reptons was therefore recorded at regular intervals of 50 iterations during model runs.

2.4.1.4. Erosion Likelihood

The erosion likelihood is the probability of a slab being transported when selected. It was established that the erosion likelihood would be set to 100% for salton slabs, as this limits the amount of iterations required for bedform development. The erosion likelihood for repton slabs was therefore the parameter of interest, as the transport frequency of reptons relative to saltons was determined to be a primary factor in the development of the armour layer that is characteristic of megaripples. If the transport frequency is set too low, reptons are trapped in the troughs of impact ripples and megaripples cannot develop. Conversely, if it is set too high, armour layers cannot develop because the high transport frequency results in the removal of the armouring slabs. One limitation of the model is that the erosion likelihood remains constant regardless of slab location in the model space (with the exception of the shadow zone described above). Because of this, a repton slab present at the crest of a megaripple has the same erosion likelihood as a repton present at the base of a megaripple. This is not reflective of natural megaripple processes, where it is understood that grains at the crest are transported much less frequently because they are subject to significantly fewer impacts from saltating grains (Yizhaq et al. 2012a). Although this lack of verisimilitude did not affect the initial formation of megaripples and megaripple stripes, it increased the rate at which they expanded and gave them a relatively short lifespan in the model. This issue will be addressed in more detail in Chapters 3 and 4.

2.4.1.5. Spanwise Transport

Although knowledge of the precise distribution of spanwise transport remains poorly constrained, it is understood that reptons are transported with a larger spanwise component than saltons (O'Brien and McKenna Neuman 2016). To account for this observation, both slab types were given a fixed probability of moving one grid cell to the left or right in the model space. This allowed for the testing of spanwise

transport of grains as a mechanism leading to megaripple stripe development and the observed textural difference between corridor types.

Two important factors control spanwise transport behaviour in MGD: the user-defined probability of spanwise transport, $P(\theta)$, and the spanwise angle of transport, θ .

$$\theta = \tan^{-1} \frac{\text{Spanwise Transport Length}}{\text{Downwind Transport Length}} \quad [8]$$

For simplicity, the spanwise transport length is one cell in all simulations (one cell to the right or one cell to the left). This gives each slab type only three possibilities for spanwise transport: 0 and $\pm\theta$. The probability of transport to the right or left by a single cell is simply $P(\theta) / 2$, and $1 - P(\theta)$ is the probability of no spanwise movement. Because the downwind and spanwise transport length in MGD are held constant in situations where there is no topographic interference, the position of a repton in the model space can be understood as a simple random walk model in one dimension. As an example, the probabilities associated with a repton's position in an idealized model space after a given number of steps is shown in Table 2.2. This idea will be expanded upon in §4.5.2.

Table 2.2: Probabilities of a repton with $P(\theta)$ of 2/3 being at a given spanwise position after a given number of steps.

		Spanwise Position								
		-4	-3	-2	-1	0	+1	+2	+3	+4
Steps	0					1				
	1				1/3	1/3	1/3			
	2			1/9	2/9	3/9	2/9	1/9		
	3		1/27	3/27	6/27	7/27	6/27	3/27	1/27	
	4	1/81	4/81	10/81	16/81	19/81	16/81	10/81	4/81	1/81

2.4.1.6. Spatial Autocorrelation Analysis

In addition to recording the changing surface concentration of reptons, the spatial autocorrelation of the reptons was found to be predictive of megaripple emergence. Reptons in the model space were

assigned a value of 2 and saltons a value of 1 to facilitate the calculation of spatial autocorrelation statistics. A log of the Global Moran's I of the surface layer of sediment was calculated in ArcGIS© to evaluate the evolving spatial autocorrelation of the entire surface layer. Additionally, to model local developments of high concentrations of repton, a Getis-Ord G_i^* statistic was calculated. Both statistics were logged at 50 iteration intervals. Moran's I is a single metric assessment of spatial clustering and was used to evaluate the entire model space (Moran 1950). The Getis-Ord G_i^* statistic is a measure of local spatial autocorrelation (Getis and Ord 1992). In this analysis, the neighbourhood of an individual slab was defined as a 12 x 12 kernel surrounding the slab (i.e., the slab under consideration and the 143 slabs surrounding it are its 'neighbourhood'). The value of this kernel is calculated where all salton slabs are given a value of 1 and repton slabs a value of 2. For example, a kernel with 20 repton and 124 saltons has a value of 164. This value is then compared to this same kernel value for all other slabs in the kernel by subtracting the mean kernel value and dividing by the standard deviation. In this way, the Getis-Ord G_i^* can be interpreted as a Z-score; a G_i^* statistic of 4 indicates that a given slab's kernel is 4 standard deviations above the mean value of the other slabs in the neighbourhood. As there are 160 000 slabs on the surface layer of the model space, 160 000 kernel values and G_i^* statistics are calculated and plotted. This allows for the visualization of 'hot' and 'cold' spots in the model space associated with high local concentrations of repton and saltons, respectively.

2.4.2. Evaluation of Model Verisimilitude and Comparison to Natural Megaripple Stripes

A challenge for bedform classification and modelling is the determination of objective measures capable of comparing modelled and observed natural features and then sorting them into distinct classes. Establishing objective measures is in many cases not possible, and there is a reliance on relative and qualitative comparison. Megaripple stripes are no exception to this, and this analysis relies on three characteristics of megaripple stripes to compare modelled and natural megaripple stripes: differential wavelengths and amplitudes of bedforms between corridor types, as well as a grain size distinction between corridor types. A comparison between the morphometrics of the megaripple stripes output by the

model and those observed in imagery and by photogrammetry was therefore essential for validating the model outputs. As the model does not have explicit spatial units, a relative comparison of wavelengths between the morphometrics of modelled outputs and observation was required. Grain size is not a parameter directly simulated by the model. As grain size and density are variable between the documented stripe locations, the model's verisimilitude is reliant on making simplifying assumptions about the relative behavioural differences caused by grain size and density. As addressed, these differences are substantial in the case of differential density at Abra Pomez. Nevertheless, slab type sorting was easily observable in the modelling outputs because repton slabs representing the behaviour of larger grains accumulate on megaripple crests.

2.4.2.1. Wavelength, DSM, and Ripple Height Comparison

The different wavelengths and heights between corridor types is an essential characteristic of megaripple stripes. Ratios of wavelength and height between the megaripples and smaller bedforms measured at the Oceano Dunes were compared to those observed in model outputs. Due to the limitations of the model space, only the downwind wavelengths could be reliably compared. The basis for these comparisons is the 3D output of the model space and the 3D output from the photogrammetric reconstructions of the Oceano Dunes. As with transect measurements made from the 3D reconstructions at Oceano, the 3D Analyst toolbox in ArcGIS© was used to measure wavelengths and heights of features in the model space.

Chapter 3: Results

3.1. Overview

Results from the morphometric analyses, grain size analyses, and modelling are included in this chapter. It is shown that a characteristic ratio of downwind wavelength and crosswind wavelength exists in megaripple stripes. There is also a clear distinction in grain size between the corridor types at the Oceano Dunes and at Abra Pomez, Argentina. Overall, results suggest that megaripple stripes are characterized by two corridor types with distinct GSDs and bedform length scales. Megaripple corridors have larger amplitude and wavelength bedforms characteristic of megaripples. Smaller bedform corridors have features with properties more similar to impact ripples, but often with some megaripple characteristics. The numerical modelling results suggest that megaripple stripes emerge in conditions of supply-limited repton when local patches containing high concentrations of reptons develop on the surface. The outputs of the numerical modelling are shown to resemble the observed wavelengths, heights, and patterning of megaripple stripes at the Oceano Dunes, California.

3.2. Wavelengths

Wavelength measurements made at each site are shown in Table 3.1. The megaripple corridors at most locations have downwind wavelengths of 2 to 3 metres, with much larger features present at Abra Pomez and Mars. The smaller bedforms in the intervening corridors are very difficult or impossible to identify in satellite imagery and could only be measured at two sites. On Mars, the wavelengths of these smaller bedforms were measured from satellite imagery and at the Oceano Dunes they were measured in the field.

The data in Table 3.1 suggest the crosswind wavelength of megaripple stripes is approximately two times larger than the downwind wavelength of the megaripple corridors (Figure 3.1). A simple linear regression for the terrestrial and Martian stripes yields an R^2 of 0.97 for these data, but further data and field research are required to test and reinforce this relationship. This is especially true given that there is

a paucity of data for megaripple stripes that are too small to resolve in satellite imagery (i.e., wavelengths < 2 m). An important caveat to results in Table 3.1 is that the downwind wavelengths estimated from the satellite imagery are likely an overestimation because some crestlines may not be detectable in the imagery. Further, there is spatial variability in the crosswind and downwind wavelengths throughout the megaripple stripes and the 2:1 ratio is only representative as an average. The average coefficients of variation of the downwind and crosswind wavelengths measured from imagery were 0.17 and 0.18, respectively. This suggests that although there is a larger range of values for the spanwise wavelengths (0.9–28.5 m) than the downwind megaripple wavelengths (0.3–8.8 m), the relative variability of downwind and crosswind wavelengths is virtually the same.

Table 3.1: Mean values from wavelength measurements of megaripple stripes from the field (Oceano Dunes) and imagery (all other locations).

Location	Sample Points	Smaller Bedform Corridor Wavelength (m)	Megaripple Corridor Bedforms Measured	Mean Megaripple Wavelength, \pm St. Dev. (m)	Crosswind Wavelengths Measured	Mean Spanwise Wavelength, \pm St. Dev. (m)
Oceano	N/A	0.10	142	0.33	36	0.90
Namibia	24	N/A	164	2.37 ± 0.15	76	3.61 ± 0.52
China	32	N/A	216	2.59 ± 0.29	160	5.86 ± 0.73
Iran (North)	56	N/A	772	2.85 ± 0.61	224	5.08 ± 1.31
Iran (TARs)	92	N/A	1139	8.78 ± 2.33	477	28.50 ± 8.70
Peru (Inland)	30	N/A	275	2.91 ± 0.39	255	4.11 ± 0.55
Peru (Coastal)	46	N/A	590	2.99 ± 0.31	376	4.94 ± 0.49
Argentina	103	N/A	859	6.92 ± 1.55	515	17.05 ± 3.68
Mars	21	3.41	153	8.83 ± 2.84	87	23.88 ± 3.10

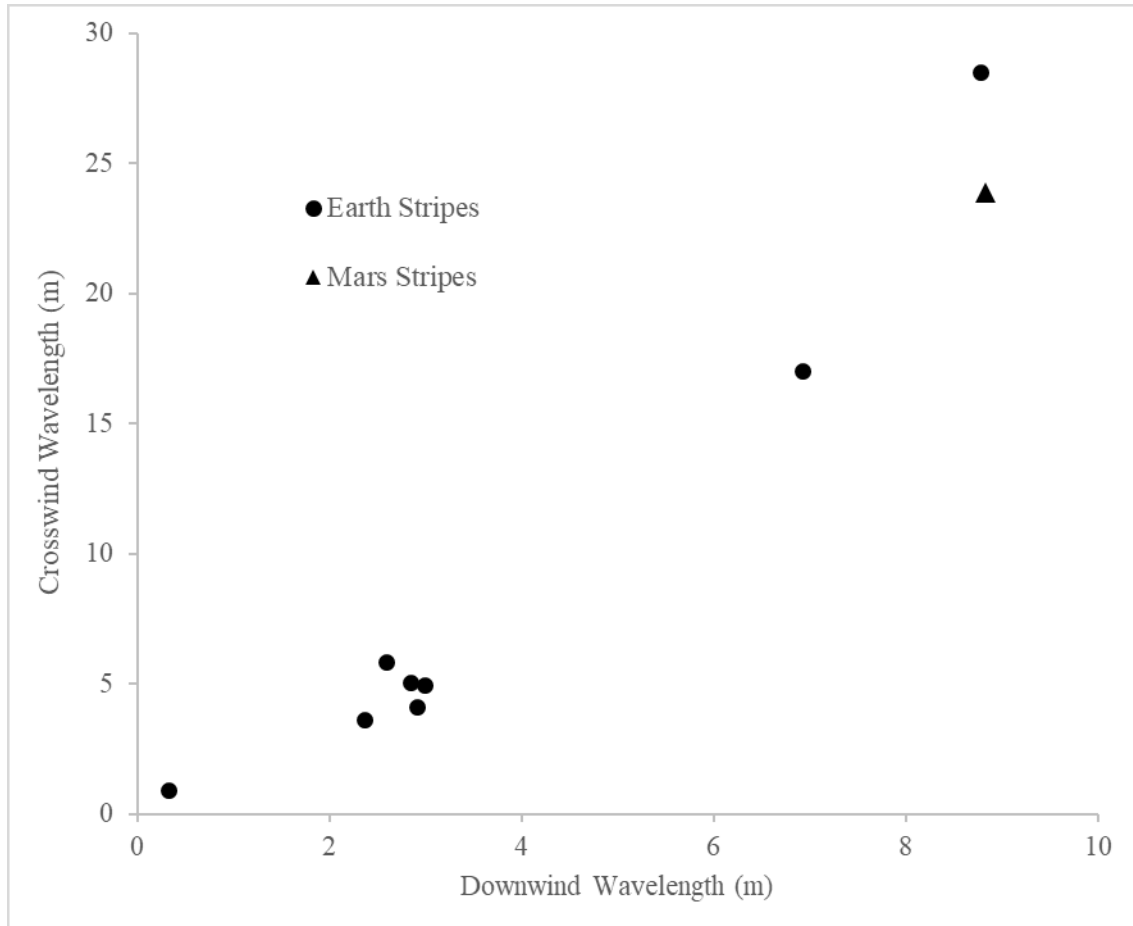


Figure 3.1: Averaged crosswind and downwind (megaripple corridor) wavelengths of measured megaripple stripes on Earth and Mars. A two-to-one crosswind-downwind wavelength ratio appears to exist for megaripple stripes.

3.3. Grain Size

3.3.1. Oceano Dunes, California

Grain size data for surface and depth samples of the megaripple stripes at the Oceano Dunes were aggregated to the level of megaripple corridors and smaller bedform corridors (Table 3.2). Tabular results from all individual samples are shown in Appendix A. The results of a two-sample t-test and a Mann-Whitney U test between the means of all megaripple corridor and smaller bedform corridor samples confirm a statistically significant difference in grain size between corridor types for both surface and depth samples with $p < 0.01$. This grain size distinction is observed at all four sampling sites (Figure

3.2A). To further emphasize the distinction between corridor types, sample means for all depth samples were rounded to the nearest 50 μm and plotted in Figure 3.2B.

Examples of the typical distributions observed in the samples are shown in Figure 3.3. For both corridor types, the surface samples were found to be coarser than the depth samples. This is expected in megaripples, where coarsening is observed with smaller sampling depths (Yizhaq et al. 2012a). This suggests that the features in the smaller bedform corridors have some megaripple characteristics (i.e., armouring) despite their smaller wavelengths. Depth samples generally have a larger standard deviation and range than the surface samples. Importantly, only three of the seventy samples showed a bimodal distribution, with all other samples being distinctly unimodal and largely log-normally distributed. This does not reflect what has typically been reported for megaripples, where it is often stated that a bimodal GSD is required for their formation (Yizhaq et al. 2012a). However, as addressed by Lämmel et al. (2018), only poorly sorted grains may be required for the initiation of megaripples. Although only three samples showed a bimodal distribution, the distribution of sample means (Figure 3.2B) for depth samples is non-normally distributed and multimodal. This suggests local variability in grain size.

Table 3.2: Aggregated grain size statistics from LPSA data for Oceano Dunes samples. All grain sizes presented are in μm . *Transition area samples were acquired at only two of four sampling sites. Although the grain sizes for the transition areas are smaller than the smaller bedform corridors in aggregate, the transition areas are coarser than the smaller bedform corridor samples from their respective sampling sites.

	N	Mean	D10	D50	D90	Std. Dev.
Megaripple (Depth)	22	713	346	665	1146	82
Megaripple (Surface)	12	724	416	688	1080	46
Smaller Bedform (Depth)	20	393	188	353	660	108
Smaller Bedform (Surface)	6	575	325	541	876	36
Transition (Depth)*	10	273	160	251	403	52

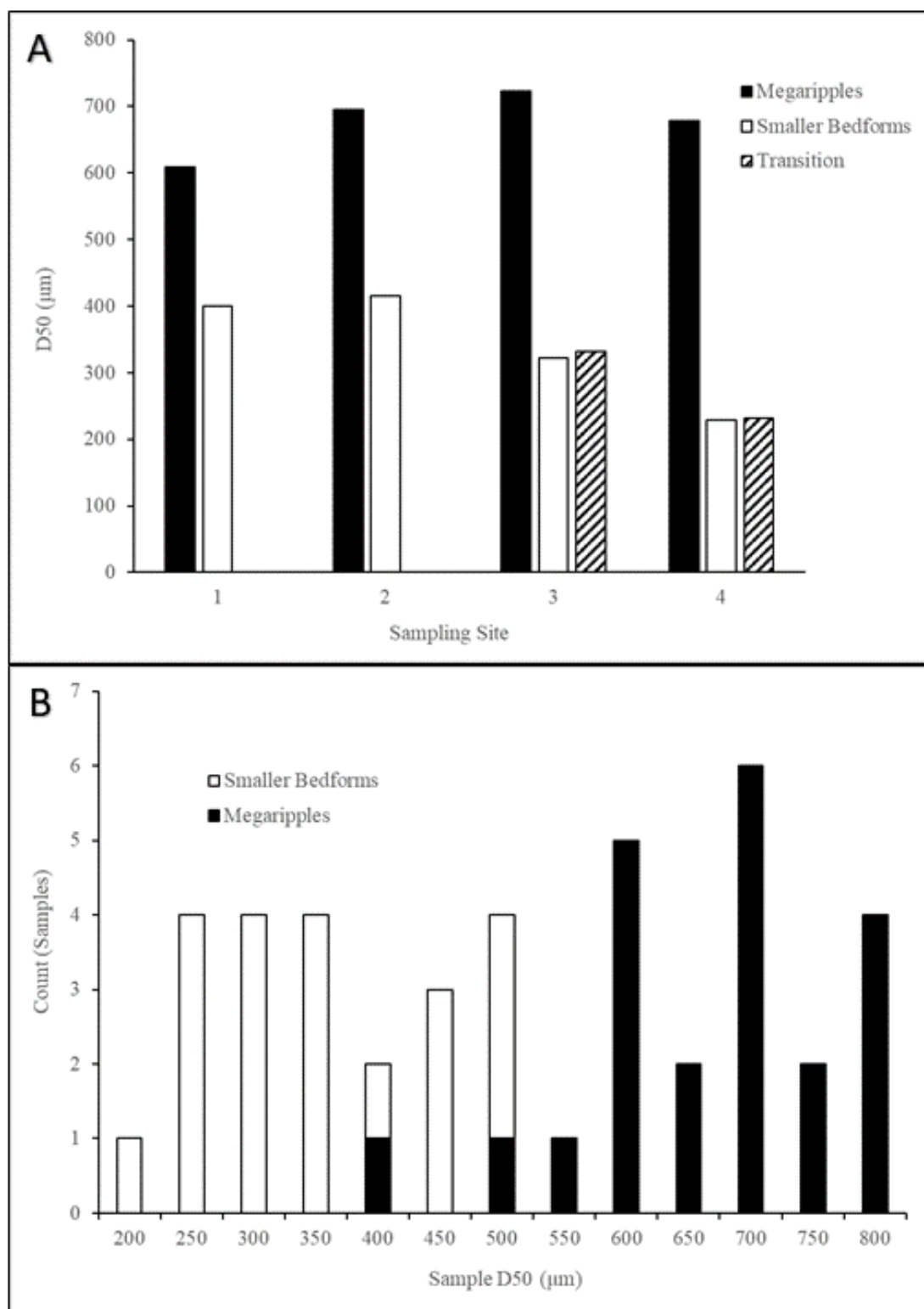


Figure 3.2: *A)* Average D50 of depth samples acquired at four sampling sites at the Oceano Dunes. *B)* D50 values from 42 depth samples acquired from the megaripple and smaller bedform corridors at the Oceano Dunes. D50 values for each sample were rounded to the nearest multiple of 50.

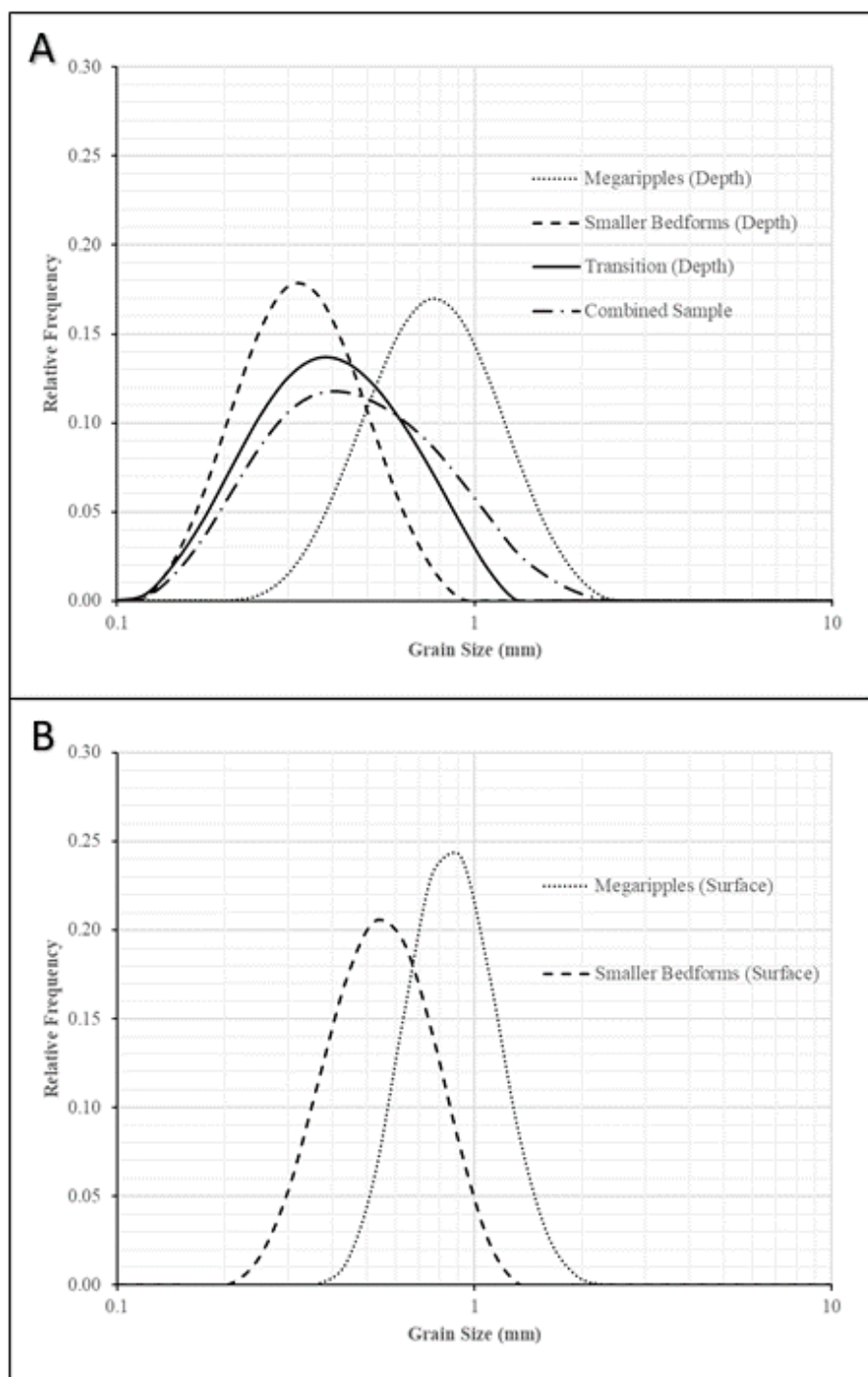


Figure 3.3: Grain size curves for a series of megaripple stripe samples at the Oceano Dunes, California.

A) Three samples acquired at depth from the stoss slopes and crests of bedforms from the megaripple corridors, smaller bedform corridors, and transitional area. Their combined distribution is also shown.

B) Two samples acquired at the surface of bedforms in the same location as A) for the megaripples and smaller bedforms.

3.3.2. Abra Pomez, Argentina

As with the Oceano Dunes, megaripple stripes in Argentina show a distinct sorting of grain size between megaripple and smaller bedform corridors. Results from the photosieving analysis are shown in Table 3.3 and Figure 3.4. As the photosieving data for both the smaller bedforms and the megaripples are non-normally distributed and data were generated for individual grains, a Mann-Whitney U test was used to compare the two corridor types from Argentina. This test confirms that there is a statistically significant difference between the megaripple grain sample and the smaller bedform grain sample with $p < 0.01$.

A bimodality is apparent in the aggregated GSD of the megaripple samples, but not in the GSD of the smaller bedforms. Of all the sample images, 14 of 23 megaripple images and 5 of 20 smaller bedform images showed bimodal or multimodal distributions. The sampling mean distribution of the photosieved results is shown in Figure 3.5 and reveals a similar but less complete separation of sample mean distributions between corridor types. As discussed, it is doubtful that these photosieved grain sizes are directly comparable to those collected via physical sampling. It is estimated that the minimum grain size capable of being digitized reliably in these images was 0.5 mm, with some variability between images. Although most of the grains in the images were resolvable, several pockets of what appeared to be small grains could not be digitized. Therefore, the left tails of the distributions presented in Figure 3.4 are not representative. Due to the nature of the photosieving method, reliability increases with larger grains, and it is therefore likely that the right tails of these distributions are representative.

The results of the regression analyses and global polynomial interpolation for testing for a spatial trend in grain size are shown in Figure 3.6. The global polynomial interpolation shows a distinct spatial trend of decreasing grain size. Notably, 15 of the 16 northernmost samples have above-average grain sizes and 19 of the 27 southernmost samples have below-average grain sizes. The regression of absolute grain sizes in Figure 3.6B shows a similar downwind fining trend for both corridor types. The relationship between northing and grain size showed a moderately strong relationship for the megaripples ($R^2 = 0.52$)

and a weak relationship for the smaller bedforms ($R^2 = 0.24$). The regression analysis for detecting a trend in sorting between megaripple and smaller bedform corridors found no relationship between northing and relative sorting ($R^2 = 0.00$) but reveals that there is significant variance in the degree of sorting between corridor types (Figure 3.6C).

Table 3.3: *Descriptive statistics of megaripple and smaller bedform corridors from photosieving of surface grains in Abra Pomez.*

	Smaller Bedforms	Megaripples
Mean (mm)	1.66	2.58
Standard Deviation	0.91	1.21
D16	0.79	1.17
D50	1.45	2.62
D84	2.61	3.77
D95	3.38	4.54
Graphic Skewness	0.14	-0.06

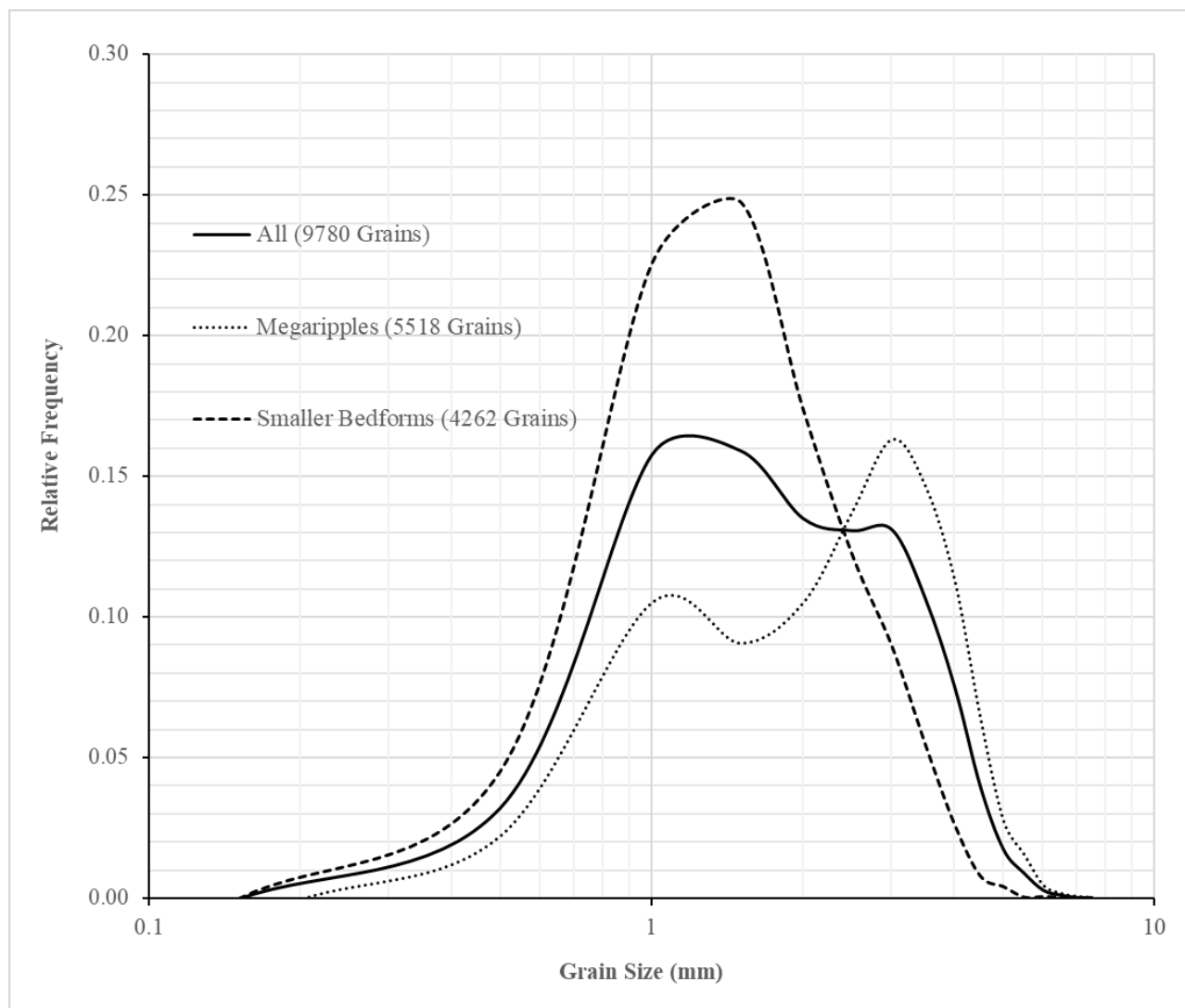


Figure 3.4: Probability density of grain sizes from photosieving for the megaripples, smaller bedforms, and all grains combined.

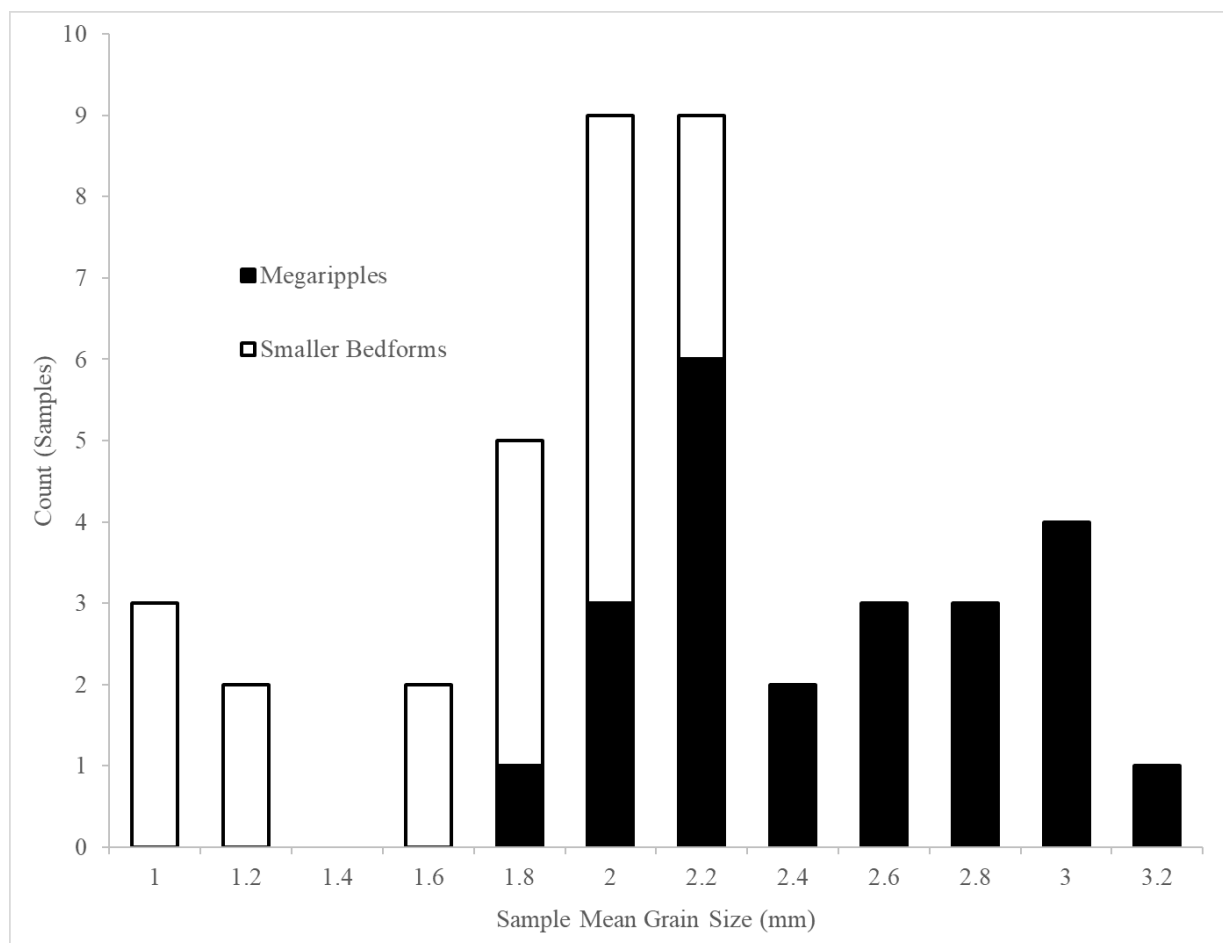


Figure 3.5: Distribution of sampling means rounded to nearest 0.2mm for 43 image samples acquired for the megaripple corridors (23 images) and smaller bedform corridors (20 images) at Abra Pomez, Argentina.

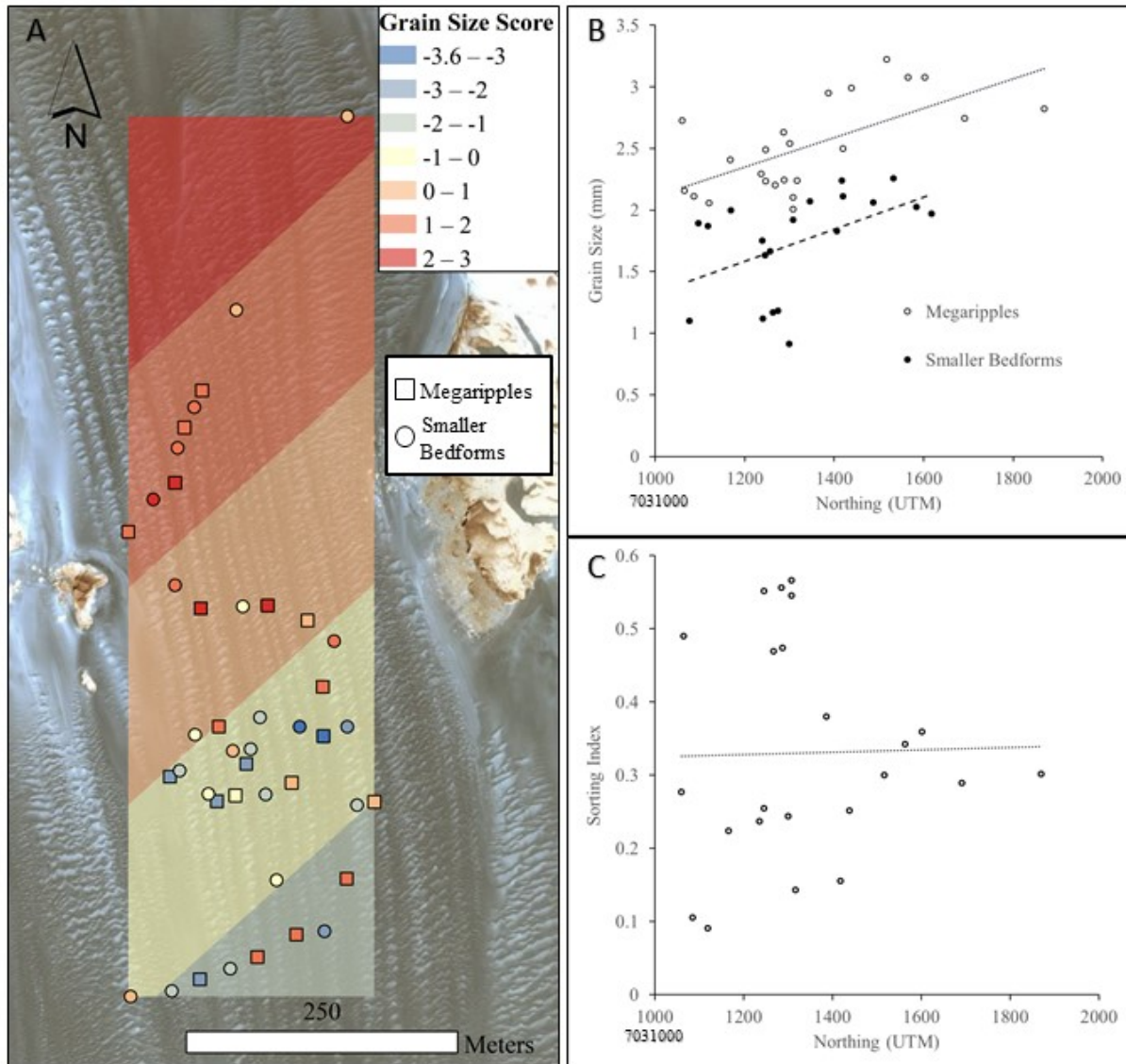


Figure 3.6: *A) A global polynomial interpolation shows a downwind fining at Abra Pomez. Individual points represent photo locations and colour scheme represents the grain size (normalized so that 0 represents the mean and ± 1 is a standard deviation). The direction of fining trend closely matches that of the prevailing transport direction. B) Scatterplot of grain size as a function of northing for megaripples and smaller bedforms. R^2 values of 0.52 and 0.24 were found for the megaripples and smaller bedforms, respectively. C) Scatterplot of sorting index (§2.3.3.1.) as a function of northing. No relationship was found between the relative sorting and northing.*

3.4. Bedform Heights and Planform Morphology

An orthomosaic photo and DSM generated at sample site 3 at the Oceano Dunes are shown in Figure 3.7. Sample transects are shown in Figure 3.8. Morphometrics calculated from transects taken from four DSMs are shown in Table 3.4. Mean bedform heights and wavelengths measured from megaripple corridors were approximately triple and double that of the smaller bedform corridors, respectively. Additionally, the variability observed in bedform heights and wavelengths of megaripple corridors was greater than that observed in the smaller bedform corridors. This larger variability is typical of megaripples (Yizhaq et al. 2009; Yizhaq et al. 2012b). Although there are evidently different dominant scales of bedform present in each corridor, there are bedforms of an intermediate size (10–20 cm) with megaripple characteristics present in both corridor types. The presence of these intermediate forms is likely a consequence of the incomplete sorting of grains between corridors and provides evidence for a continuum of bedform types rather than two distinct classes (impact ripples vs. megaripples) with strictly defined properties.

Table 3.4: Morphometrics acquired from measurements of the structure-from-motion DSMs generated at the Oceano Dunes megaripple stripes. *Note that the wavelength measurements for Oceano reported here do not match those reported in Table 3.1 because these measurements were acquired from different samples and by a different methodology.

		Smaller Bedforms (n = 82)	Megaripples (n = 58)
Wavelength	Mean (cm)	10.65	20.40*
	Standard Deviation (cm)	3.20	8.36
	Coefficient of Variation	0.30	0.41
	Max (cm)	20.10	43.59
Height	Mean (cm)	0.39	1.40
	Standard Deviation (cm)	0.84	0.62
	Coefficient of Variation	0.28	0.44
	Max (cm)	0.74	3.18

The planform morphology of the features in the megaripple corridors is convex relative to the dominant transport direction (i.e., barchan). This curvature is evident in all the imagery of megaripple stripes and appears to be a common characteristic of megaripple corridors. The curvature of the features in the smaller bedform corridors is less consistent, but the ripples generally have a concave shape relative to the transport direction (i.e., parabolic). This concave shape was only observable at Oceano and in imagery of Mars because the smaller bedforms could not be resolved in imagery of the other locations.

The slopes and cross-sectional profiles of features in the megaripple corridors are characteristic of megaripples, which have approximately isometric stoss and lee slopes as well as a smaller wavelength-to-height ratio (Zimbelman et al. 2012). The profiles of the features in the smaller bedform corridors are more typical of impact ripples with shallower stoss slopes and steeper lee slopes. However, the profiles of several bedforms vary from these standards, further suggesting the incomplete sorting of grains between corridor types and the presence of bedforms with intermediate characteristics.

The lowest topographic points in the megaripple stripes are the troughs of the megaripple corridors. The megaripple crests represent the highest point in the stripes. The corridors of smaller bedforms are at a height intermediate between the troughs and crests of the adjacent megaripple corridors (Figure 3.8A). As these data are only available for one location, it is uncertain if these characteristics are typical of megaripple stripes or incidental. However, these topographic characteristics were also reproduced in the modelling of megaripple stripes.

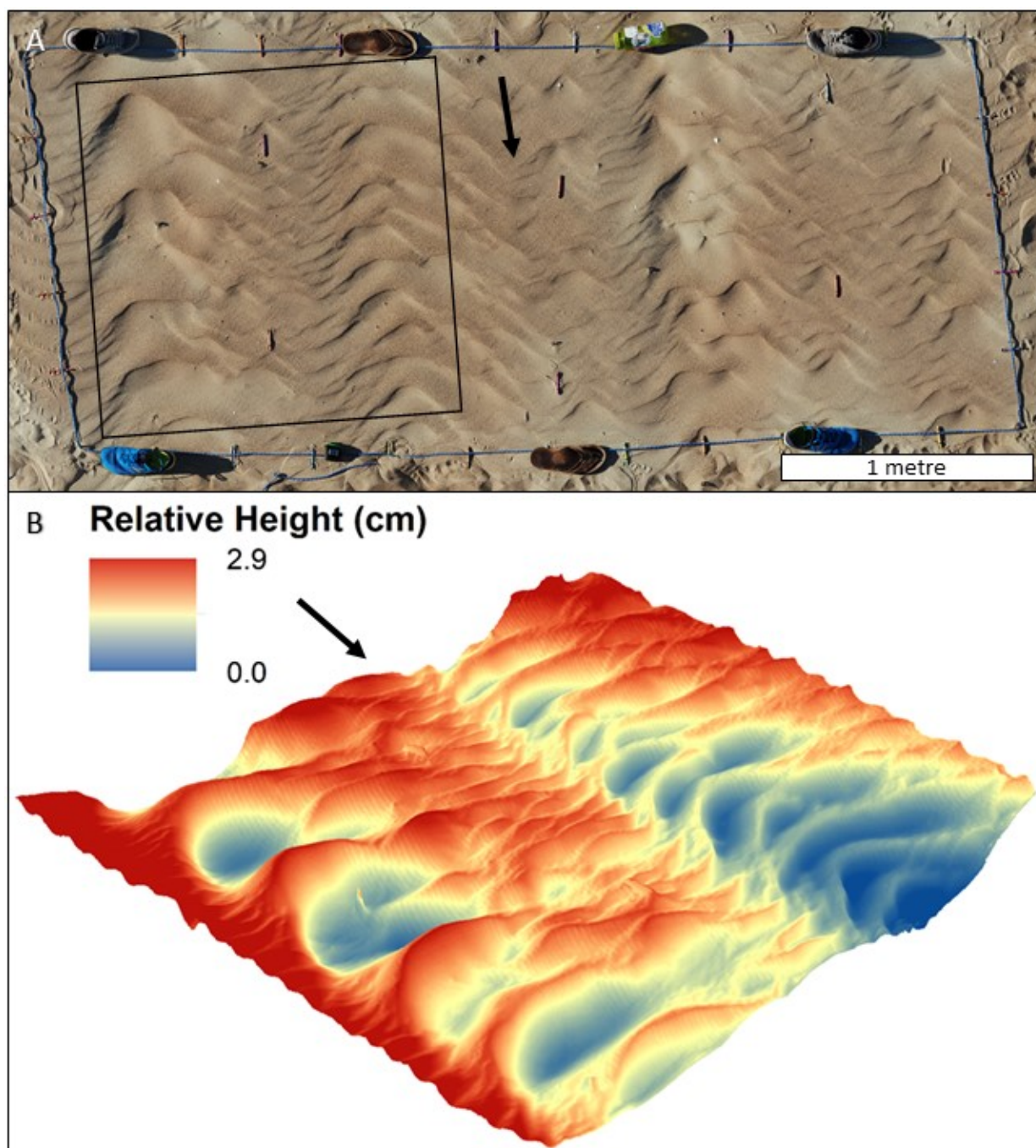


Figure 3.7: **A)** Orthomosaic of megaripple stripes at the Oceano Dunes sample site 3. Arrow shows assumed dominant transport direction. **B)** Sample of DSM from megaripple stripe site 3 at the Oceano Dunes. Inset from A).

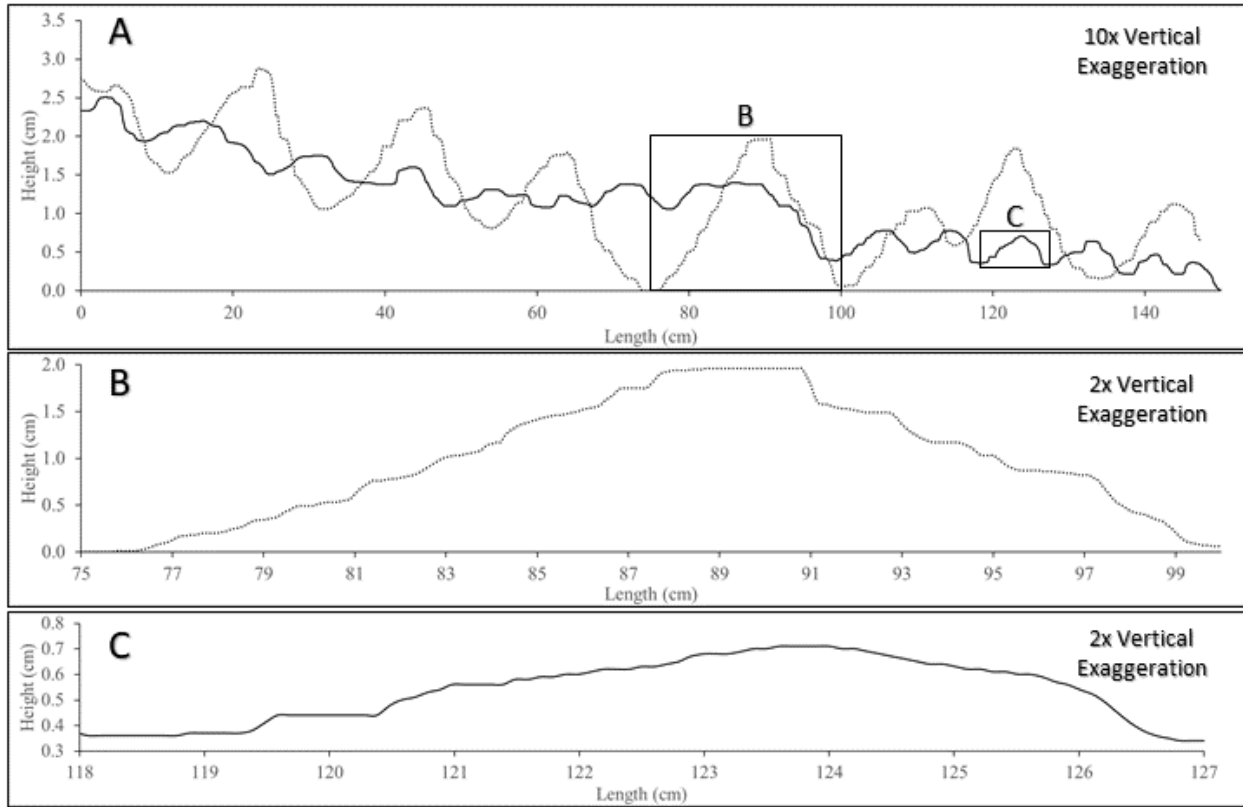


Figure 3.8: *A) Profile graph of megaripples and smaller bedforms extracted from DSM of stripes at Oceano Dunes, California. Transport direction is left-to-right. Overall, these results show that there are large differences in ripple height and wavelength between corridor types. B) Inset of megaripple profile. The stoss and lee slopes are of approximately the same length. C) Inset of smaller bedform profile. The slopes are shallower, and the stoss slope is longer than the lee. Vertical exaggeration in B) and C) is 2, giving the same relative scale and allowing for easier comparison of their profiles.*

3.5. Numerical Modelling

3.5.1. MGD Megaripple Stripes and Parameter Constraints

Megaripple stripes were reproduced in MGD using the parameters outlined in Table 2.1. It was found that a very narrow range of parameters in MGD could reproduce megaripple stripes. Two parameters were essential to controlling their emergence and behaviour. These were the percentages of repton slabs in the model space and the erosion probability of the repton slabs. The probability of spanwise transport and its observed effects on megaripple stripe development are also addressed. After

presenting the effects of these three parameters, an outline of a typical model run that produced megaripple stripes is provided.

3.5.2. Parameters Affecting Megaripple Stripe Formation in MGD

3.5.2.1. Percentage of Reptons Required for Megaripple Stripe Development

The relative percentage of reptons and saltions in the model space was found to be the most important parameter controlling the development of megaripple stripes. Importantly, only a very narrow range of initial repton concentrations led to the formation of megaripple stripes. With too few reptons megaripple nucleation did not occur. Too many reptons caused megaripple nucleation to occur at many locations simultaneously, not resulting in stripe formation. Example simulations with varying initial concentrations are shown in Figure 3.9. It was found that when all other parameters presented in Table 2.1 were held constant, megaripple stripes developed with an initial percentage of reptons between 2.4 and 4.7%. These percentages represent the initial bulk distribution of sediment in the model space. Initial repton concentrations in this range led to the slow development of megaripples at only one or two locations in the model space. This will be addressed in greater detail below. Concentrations from 2.4 to 3.4% only occasionally led to nucleation and required a very long time (7000+ iterations) for stripe development. Concentrations $> 4.7\%$ led to megaripple formation with no striped pattern appearing and concentrations $< 2.4\%$ only led to impact ripple formation. Concentrations from 3.3 to 4.7% most consistently led to stripe formation.

As ripples develop over time, the percentages of reptons and saltions present at the surface change. The concentration of reptons on the surface increases during a megaripple stripe model run. The rate of this increase varies depending on the initial concentration and whether megaripples are developing. This rate of exchange between the bulk distribution of reptons and the surface distribution of reptons was found to be critical to understanding megaripple stripe development, which echoes the findings of Lämmel et al. (2018). The percentage of reptons present on the surface layer of the model

space is therefore found to be closely related to megaripple stripe formation. This changing surface concentration was logged at regular intervals for a series of simulations with varying initial repton concentrations (Figure 3.10).

3.5.2.2. Erosion Probability Required for Megaripple Stripe Development

In these simulations, erosion probability behaves as a proxy for grain size. An erosion probability of 0% is representative of grains too large to be transported, and 100% is representative of grains that are readily transported. As discussed, in the two-species approach used here, saltons are the most readily transported and were given a 100% erosion probability. Because repton slabs are given very short transport lengths, it is important that they be given a low erosion probability so that the behaviours assigned to the slab are in relative agreement. In other words, a slab cannot be given the transport length of a repton and the erosion probability of a salton if verisimilitude is the objective. This required some experimentation. It was found that, with all other model parameters presented in Table 2.1 held constant, repton erosion probabilities of 12–30% were conducive to megaripple stripe formation. Values of 18–24% were found to reproduce megaripple stripes most consistently and with the highest degree of verisimilitude. Values < 12% did not allow for megaripple nucleation because the migration of smaller ripples composed of saltons happened too rapidly for armour layers to develop. Simulations with these low percentages produced features similar to impact ripples moving over a lag deposit. Values > 30% caused very rapid development of large megaripples because of the frequency with which reptons were being transported. This rapid growth was occurring because of the ease with which armour layers could develop under such high-frequency repton transport. Impact ripples did not coexist with megaripples for very long under these conditions.

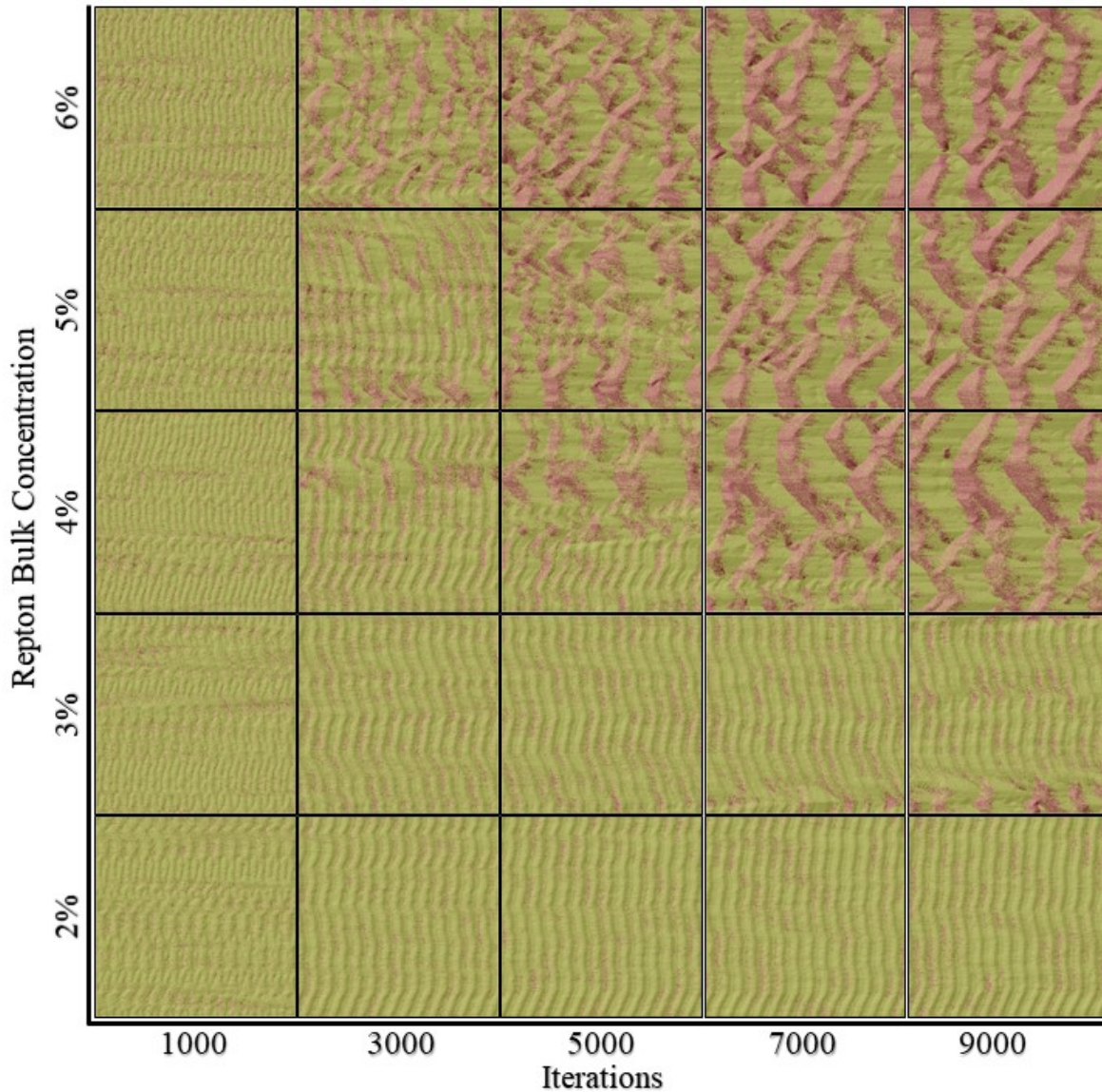


Figure 3.9: Model space visualizations of simulations with 2–6% initial repton concentrations after 1000, 3000, 5000, 7000, and 9000 iterations. Representations of salton (yellow) and repton (red) slabs on the model surface. Transport is left-to-right. Megaripples do not develop at 2% and simple impact ripples migrate through the model space for the entire simulation. At 3%, a small corridor of megaripples has developed in the bottom of the model space after 9000 iterations. After 5000 iterations with a 4% concentration there is a large megaripple corridor. By the end of the model run, megaripples dominate the model space. With initial bulk concentrations of 5% and 6%, megaripples develop rapidly throughout the model space.

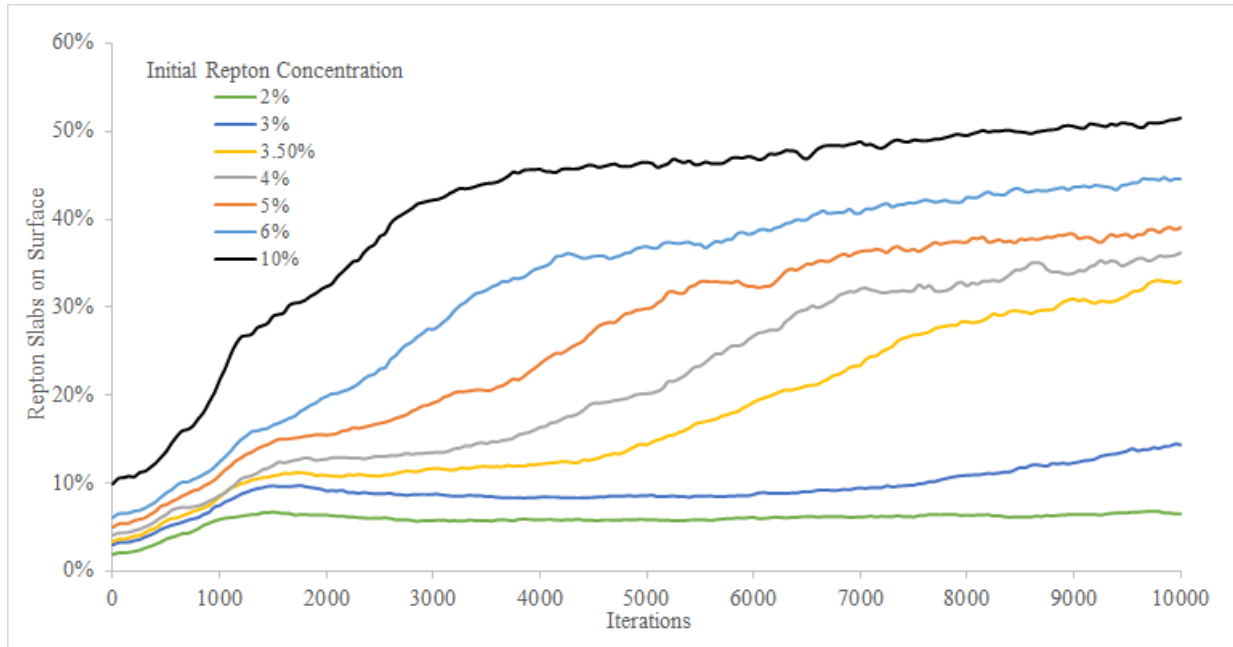


Figure 3.10: Percentage of repton slabs on the surface layer of the MGD model space for 10 000-iteration model runs with varying initial repton concentrations. Megaripple stripes developed with initial concentrations of 3, 3.5, and 4% initial concentrations. At 2%, only impact ripples develop. At 5% or greater, megaripples form rapidly and the megaripple stripe pattern does not emerge. These results show a coarsening over time that is consistent with the findings of Yizhaq et al. (2012a). Interestingly, there is a characteristic shape to the curves which resulted in megaripple stripe formation: a rapid initial increase followed by a brief plateau, followed by a second increase.

3.5.2.3. Effects of Spanwise Transport

To test the effects of spanwise transport, 40 simulations were designed and run. Pairs of simulations were run in increasing increments of 5% $P(\theta)$ from 0 to 1 (i.e., two simulations at 0, 0.05, 0.10, etc.). Five example simulations are shown in Figure 3.12 and a scatterplot of all results is shown in Figure 3.13. The R^2 of 0.20 suggests a weak negative relationship in which increasing spanwise transport leads to megaripple stripes emerging earlier in the model run. However, due to the stochastic nature of the model caused by the influence of several parameters, this effect cannot be established with a high level of confidence without more research and testing with a variety of parametrizations. Further, the dominance of negative residuals for $P(\theta)$ of 0.40–0.65 suggests that the relationship may have non-linear elements. More research is required to isolate these effects. Still, these results suggest that spanwise transport has a

negligible effect on the time (iteration) at which the megaripple stripe pattern emerged in the model. Spanwise transport was likely ineffective and the lifespan of megaripples short because the erosion probabilities in the model do not vary based on location. This issue will be addressed in Chapter 4.

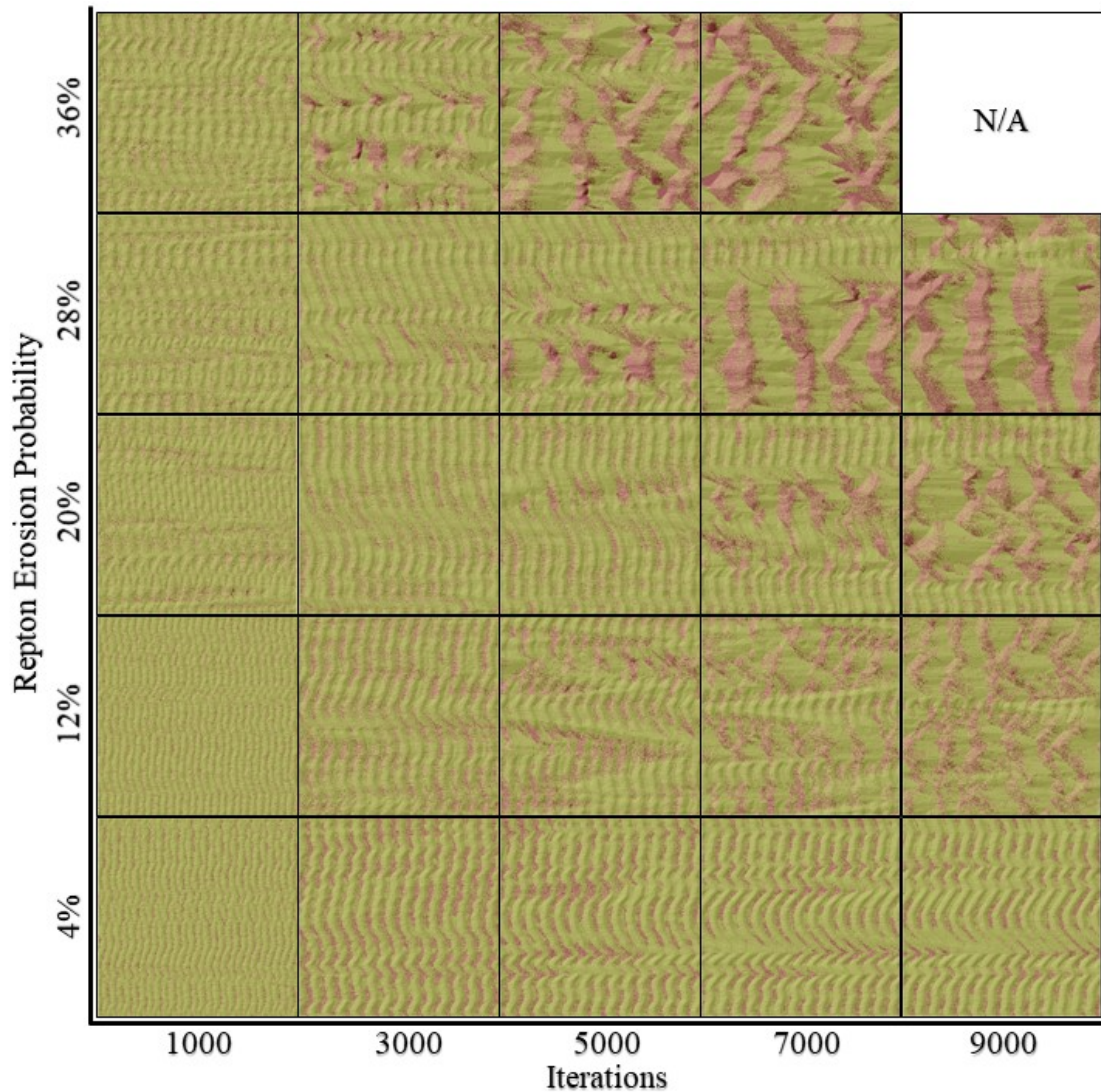


Figure 3.11: Model space visualizations of simulations with 4–36% repton erosion probability after 1000, 3000, 5000, 7000, and 9000 iterations. Megaripples do not develop at 4% and impact ripples migrate over a bed of reptons. Megaripple stripes develop in all other simulations. Larger erosion probabilities increase the rate at which megaripples develop. The simulation for 36% could not be completed because the height of the megaripples exceeded the maximum dimension of the model space after 7150 iterations. All simulations run with identical parameters, except repton erosion probability.

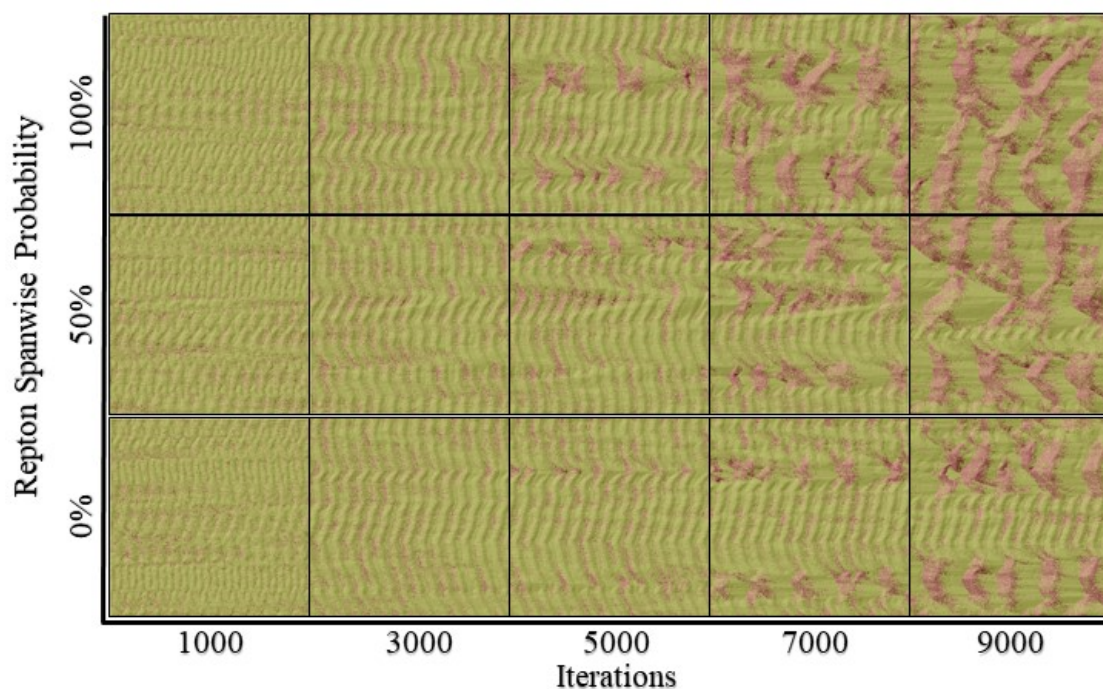


Figure 3.12: Model space visualizations with 0%, 50%, and 100% spanwise transport probability for reptons. Megaripple stripes develop in all simulations. All simulations run with identical parameters, except repton spanwise transport probability (Table 2.1).

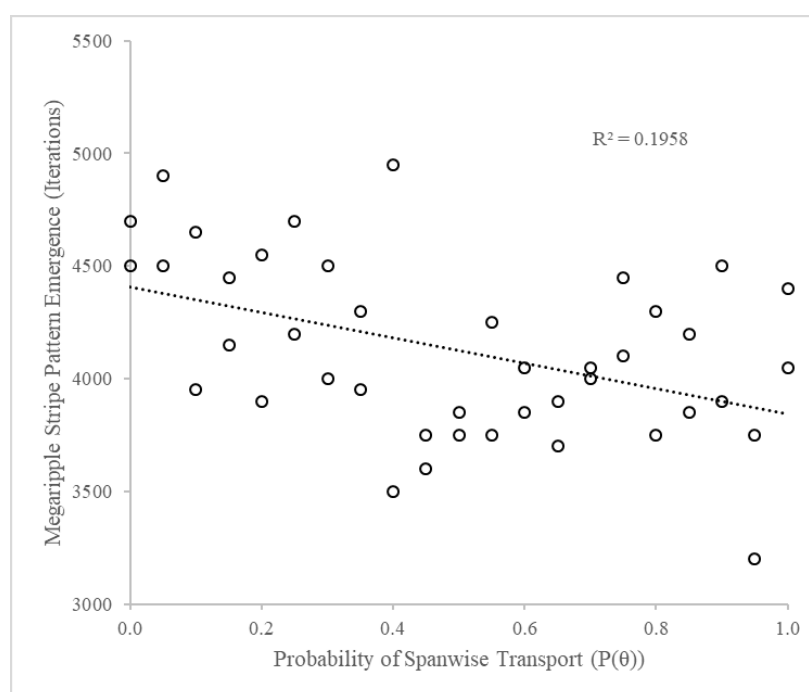


Figure 3.13: Scatterplot of megaripple stripe emergence in the MGD model space against the probability of spanwise transport for repton slabs. A weak negative relationship with R^2 of 0.20 is found.

3.5.3. Summary of Megaripple Stripe Formation in MGD

It was found that there are four distinct stages of megaripple stripe formation in MGD:

1. Impact Ripple Development
2. Nucleation Site Development
3. Megaripple Stripe Expansion
4. Megaripples

Each of these four phases is characterized by the observed pattern on the surface of the model space, the degree of spatial autocorrelation, and the percentage of reptons present on the surface. The following sections are a summary of the progress through a typical model run with parameters shown in Table 2.1.

3.5.3.1. Impact Ripple Development

The initial phase of the model sees the rapid development of small ripple features in the model space after fewer than 1000 iterations (Figure 3.14). These proto-ripples mature and become regularly spaced ripples with largely uninterrupted crestlines after approximately 1500–2000 iterations. This ripple development causes a rapid increase in the percentage of reptons on the surface.

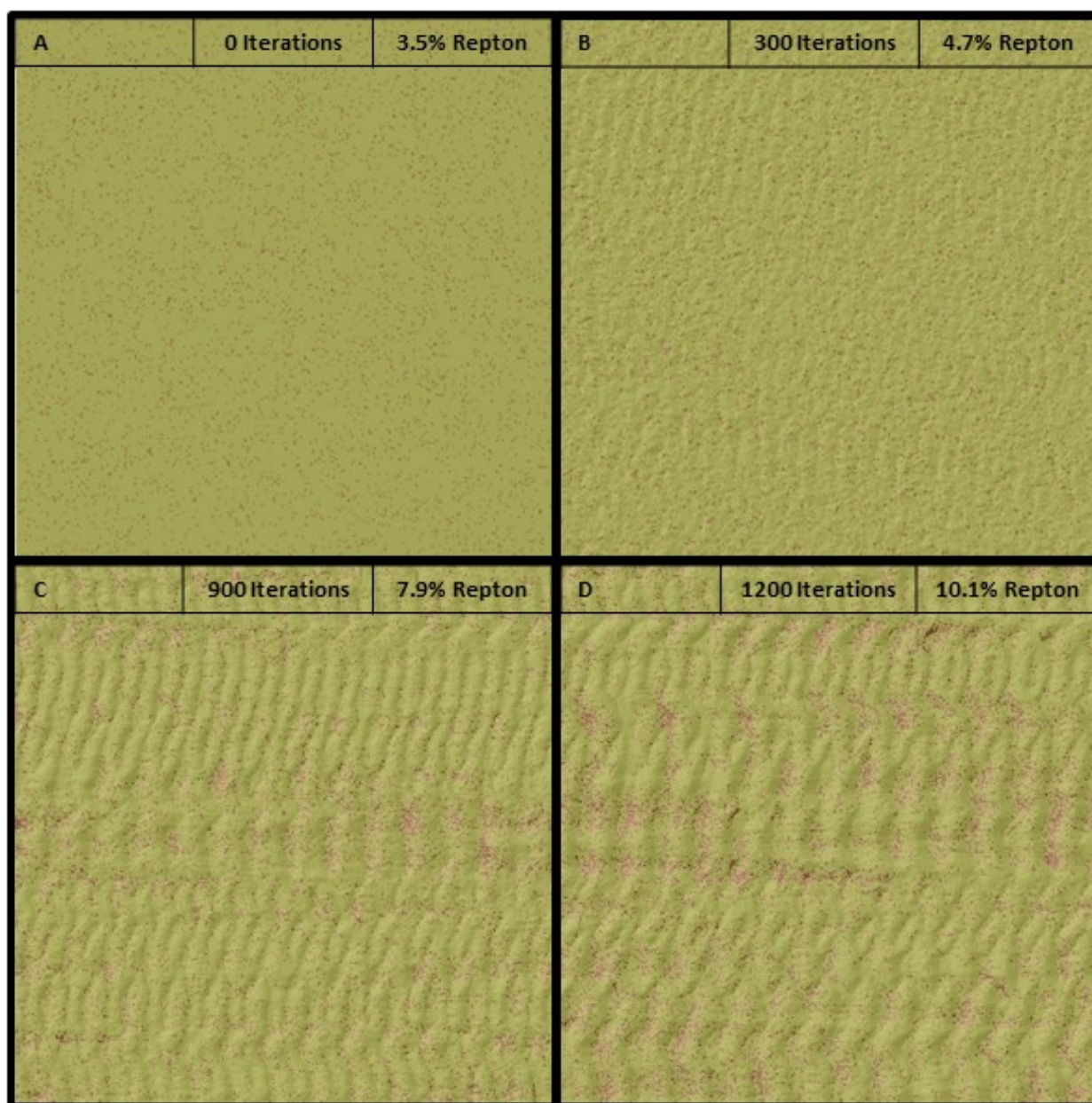


Figure 3.14: Initial impact ripple development in MGD through 1200 iterations. Repton % reflects the concentration of repton slabs on the surface layer of the model space. **A)** The model begins with a random featureless distribution of reptons and saltons. **B)** After 300 iterations, the percentage of reptons on the surface has increased. Small features analogous to proto-ripples begin to emerge at this stage. **C)** Well-defined ripples begin to emerge, and small local concentrations of reptons are apparent. **D)** Ripples continue to develop and increase in wavelength. After only 1200 iterations, repton surface concentration has almost tripled.

3.5.3.2. Nucleation Site Development

Impact ripples continue to develop and migrate in the model space until a large local concentration of repton slabs develops (Figure 3.15). These concentrations serve as ‘nucleation sites’ for megariipple development. Megariipple formation is initiated once a site reaches a downwind size larger than approximately one-half to one-full wavelength of the impact ripples (15–30 slabs). The formation of these sites is associated with a rapid increase in the concentration of reptons on the surface. Because the initial surface concentration of reptons in the model space is relatively low (3.5%), these sites develop slowly at only one or two locations. Megariipple corridors then develop and expand from these nucleation sites. At initial repton concentrations of 5% or greater, nucleation sites develop in multiple locations simultaneously and do not produce stripes (as shown in Figure 3.9).

Little has changed in the model space between iterations 1200 and 3000 (Figures 3.14 and 3.15). The repton concentration has increased by only 1.6% during this time and the features in the model space are still composed of salton slabs, with repton slabs largely confined to the troughs. As will be addressed below, what has increased during these 1800 iterations is the self-organization of the model space (i.e., reptons are closer to other reptons and saltions closer to other saltions after 3000 iterations).

At iteration 3800 a nucleation site has formed that rapidly initiates the development of a megariipple corridor (Figure 3.15C). The observed growth of megariipples is consistent with the findings of Isenberg et al. (2011), where megariipples are found to emerge initially as impact ripples and rapidly develop into megariipples due to coarsening of the surface GSD. This process is further explained by Lämmel et al. (2018), who state that “megariipples co-localize with accumulations of coarse grains and emerge as long-lived transient structures from a unimodal bulk distribution dominated by much finer sand.” (p. 760) Another concentration/nucleation site starts developing in the model space at iteration 4400, from which another corridor of megariipples develops. This leads to the development of a distinct megariipple stripe pattern in the model space.

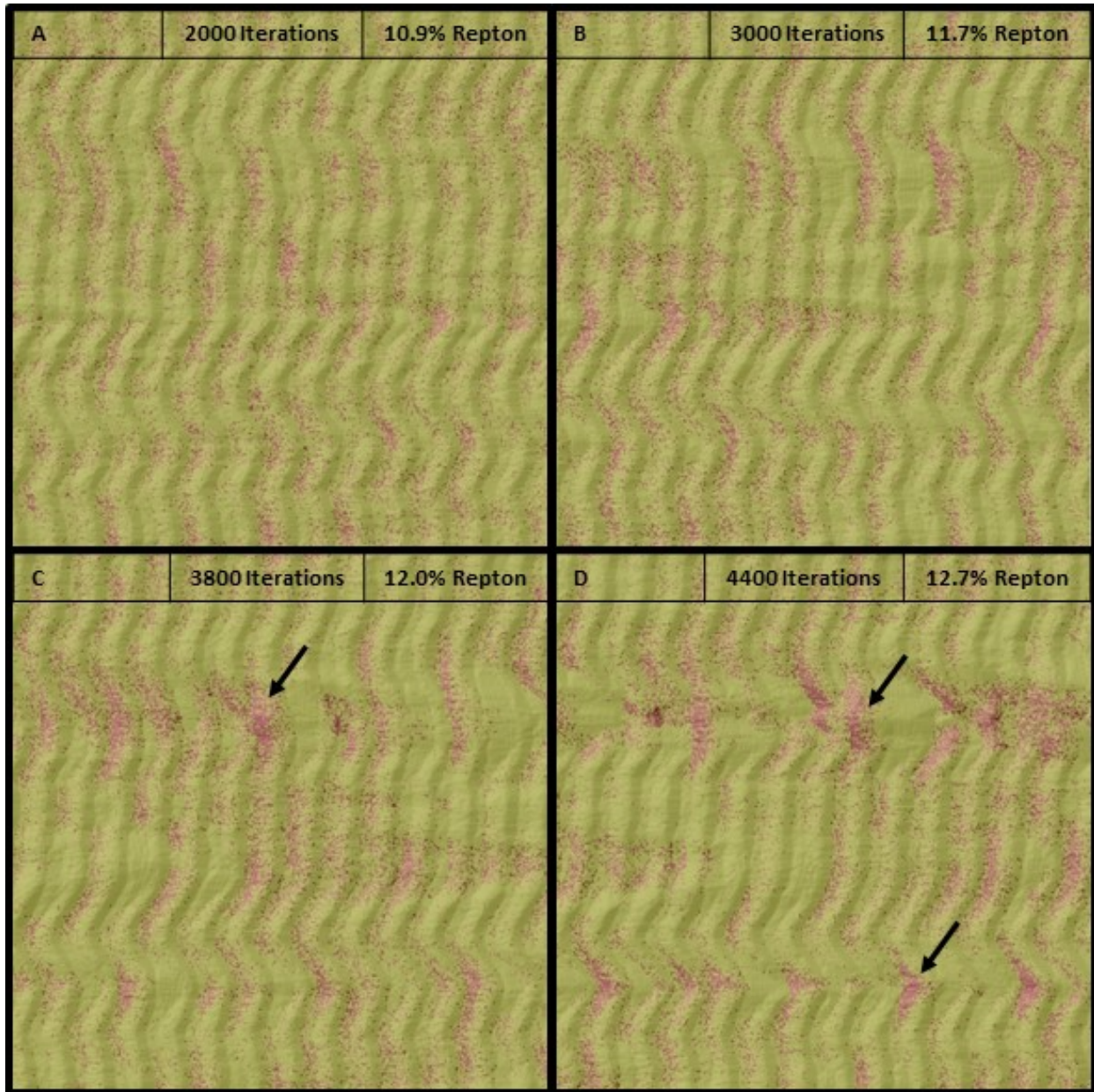


Figure 3.15: Megariipple nucleation site emergence in MGD. **A)** Impact ripples remain the dominant feature of the model space, and repton concentrations have only increased by 0.8% over the past 800 iterations. **B)** Impact ripples continue to migrate in the model space, and repton concentration has increased slightly. **C)** A nucleation site has begun developing in the model space, indicated by the black arrow. The nucleation site has intersected the crestline of the impact ripple. **D)** Two nucleation sites are now present in the model. The topmost nucleation site has expanded and the formation of a megariipple stripe has begun.

3.5.3.3. Megaripple Stripe Expansion

Once nucleation sites have developed, megaripple corridors expand rapidly in downwind and crosswind directions (Figure 3.16). Two megaripple corridors have developed in the model space. This is associated with rapid increase in repton slabs present at the surface after the relative stagnation in repton concentration from iteration 1200 (10.1%) to iteration 4400 (12.7%), for an average rate of 0.08% per 100 iterations. During the formation and expansion of megaripple stripes, repton concentration increased from 14.4% to 26.4% over 2400 iterations, an average rate of 0.50% per 100 iterations—six times the rate observed during the migration of impact ripples earlier in the model run.

3.5.3.4. Megaripples

Stripes cease to exist when crests of the megaripples expand and merge to overtake the corridors of smaller features. The spanwise expansion of the megaripples can be observed throughout Figure 3.16, and the completion of their expansion until only megaripples remain can be seen in Figure 3.17. The percentage of reptons on the surface increased throughout the simulation and reached 32.9%, a nearly tenfold increase from the initial surface concentration. This increase in the surface concentration of large grains associated with megaripple development was observed by Yizhaq et al. (2012a), who recorded an increase in surface concentration of coarse grains from 2.7% to 39.6% over an 11-month period at Nahal Kasuy, Israel. All simulations that led to the formation of megaripple stripes saw the expansion of megaripples until they filled the model space. The length of this phase represents the lifespan of megaripple stripes in the model. Because of the expansion of megaripple corridors, megaripple stripes represented a transitional form in MGD that typically lasted for 1000–5000 iterations.

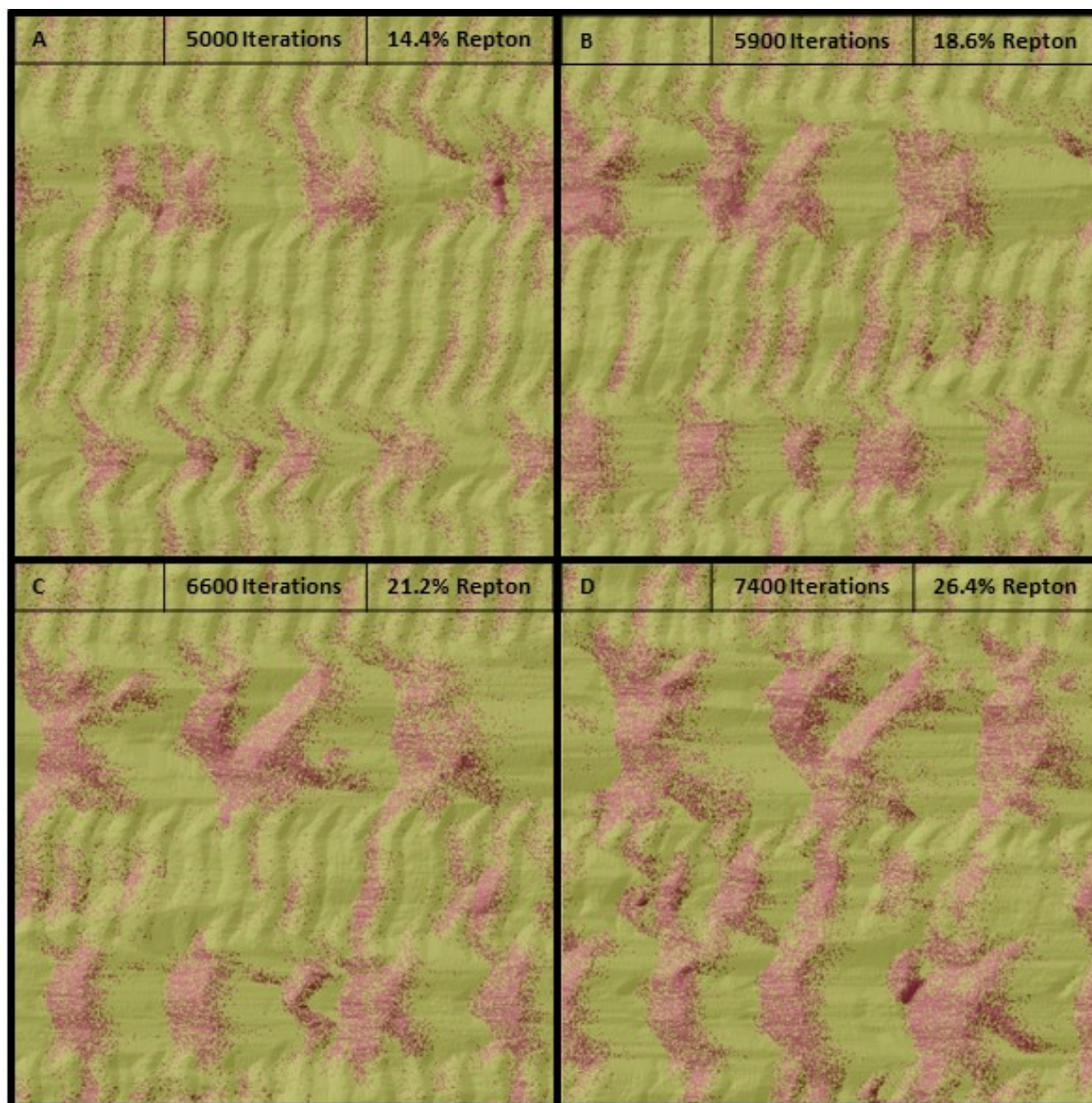


Figure 3.16: Megaripple stripe development and expansion in MGD. **A)** Megaripple stripe development continues from Figure 3.15D, and the surface repton concentration continues to increase. **B)** The megaripple stripe pattern is well developed at this stage, and distinct megaripple-type features have emerged in the model space and have started expanding crosswind. **C)** The crosswind expansion of megaripple stripes continues. **D)** The megaripple features have expanded and nearly overtaken all the smaller ripple features, nearly bringing an end to the megaripple stripe pattern in the model space. The surface repton concentration after 7400 iterations is 7.5 times greater than the initial value.

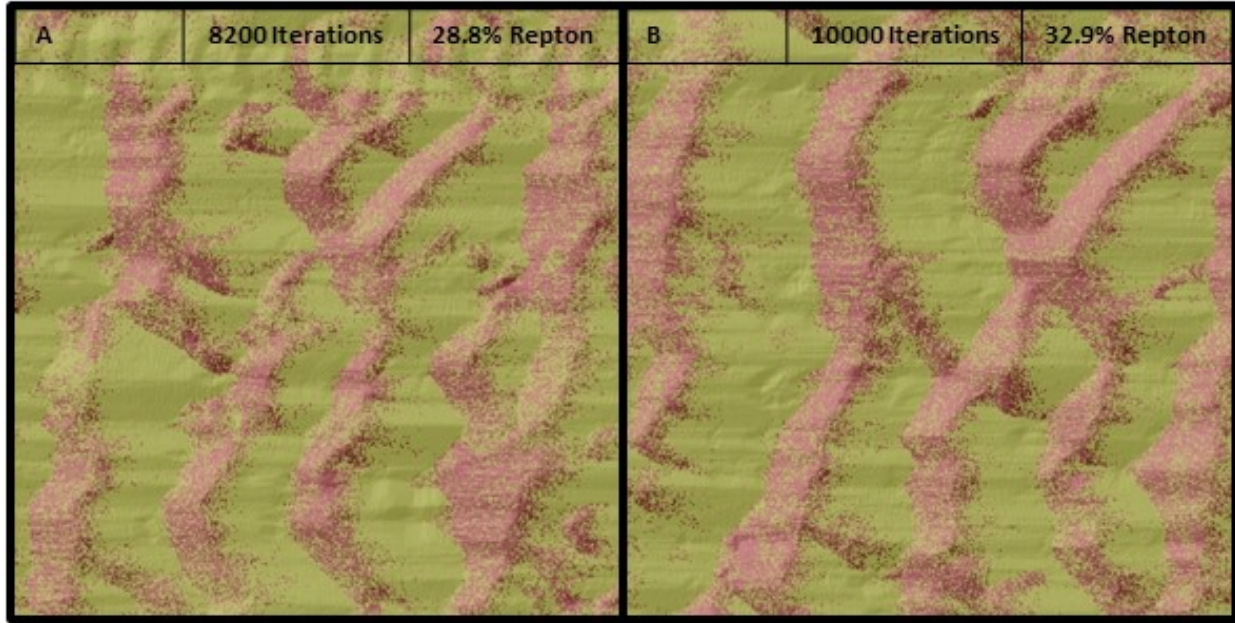


Figure 3.17: Final stages of megaripple stripe simulations in MGD. **A)** The corridor pattern is no longer extant and almost the entire model space is filled with megaripples. **B)** After a 10 000-iteration model run beginning with a featureless model space and only 3.5% reptons on the surface, large megaripples have developed and repton slabs cover a third of the surface layer.

3.5.4. Spatial Autocorrelation and Megaripple Stripe Development

Megaripple stripes and their development are closely related to the spatial organization of reptons and saltions in the model space. The spatial organization of the entire model space was tracked using a global Moran's I statistic. Moran's I ranges from -1 to 1, where -1 represents perfect dispersion of reptons and saltions, 0 represents a random distribution, and 1 represents complete segregation of slab types. No negative values were observed during the simulations. The logged Moran's I statistic and the associated change in the percentage of reptons on the surface for three typical megaripple stripe simulations are shown in Figure 3.18. A local spatial autocorrelation statistic, the Getis-Ord G_i^* , was also tracked at 50 iteration intervals. Model space visualizations for slab type and G_i^* for a 10 000-iteration simulation are shown in Figure 3.19. Together, these two figures show how megaripple stripes emerge from increasing overall and local concentrations of reptons in the model.

As MGD begins with a random distribution of reptons and saltons, the Moran's I for all simulations begins at a value very close to 0. The simulations shown in Figures 3.18 and 3.19 had a bulk repton concentration of 3.5%. There is initially a rapid rise in both Moran's I and the number of reptons in the model space. This is followed by a period of relative stability in the model space where spatial autocorrelation increases slowly as ripples mature, and repton concentration remains relatively constant. The signal of megariipple formation is a rapid increase in repton concentration after a period of stagnation and an accompanying increase in both local and global spatial autocorrelation. It is clear in Figure 3.19 that megariipple stripes develop from local concentrations of reptons. Megariipple stripes then continue to grow and spatial autocorrelation continues to increase until megariipples occupy the entire model space and the striped pattern is no longer present.

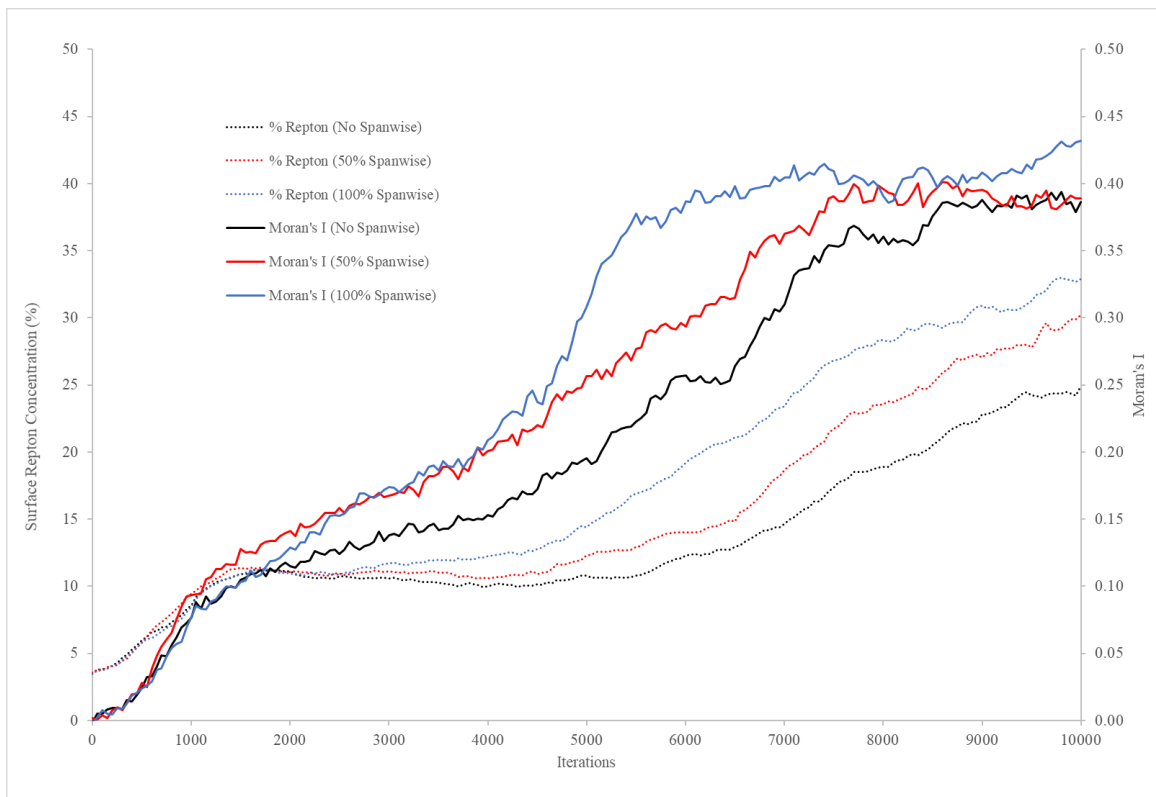


Figure 3.18: Logs of the percentage of repton slabs present at the surface and the Moran's I of the surface layer for three MGD simulations. The simulations shown were run with identical parameters (Table 2.1), with the exception of repton spanwise transport. The spanwise transport probabilities used were no spanwise transport (black), 50% spanwise transport (red), and 100% spanwise transport (blue).

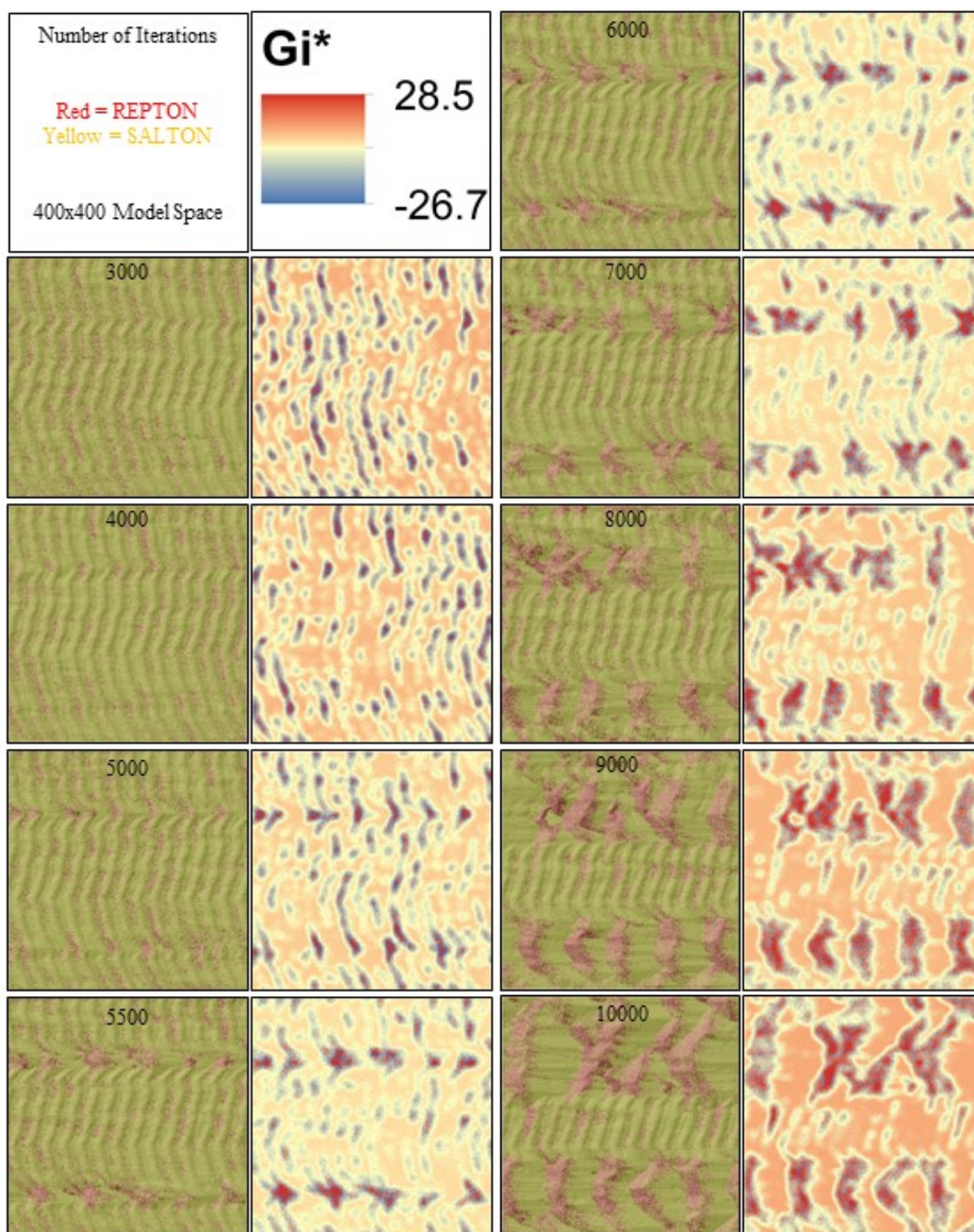


Figure 3.19: Model space visualizations of slab type and Gi^* for a 10 000-iteration simulation with a bulk concentration of 3.5% reptons. Megaripple stripes emerge when a local concentration of reptons develops. The Gi^* is interpreted as a Z-score, where a value of ± 1 indicates a single standard deviation above/below the mean. The scale shown is representative for all outputs.

3.5.5. Morphometric Comparison of MGD and Oceano

A DSM from a simulation of megaripple stripes in MGD is shown in Figure 3.20. A sample transect measurement is shown in Figure 3.21. A comparison of Figures 3.20 and 3.21 to Figures 3.7 and 3.8 shows a strong resemblance between simulated megaripple stripes and those found at the Oceano Dunes. Measurements of ripple heights and wavelengths from the Oceano Dunes are compared with the outputs from the numerical modelling in Table 3.5. However, as units differ between these two measurements, the relative ratios of height and wavelength between megaripple and smaller bedform heights and wavelengths are shown in Table 3.6. These ratios and coefficients of variation suggest the model has reproduced features similar to megaripple stripes.

The most significant difference between the megaripple stripes produced in MGD and those observed at the Oceano Dunes is the ripple index of the features; the modelled features have unrealistically low ripple indices. This, as will be addressed below, is likely because there is no simulation of flow acceleration at the top of features to limit bedform heights (Siminovich et al. 2019). This led to bedforms being taller than expected relative to their wavelengths. Nevertheless, the ratios of heights and wavelengths of the modelled bedforms are similar to those observed at Oceano (Table 3.6) and the reproduction of two corridor types with different characteristic bedform sizes is obvious. The large variability in heights and wavelengths of natural megaripples was well reproduced in the model, whose coefficients of variation closely match those of the Oceano megaripples. The modelled smaller bedforms were more deterministic in size and did not reproduce the same level of morphometric variability observed in the smaller bedforms at Oceano.

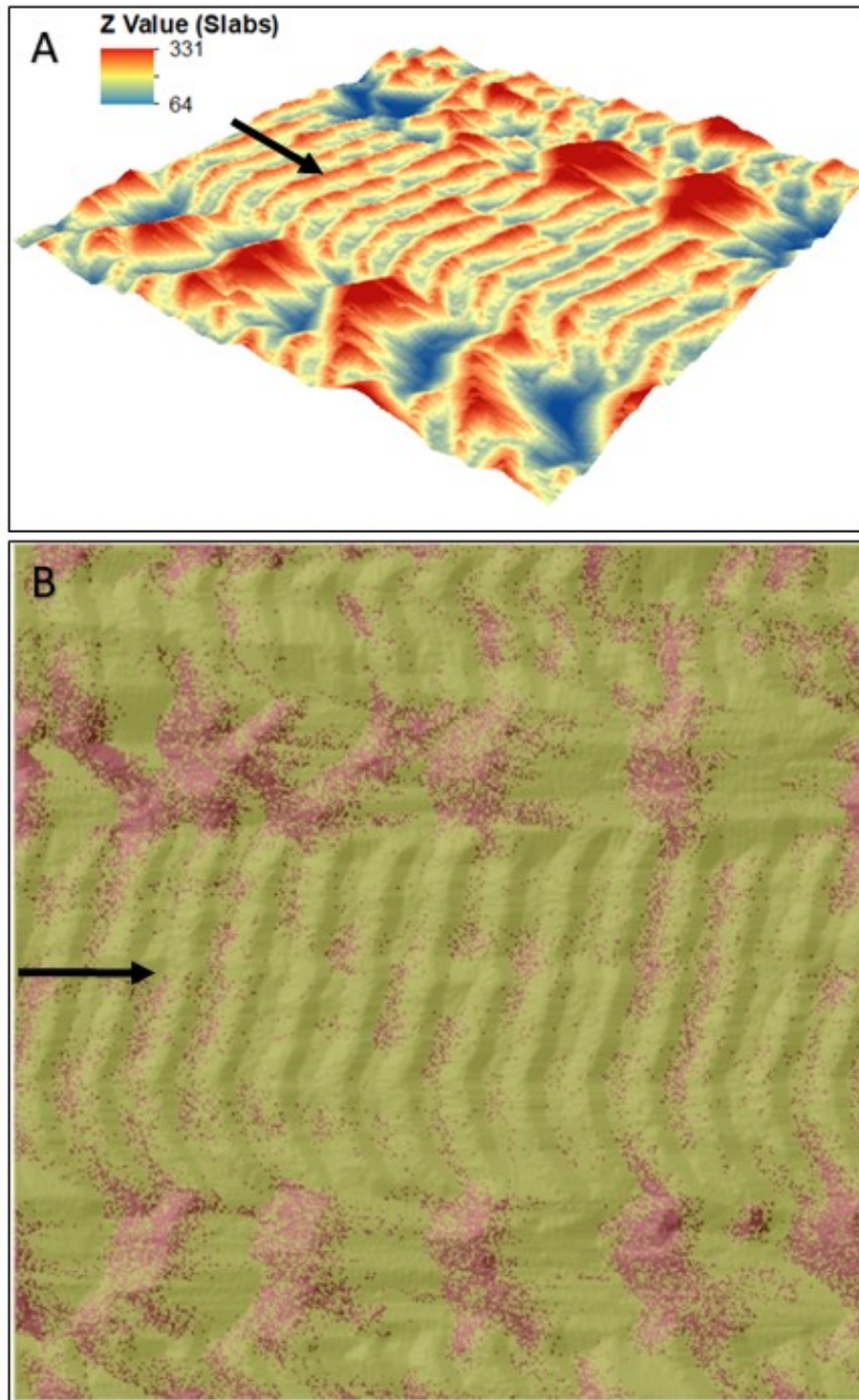


Figure 3.20: *A)* DSM of a megaripple stripe simulation after approximately 1.2 billion individual slab transport events (7500 iterations). *B)* Planview of the surface for the DSM shown in A). As with the megaripple stripes observed in Oceano and Argentina, the lowest point in the simulated megaripple stripes is also the trough of the megaripples. Arrows indicate transport direction. Compare to Figure 3.7.

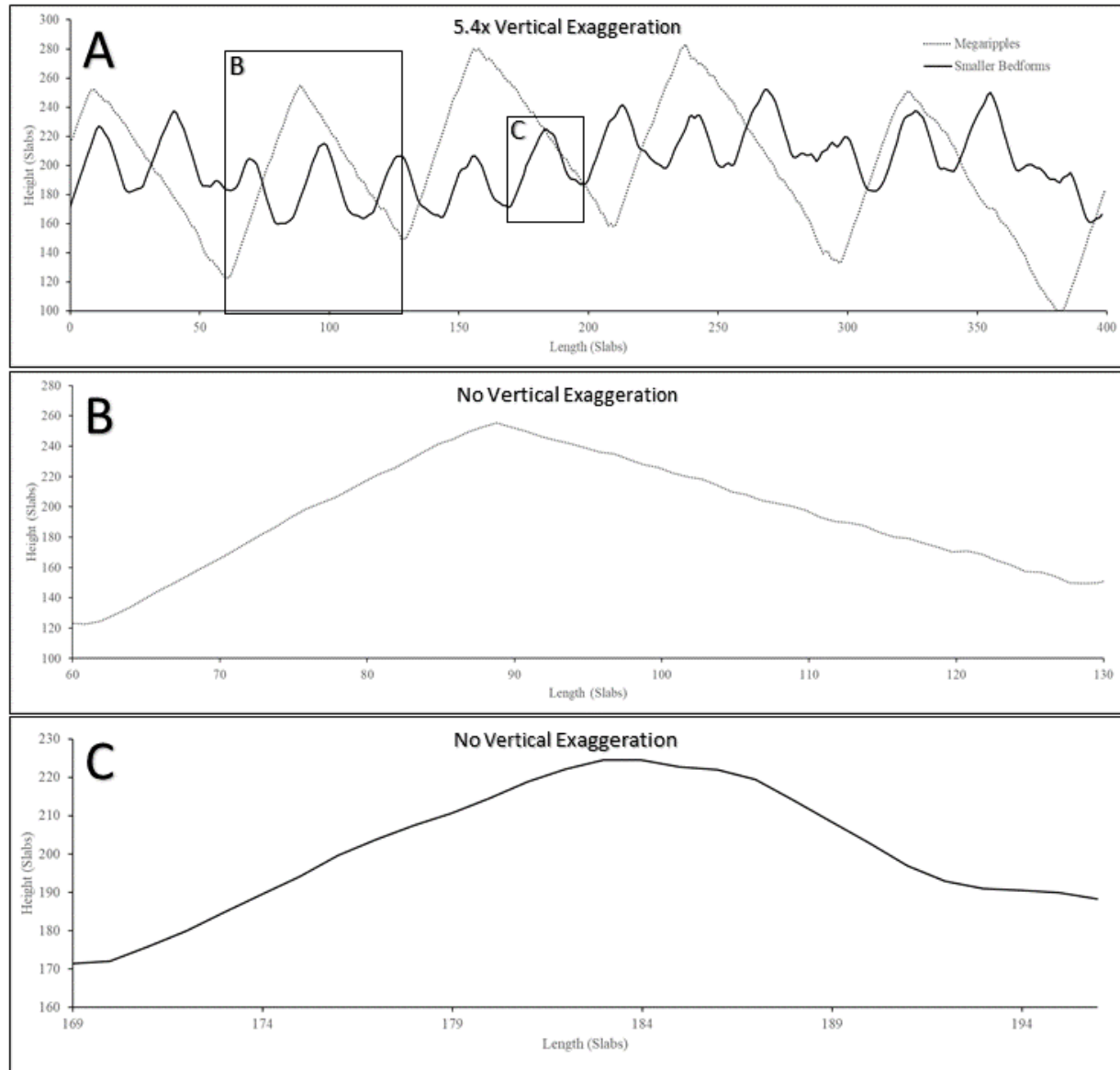


Figure 3.21: *A)* Transect measurements of smaller bedform and megaripple corridors in MGD showing distinct differences in height and wavelength between corridor types. Note that the z dimension of slabs is one-tenth that of the x dimension. *B)* Inset of megaripple profile. The stoss and lee slope have lengths of approximately 30 and 40 slabs, respectively. *C)* Inset of smaller bedform profile. The convex curvature of the ripple is similar to that observed at the Oceano Dunes. Compare to Figure 3.8 above.

Table 3.5: Morphometrics acquired from photogrammetry of the Oceano Dunes megaripple stripes and the MGD model outputs. *The wavelength measurements for Oceano reported here do not match those reported above because these measurements were acquired from different samples and by a different methodology.

		SMALLER BEDFORMS		MEGARIPPLES	
		Oceano (cm)	Model (Slabs)	Oceano (cm)	Model (Slabs)
Wavelength	Mean	10.65	28.69	20.40*	87.07
	Standard Deviation	3.20	1.55	8.36	27.19
	Coefficient of Variation	0.30	0.05	0.41	0.31
Height	Mean	0.39	4.54	1.40	13.90
	Standard Deviation	0.84	0.50	0.62	6.08
	Coefficient of Variation	0.28	0.11	0.44	0.44

Table 3.6: Relative metrics of wavelength and height for the Oceano Dunes and the MGD model.

	Oceano	MGD
Megaripple/Smaller Ripple Wavelength Ratio	1.92	3.03
Megaripple/Smaller Ripple Height Ratio	3.58	3.06
Ripple Index (Megaripple, Smaller Bedform)	14.54, 27.23	6.26, 6.39

3.6. Summary of Results

The results presented indicate that megaripple stripes are a crosswind pattern composed of two alternating corridor types: one consisting primarily of megaripples and relatively coarser grains, and another consisting of impact ripples and smaller megaripples with relatively finer grains. There appears to be a positive relation between the downwind wavelengths of the megaripple corridors and the crosswind wavelength, whereby the latter is 2–3 times larger than the former. Grain size data from California and Argentina confirm that the smaller bedform corridors have smaller grains than the megaripple corridors.

This largely confirms the first hypothesis of a distinction in grain size between corridor types being a primary characteristic of megaripple stripes.

Megaripple stripes were reproduced using a cellular automata model and a two-species approach. Reptons were given small transport lengths and low erosion probabilities to simulate the properties of larger grains that resist direct fluid transport. Saltons were given large transport lengths and high erosion probabilities to simulate the properties of smaller grains below the fluid threshold. Importantly, this binary reduced-complexity approach shows that megaripple stripes could be reproduced without the need for incorporating airflow or more complex mechanisms. The two key elements were a limited supply of repton slabs (2.4–4.7%) and low repton erosion probabilities (12–30%). These findings provide support for the second hypothesis outlined in Chapter 1. These parametrizations allowed for megaripple nucleation sites to develop slowly and in only one or two locations in the model space. Megaripple corridors then expanded from these nucleation sites to create the striped pattern. Megaripple stripes produced in MGD show a strong morphometric resemblance to megaripple stripes observed at the Oceano Dunes. The development of megaripple stripes is found to emerge from concentrations of reptons, which were quantified locally and globally in the model space using spatial autocorrelation metrics. Modelled megaripple stripes are a transitional pattern that emerge when initially low concentrations of reptons lead to the formation of nucleation sites from which corridors of megaripples develop. However, it is unclear if megaripple stripes observed in the field and in imagery have the same life cycle and behaviours as these modelled features. Spanwise transport was not necessary for megaripple stripe development but may be essential for maintaining the pattern because megaripple stripes were only a short-lived feature in the model. This will be discussed in the following chapter.

Chapter 4: Discussion

4.1. Overview

Megaripple stripes are a crosswind pattern of alternating corridors of smaller bedforms and megaripples. The corridor types can be distinguished by their distinct scales of bedforms and grain size. This was confirmed with field measurements and satellite imagery. These results were further supported by outputs from a numerical model, MGD. The coarse grains present on the crests of the megaripple corridors are assumed to be largely reliant on reptation for transport and are accordingly termed reptons (Bagnold 1941, Andreotti 2004, Yizhaq et al. 2012a). Conversely, the finer grains present are assumed to be predominantly transported by saltation and are termed saltons. This simplified binary approach was sufficient to reproduce megaripple stripes in MGD. Further, it is known that these smaller grains must be transported predominantly by saltation because if these grains were reliant on reptation, they would also develop into larger megaripple features (Bagnold 1941). Of course, due to the stochastic nature of grain transport and bedform migration, some bedforms with morphometric properties intermediate to impact ripples and megaripples are present in both corridor types. The presence of bedforms in megaripple stripes with wavelengths ranging from a decimetre to ten metres reflects the fluid nature of bedform development and migration. The migration of bedforms of differential height and celerity leads to collisions between bedforms (Yizhaq et al. 2012b). Although the modelling provided some insight into megaripple stripe behaviour and the mechanisms that cause the pattern to emerge, there remains uncertainty about how these mechanisms operate in natural conditions.

4.2. Megaripple Stripes – Corridor Types

The bedforms of the megaripple corridors have morphometrics and characteristics typical of megaripples. Although definitions vary, megaripples are understood as having the following characteristics:

1. Wavelengths generally larger than 30cm (Yizhaq et al. 2015; Lämmel et al. 2018)

2. A bimodal or poorly sorted GSD (Jerolmack et al. 2006; Yizhaq et al. 2015)
3. Nearly symmetric downwind cross-sections (Zimbelman et al. 2012) and sinuous crestlines (Yizhaq et al. 2015)
4. Formation timescales on the order of days to years (Yizhaq et al. 2015; Lämmel et al. 2018)

It is known from results presented above that the features in the megaripple corridors conform to the first three of these. The formation timeline of megaripple stripes, and with megaripples in general, remains unclear. Results from MGD showed that megaripples emerge from nucleation sites of reptons, but no field evidence for this was found. Regardless of formation timeline, the features in the megaripple corridors are interpreted here as megaripples because they clearly fit these characteristics and are not regular impact ripples. Megaripples are dependent on the presence of reptating grains for their formation and growth (Bagnold 1941). The features in the smaller bedform corridors of megaripple stripes are interpreted as impact ripples, driven primarily by saltation. However, several bedforms in both corridor types have intermediate properties and cannot be tidily classified as either impact ripple or megaripple.

None of the bedforms present in megaripple stripes are particularly remarkable when considered in isolation. Instead, megaripple stripes are notable because of their pattern and spatial distribution of different bedform sizes. Although the presence of two distinct wavelengths of ripple-scale bedforms is not novel in aeolian features, their organization into crosswind corridors is. The same surface GSDs are not present in both corridor types, suggesting that there are insufficient grains reliant on reptation to develop an armour layer leading to megaripple development throughout the bedform field. It is highly unlikely that this cross-wind stratification was pre-existent in the deposits. Therefore, some aeolian transport mechanism must be causing this pattern to develop. A numerical model was used to elucidate what this mechanism might be and to show that a limited repton supply leads to megaripple stripe development.

4.3. Modelling of Megaripple Stripes

An outcome of this research is that direct modelling of small variations in fluid and grain behaviour is not necessary to reproduce megaripple stripes in a model; two generalized behaviours, saltation and reptation, are enough. These findings are consistent with other two-species approaches (e.g., Andreotti 2004; Lämmel et al. 2012). The repton and salton species were modelled as having downwind trajectories of 3 and 30 cells, respectively. It was found that megaripple stripe formation was controlled primarily by having a small proportion of reptons in the model space and an erosion probability for reptons that was approximately 12–30% that of the saltons. In other terms, the effective flux on a per slab basis for saltons was typically forty times greater than that of reptons. These parameters produced a pattern of features very similar to natural megaripple stripes. A strong crosswind sorting of grains, large megaripples with an armoured stoss slope, and similar wavelength ratios for megaripple and smaller bedform corridors were all reproduced by the model. The modelling results show that megaripples stripes in MGD develop from a nucleation site of reptons on the surface that initiates megaripple formation and propagates downwind. These nucleation sites are associated with both an increasing global organization of slabs in the model space as well as high local concentrations of reptons. Because the repton slabs are limited, only a few of these sites develop. This allows for the development and downwind extension of corridors of megaripples to occur rather than rapid megaripple growth throughout the entire model space. The smaller bedform corridors are simply the areas of remaining smaller bedforms in the crosswind gaps between megaripple corridors. The megaripple stripe pattern ceases to exist when these gaps are overtaken by the expanding megaripple corridors. Due to the long timescales involved it is unclear whether these parameters can be directly related to the mechanism and conditions that lead to natural megaripple stripe formation.

Ripple heights are controlled by the nature of saltation and reptation. Impact ripples have little variability in their height because all the surface grains have high probabilities of transport. The portion of an impact ripple that is higher than another will see its grains removed more quickly than the lower

portion, assuming the same grain properties at the two locations, because the higher grains are subject to larger shear velocities (Yizhaq et al. 2012b). This is not necessarily the case in megaripples because the armour layer is resistant to direct fluid entrainment under most conditions. Megaripples are theoretically capable of growing to infinitely large sizes if there is a supply of reptons to form an armour layer, saltons available to initiate the transport of these reptons, and a wind less than the transport threshold of the reptons (Bagnold 1941; Siminovich et al. 2019). These conditions were summarized in Equation 5. If the wind is incapable of removing the armouring reptons, then they will continue to accumulate on the stoss slope and the megaripple will grow. In nature, megaripple growth is limited by flattening due to strong winds that drive reptons into saltation, and from deflation by impacts of faster saltating grains (Katra et al. 2014). However, these limiting factors do not affect megaripple growth in MGD because there is no explicit simulation of flow and the transport behaviours of saltons and reptons are not directly linked. This allows megaripples in MGD to grow to unrealistically large sizes if the model is run indefinitely or reptons are given a high erosion probability.

Despite the success of the simulations, several aspects of megaripple stripes remain unclear. First, it was shown that the crosswind wavelength of megaripple stripes scales with their downwind wavelength, and it is known that the downwind wavelength of megaripples is largely determined by grain size (Yizhaq and Katra 2015). It is therefore likely that crosswind wavelength is also a function of grain size, but what physical mechanism governs this scaling remains unclear. Second, spanwise segregation was reproduced in the modelling runs, but megaripple stripes were relatively short-lived in MGD. This is likely due to the lack of a location-based erosion probability in MGD, discussed below, which does not reproduce bedform-constrained saltation and reptation behaviour observed in natural aeolian sediment transport. It is difficult to assess what the lifespan of natural megaripple stripes may be and to compare the computational development timeline (iterations) to the actual passage of time. Finally, there is limited field evidence for the ‘nucleation site’ hypothesis provided here. It is posited that megaripple stripes begin upwind and gradually migrate downwind as reptons are transported. In all cases, megaripple stripes are

dependent on the presence of reptons in supply-limited quantities. Of course, megaripple stripe formation and migration are also affected by sorting mechanisms in all three dimensions. Some of these were effectively replicated in MGD and others were not. These sorting mechanisms are complex and occur on multiple scales.

4.4. Repton Sources for Megaripple Stripes

Interdune trough deposits are the likely source of reptons for the megaripple stripes observed in Oceano, China, Namibia, and Mars. Coarser grains are known to accumulate in interdune troughs (Bagnold 1941). This allows for the development of megaripples to be initiated at the base of the stoss slopes of dunes (Figure 4.1). Megaripple formation is initiated in dune troughs and corridors of megaripples slowly climb the stoss slopes of dunes. As the source of reptons is the trough of the dune, megaripple formation would be dependent on the slow transport of reptons up the dune slope. This explains the thinning of megaripple corridors as they climb the dune slopes. In some cases where repton supply is limited even in these trough deposits, megaripple stripes develop immediately. In others, full megaripples form and then develop into stripes as they migrate upslope and repton supply becomes increasingly limited. Further, the rate of this climb and the development of megaripple stripes are limited by the migration rates of the dunes. A dune superimposed with megaripples on it must be migrating more slowly than a dune with simple impact ripples because reptation is a much slower transport process than saltation. Further, because dune formation and scaling are thought to be dependent on the spatial lag between the maximum shear velocity and the maximum flux of grains (the ‘saturation length’), a distance governed by saltation, it is not expected that extensive megaripples can coexist with large active dunes (Andreotti et al. 2010). This length-scale distinction led Lämmel et al. (2018) to suggest that megaripples may be better understood as ‘reptation dunes’ rather than ripples because the wavelengths of megaripples reflect the saturation length of reptation. Because megaripple stripes form in environments with a portion of the GSD that is dependent on reptation, it is unclear how well they may coexist with active dunes because dune migration is reliant on the majority of grains being capable of saltation (Table 4.1).

Megaripple stripes on dunes are an interesting example of decimetre-scale impact ripples, metre-scale megaripples, and decametre-to-kilometre-scale dunes all present together, a coincidence of three bedform wavelengths thought to be uncommon on Earth (Lapotre et al. 2016).

There are three terrestrial locations where megaripple stripes are present alongside sparsely vegetated and stable dunes (Oceano, Namibia, China). Slow dune migration is likely a requirement for the existence of megaripple stripes because the rate of megaripple growth must be faster than the migration rate of the dunes. Some likely candidate sites for finding more megaripple stripes are therefore the upwind sources and trough deposits of vegetated barchan dune fields (e.g., Namibia, China) or downwind of a foredune complex (e.g., Oceano). The sources of repts for the megaripple stripes at the other locations (Argentina, Iran, Peru, Mars) are uncertain. At each of these sites, there is the possibility of repts being exhumed in situ throughout the field of megaripple stripes or transported long distances from upwind deposits. In the case of Argentina, there is likely a combination of source materials because of the complex geology of the region and its strong winds (Báez et al. 2015; Bridges et al. 2015). Due to the erosional environment of the yardangs in Iran, the source of grains is likely a combination of upwind sources and clasts exhumed by abrasion. Gay Jr. (2005) suggested that the sand in the Ica Desert of Peru is sourced from coastal deposits, but it is unclear whether this is the case for both the fine sands and coarser grains present on megaripples in the region. The megaripple stripes in Rabe Crater are composed of ‘dark sediment’, which is thought to be sourced locally from within the crater (Fenton 2006; Tirsch et al. 2011).

Table 4.1: Generalized bedform formation table based on the type of aeolian transport occurring. Megaripple stripes are hypothesized to occur only when the transport environment is conducive to megaripple development, but reptons are in limited supply.

		Bedforms	
		Ripple-Scale	Dune-Scale
Transport Types	Saltation-Dominant	Impact Ripples	Dunes
	No Transport (Below Threshold Winds)	None	None
	Reptation-Dominant	Megaripples	Dunes?
	Frequent Saltation and Infrequent Reptation (Supply-Limited Reptons)	Megaripple Stripes (Megaripples and Impact Ripples)	Dunes?

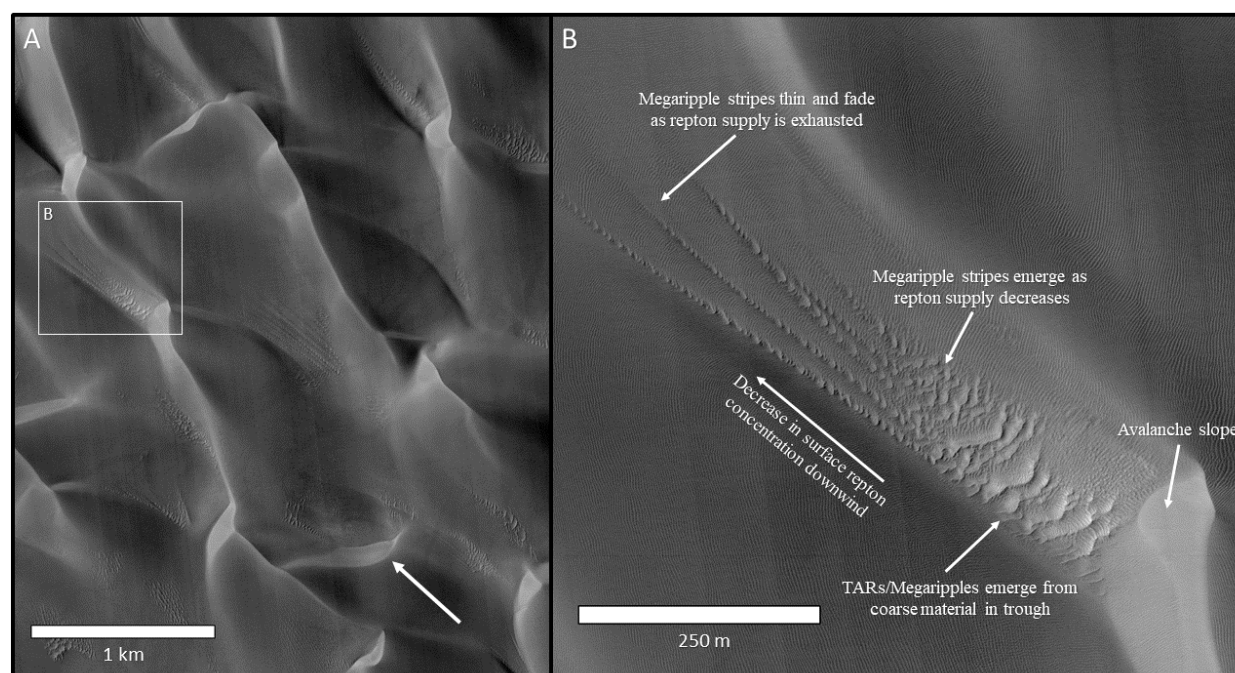


Figure 4.1: **A)** Barchanoid dunes and megaripple stripes in Rabe Crater. The megaripple stripes and megaripples have emerged in several locations directly downwind of avalanche slopes and/or from dune troughs. The megaripples extend for some distance and then fade. The dune troughs are likely sources of reptons, which rapidly decrease in availability as the megaripples climb the stoss slopes of dunes. Arrow denotes assumed dominant direction of transport. **B)** Inset image with hypothesized downwind decrease in reptons and thinning of the megaripple stripe pattern. These same processes can be seen occurring in the imagery of China (Figure 1.7) and Namibia (Figure 1.8).

4.5. Sorting Mechanisms

Sorting occurs on small and large spatial scales. Perhaps the most important sorting mechanism for megaripple formation is the different trajectory lengths of saltating and reptating grains (Anderson 1987). This sorting process occurs at smaller scales and is associated with the formation of armour layers on megaripples and inverse graded lamination if ripple migration continues for an extended period (Anderson and Bunas 1993; Makse 2000). This sorting was reproduced in MGD using two different transport lengths for salton and repton slabs. The 10:1 transport length ratio used for saltons and reptons in MGD produced bedforms with similar relative scaling to natural megaripples and impact ripples.

On a larger scale, observed only in satellite imagery and not in MGD, there is a downwind sorting of grains that appears to be occurring at several of the observed megaripple stripes. This is most apparent at Abra Pomez, Argentina (Figure 1.3). This ‘aeolian sieving’ process is well understood and is known to create a downwind fining and sorting effect over relatively large distances (Durán et al. 2011). Although this natural sieving occurs over several kilometres in the case of dune sands, it may occur over much shorter distances in the case of grains reliant on reptation. Evidence for downwind fining was found in the photosieving results from Abra Pomez. This is because reptons are transported infrequently, have short transport lengths, and require impacts from other grains of sufficient size to be transported. The downwind thinning of megaripple corridors is associated with the downwind fining of grains because the availability of reptons for megaripple development likely decreases downwind. At Namibia, Oceano, and China, megaripple stripes in dune fields thin over small distances as they climb the stoss slope. In these cases, there is both an aeolian and effective gravitational sieving caused by the difficulty of transporting reptons upslope.

On a smaller scale, reptons climbing the stoss slope of megaripples become increasingly isolated from transport. Saltation is expected to be more frequent in the smaller bedform corridors than in the megaripple corridors simply because there are more grains susceptible to saltation in the former. As reptation is dependent upon impact from saltons, it is also expected that the frequency with which a

repton is transported will be higher in the smaller bedform corridors. If this is the case, then there are differential erosion probabilities for reptons in each corridor type. A repton on the crest of a megaripple is isolated from impacts by saltons and has a lower probability of transport relative to reptons in the adjacent smaller bedform corridors. A repton in this crest position is far more stable than one in a field of impact ripples, where it would be subject to a higher rate of salton bombardment and transport (except for its increased susceptibility to direct fluid entrainment). It follows that in an environment where reptons are in limited supply they will continue to be transported from an unstable environment with frequent transport (smaller bedform corridors) until they are relatively stable on the crest of a megaripple in an adjacent megaripple corridor. In megaripple stripes it is then clear why allowing for a spanwise component of transport is essential, as spanwise transport would provide the mechanism necessary for the exchange of grains between corridor types. It is posited that reptons in the smaller bedform corridors will continue to be transported downwind until, by means of spanwise transport, they have been transported onto the crest of a megaripple.

The exhumation of grains under erosive conditions is an essential mechanism for megaripple development (Lämmel et al. 2018). In conjunction with the downwind thinning of megaripple corridors and fining of grains, the availability of reptons from the subsurface or ‘bulk distribution’ in an area affects megaripple stripe formation. It is expected that reptons present on the surface will increase over time because of the transport of finer material downwind, ripple formation, and the exhumation of reptons from the bulk subsurface distribution. However, there are several important considerations in evaluating how megaripple stripes migrate and how reptons come to the surface in a given area: they are either transported from upwind, are already present on the local surface, or are exhumed locally under erosive conditions (Lämmel et al. 2018). For megaripple stripes to expand downwind, at least one of these processes must occur or the stripes will no longer propagate.

4.5.1. Sorting Mechanisms Observed in MGD

An increase in the concentration and spatial autocorrelation of repton on the surface of the model space was associated with megaripple and megaripple stripe formation. As expected, this concentration increased over time as transport and ripple formation lead to the exhumation of repton slabs previously below the surface layer of the model. This is significant for megaripple formation because given an equivalent surface distribution of sediment and upwind supply, the bulk (subsurface) distribution is partly predictive of how rapidly megaripples will evolve in a given environment (Lämmel et al. 2018). The other component, not considered by MGD, is the variability of the wind regime. Importantly, even small increases in the bulk distribution of repton of one or two percent were found to increase the rate of megaripple formation. It was found that initial bulk concentrations of repton slabs between 2.4 and 4.7% favoured megaripple stripe formation. Below 2.4% there were too few repton slabs to initiate megaripple nucleation. Above 4.7% there were too many repton, which caused nucleation everywhere simultaneously, quickly filling the model space and impeding stripe development.

Modelling results from MGD suggest that the locations of concentrations of repton generated by erosion is unpredictable. A limited set of parameters consistently led to megaripple stripe formation, but due to the stochastic nature of the model it could not be determined with great precision when or where the nucleation sites would develop. This element of randomness that leads to nucleation site development was especially important in conditions where repton slabs were supply-limited because the formation of only a few of these sites is what caused the emergence of megaripple stripes in the model. Importantly, the nucleation sites served to interrupt the migration of impact ripples in the model space and lead to megaripple development. The impact ripples reached a wavelength approximately equal to the transport length of the salton slabs (30 slabs). The migration of impact ripples in the model can then be interpreted as the hopping of saltons from the stoss slope of one ripple to the next. Once a patch of coarse grains exceeds the length of the shadow zone of the upwind ripple, however, this synchronization between salton hop length and wavelength is interrupted and an armour layer can begin to grow. The migration of the

ripples in all cells downwind of the nucleation site is disrupted by this armour layer because the synchronization between hop length and ripple wavelength ceases. Instead of saltons hopping from ripple to ripple, the saltons are transported onto the stoss slope of the newly developing megaripple or into its larger shadow zone. This effectively stops the rapid transport of saltons and allows for the much slower and shorter hops of the reptons to lead to more megaripple development. For example, consider a repton slab and a salton slab at the base of a megaripple stoss slope with a length of 40 slabs. The salton, with its transport length of 30 slabs and 100% erosion probability, climbs the megaripple and will then be in its shadow zone after only 2 iterations. It is then trapped in the shadow zone of the megaripple and will not be able to be transported until the megaripple has migrated over it. If it is exhumed after the megaripple has crossed over it, then it will simply repeat the process of crossing over the megaripple again and returning to the shadow zone. By contrast, a repton with a transport length of 3 slabs and 20% erosion probability will require 67 iterations before it has climbed the 40 slabs, if it remains on the surface layer throughout its climb. Once nucleation sites form and megaripples grow their effect is to trap saltons and allow reptons to become more dominant on the surface of the model. This creates a positive feedback effect and explains why the repton concentration on the surface layer increases rapidly once megaripple formation is initiated.

Bedform collision may be an additional important mechanism in the megaripple stripes. This is particularly the case in the megaripple corridors. Small megaripples migrate more rapidly than large megaripples, generating collisions that lead to the smaller megaripples coalescing with the larger megaripples (Yizhaq et al. 2012b). This leads to further growth of the megaripples. Although migration and collision do occur in impact ripples, these interactions are typically not constructive in nature because the grains involved are saltons and the ripple will be rapidly reduced in size by the wind. However, this latter effect is not reproduced in MGD.

Spanwise transport and avalanching in the crosswind direction are two mechanisms that can cause crosswind sorting of grains. The curvature of megaripples in the megaripple corridors suggests that

there is a reinforcing mechanism for spanwise transport and crosswind avalanching. Crosswind avalanching is the spanwise sorting of grains caused by grainfall, where the curvature of the megaripples would lead to grains avalanching on their lee slopes to preferentially remain in the megaripple corridors. Although the obvious crosswind nature of the megaripple stripes suggests that spanwise transport may be essential for their development, limited evidence for these effects was found in MGD. This is caused by a simplifying assumption made in the model that leads to a lack of verisimilitude. In MGD, all slabs of the same type have the same erosion probability regardless of their location in the model space (except for the shadow zone). This is perhaps the most consequential difference between MGD and natural aeolian processes: each slab in MGD has a universal set of behaviours associated with it under all conditions. By contrast, the transport probability of reptions in a real megaripple field varies dramatically based on location. This makes the differential transport likelihood present in natural megaripple stripes irreproducible in MGD. The consequence of this is that the megaripples in MGD are likely migrating too rapidly and grow to unrealistically large sizes if the model is run for more than approximately 10 000 iterations. Further, the lack of crosswind sorting and differential erosion probabilities are causing the megaripples to expand crosswind more rapidly than expected. This explains the short lifespan of megaripple stripes in the model. The crosswind expansion of megaripples is expected to be much slower in natural environments than in MGD. Because of this, megaripple stripes are perhaps more stable and long-lived features than the model suggests. Of course, this is location dependent, and it is expected that there is large variability in the lifespan of megaripple stripes at each of the sites presented. Megaripple stripes can emerge in the model space despite the lack of differential and location-based transport behaviours, so these likely play a more important role in maintaining the pattern than in causing it to emerge. Figure 4.2 summarizes some of the small-scale sorting behaviours thought to be occurring in megaripple stripes. Further research must be done to constrain these effects and their importance for megaripple stripe development. A probabilistic explanation will now be explored and discussed to better explain the importance of spanwise transport, differential erosion probabilities, and the bulk distribution in megaripple stripes.

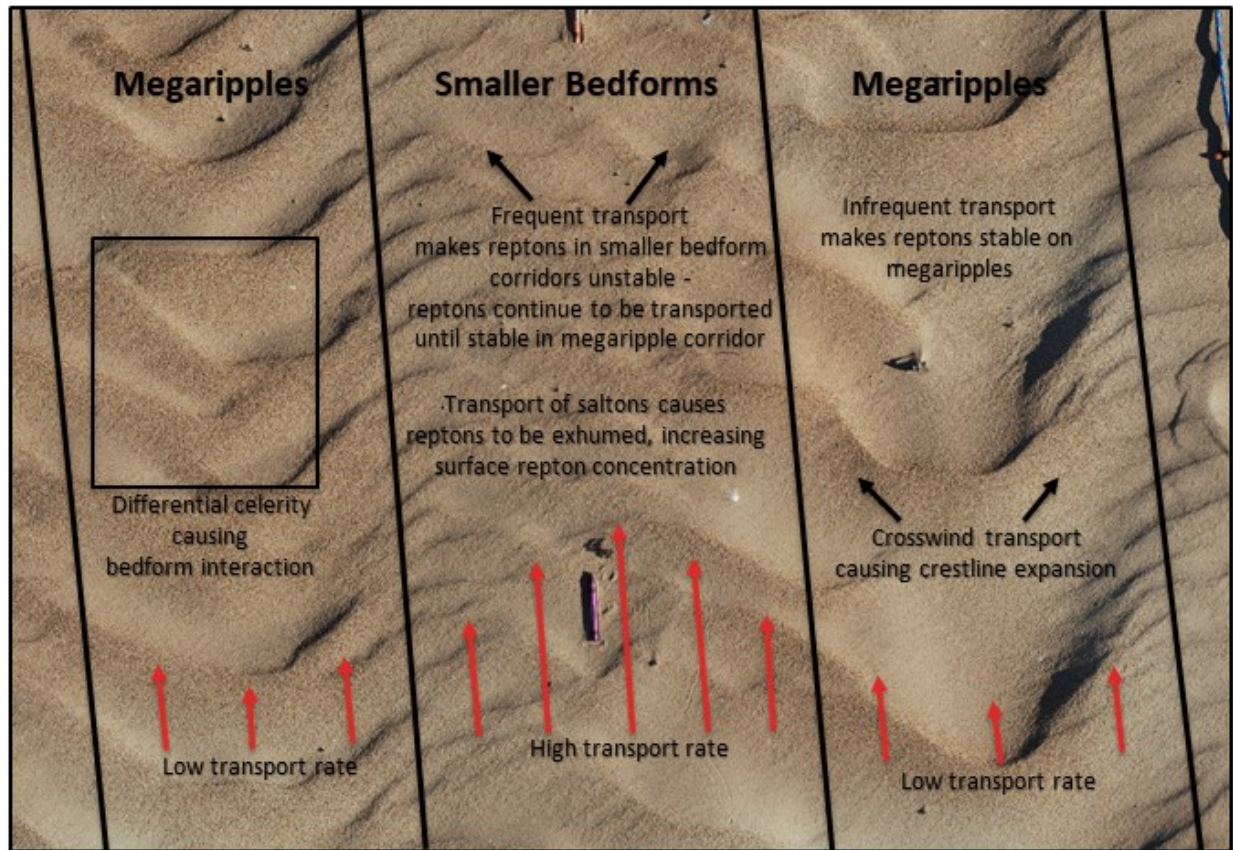


Figure 4.2: Small-scale processes and sorting mechanisms occurring in the corridors of megaripple stripes. Red arrows indicate assumed rate of transport at different locations. Black arrows indicate spanwise transport caused by reptation.

4.5.2. Quantifying Sorting Effects: A Random Walk and Markov Chain Approach

The effects of spanwise transport represent an interesting challenge for aeolian geomorphology and require significantly more research. Recent experimental work has shown that reptons are transported with a spanwise component (O'Brien and McKenna Neuman 2016). It was suggested above that a sorting mechanism for megaripple stripes is that reptons on the stoss slopes of the smaller bedform corridors are subject to a higher rate of bombardment and transport than reptons in the megaripple corridors. This leads to differential, location-based transport properties for grains of the same size. However, this effect could not be modelled in MGD. In lieu of this, a simple random walk and Markov chain approach will be shown and discussed here as useful tools for demonstrating the potential importance of spanwise transport in megaripple stripes.

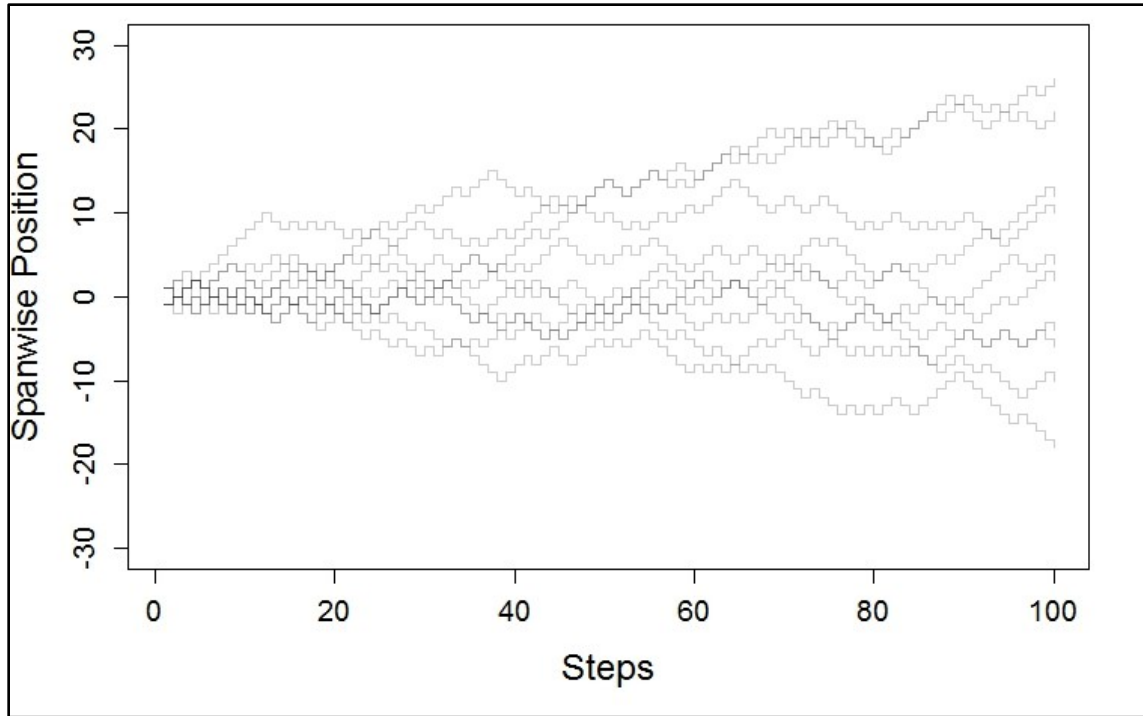


Figure 4.3: *Example of 10 random-walk slab paths through an idealized model space with no influences other than spanwise transport.*

Figure 4.3 plots a random walk through a model space for ten retons with $P(\theta)$ of 1 and no directional bias. This random walk is simply a binomial distribution represented graphically; this is essentially a spatial representation of the successive outcomes of a coin flip. Of course, this random walk model is two-dimensional and does not account for any additional complexities of ripple development (topography, avalanching, etc.), but it effectively shows that slabs with the capacity for spanwise transport moving through a model space can migrate laterally. The development of a self-organized pattern, however, requires that there be areas with conditions that lead to different transport probabilities. This is the mechanism that is lacking in MGD and why only minimal effects of spanwise transport were found (Figure 3.13). It is therefore necessary to show that if the transport of retons occurs at a higher rate in megaripple corridors than smaller bedform corridors, then spanwise transport is a more significant sorting mechanism than could be modelled by MGD. An expansion of the random walk model, a ‘gambler’s ruin’ probability model, can be used to show this.

An adaptation of the gambler's ruin problem can be used to determine the average number of steps a repton slab with a given $P(Er)$ and $P(\theta)$ will take through a model space before it will have moved to a spanwise position $\pm Y$. Given equal probabilities of moving left and right, the mean number of steps before a repton slab at a given position Y_1 reaches either of two barriers at positions Y_2 and Y_3 can be determined. Feller (1968) shows that in a random walk the average number of steps, n , before either position Y_2 or Y_3 is reached is given by:

$$n = (Y_1 - Y_2) * (Y_3 - Y_1), \text{ where } Y_2 < Y_1 < Y_3 \quad [9]$$

For example, consider a repton slab in the model space that is in a smaller bedform corridor at Y position 240. The slab has a megaripple corridor that is 30 cell positions to its right and another megaripple corridor 60 cell positions to its left. If the $P(\theta)$ of a repton in the smaller bedform corridor is set to 0.7 and the $P(Er)$ is set to 0.4, the mean number of model iterations, E_n it will take for that slab to be incorporated into the megaripple corridor can be estimated with:

$$E_n = \frac{1}{P(Er) * P(\theta)} * n \quad [10]$$

In this example, the mean expected number of iterations before this slab would be transported from smaller bedform corridor to megaripple corridor is 6429. If the transport probability in the megaripple corridor is set to be significantly lower, 0.1 for example, to reflect the expected decrease in transport rate, then the mean number of iterations for a repton in the same position in a megaripple corridor to be transported to a smaller bedform corridor is 25 714. This effectively demonstrates that reptons transported with a spanwise component would leave an environment with a high transport rate and accumulate in one with a low transport rate. In fact, this rate of exchange is simply determined by the ratio of the $P(Er)$ between the corridor types. In the example above, this ratio is 4:1, and the simplified statement can be made that the expected rate of repton departure from smaller bedform corridor to megaripple corridor is quadruple the expected rate in the opposite direction. By extending this idea of the

rate of exchange between corridor types, a simple Markov chain can be developed to demonstrate how the concentrations of retons in each corridor may evolve. A transition probability matrix for the rate of repton exchange between the corridor types can be defined as:

$$\begin{bmatrix} MR \rightarrow MR & MR \rightarrow SB \\ SB \rightarrow MR & SB \rightarrow SB \end{bmatrix}$$

where $MR \rightarrow MR$ is the probability of a repton in a megaripple corridor remaining in a megaripple corridor, $MR \rightarrow SB$ is the probability of a repton in a megaripple corridor migrating to a smaller bedform corridor, etc. The initial concentrations of retons is described by the initial state matrix:

$$[MR \text{ Repton } \% \quad SB \text{ Repton } \%]$$

For example, maintaining the arbitrary 4:1 ratio used in the example above and initial repton concentrations of 70% in the megaripple corridor and 30% in the smaller bedform corridor, the rates of exchange between corridor types can be defined as:

$$\begin{bmatrix} 0.975 & 0.025 \\ 0.900 & 0.100 \end{bmatrix}$$

For a single iteration, 97.5% of the retons in a megaripple corridor will remain and 90% of retons in a smaller bedform corridor will remain; the rest are exchanged. After one iteration of the transition probability matrix, the concentrations of retons in the corridors becomes:

$$[0.7125 \quad 0.2875]$$

This demonstrates that the initial concentrations are imbalanced with the rate of exchange between corridor types, and the concentration in the megaripple corridor will continue to increase until it reaches equilibrium. By extending out the Markov chain, the equilibrium concentration of retons in the corridors is the stationary matrix determined by the 4:1 ratio of exchange between the corridor types:

[0.8 0.2]

In this highly simplified representation of megaripple stripes, the degree of sorting between corridors is governed by their relative rate of repton exchange. Of course, these values reflect arbitrary initial values and rates of time. Further, this approach assumes that the rates of exchange do not change over time, an assumption that is surely false as it does not account for the variability of the wind, upwind sources, ripple topography, and other complications. Nevertheless, it serves to demonstrate that if there is spanwise transport and the expected rate of transport from smaller bedform to megaripple corridor is greater than that from megaripple to smaller bedform corridor, then the megaripple stripe pattern will be reinforced by spanwise sorting. In fact, the ratio of exchange between corridor types is the value that determines the extent of the sorting. Finally, the sorting will never be complete if there is some expected rate of reptons leaving megaripples and remaining in smaller bedform corridors.

The objective of the above was to show that a differential rate of transport between corridors allows for spanwise transport to have a sorting effect. Because no differential rate existed in MGD, the effects of spanwise transport were minimal. This means that the impact of spanwise transport is closely related to the erosion probability and is only expected to be consequential in environments where there are different location-based erosion probabilities and transport behaviours. Importantly, spanwise transport is not expected to have a significant effect when there is an abundance of reptons because the expected rate of transport will be relatively similar throughout the bedform field.

Unfortunately, experimental evidence for spanwise transport is limited and its effects could not be demonstrated in MGD. The allowance for location-based erosion probabilities would represent an improvement to MGD's verisimilitude but would also require the development of rules on how these erosion probabilities are determined. This could possibly be done through local calculations of slab elevation, spatial autocorrelation, and other parameters. As MGD was able to demonstrate megaripple stripe formation without spanwise transport, it is not the only relevant quantity determining repton

concentration and distribution. Another quantity, the exchange of reptons between surface and subsurface, was well-reproduced and easily measured by MGD (§3.5.3.). This process can also be modelled by a Markov chain and then compared to the outputs from MGD. This allows for an evaluation of the effectiveness of the Markov chain method. The relative transition probability matrix for the exchange of saltons between the surface layer of the model and the bulk distribution is:

$$\begin{bmatrix} \text{Salton} \rightarrow \text{Salton} \% & \text{Salton} \rightarrow \text{Repton} \% \\ \text{Repton} \rightarrow \text{Repton} \% & \text{Repton} \rightarrow \text{Salton} \% \end{bmatrix}$$

where $\text{Salton} \rightarrow \text{Salton} \%$ is the probability of the surface of the model space occupied by a salton remaining a salton, $\text{Salton} \rightarrow \text{Repton} \%$ is the probability of the surface of the model space occupied by a salton becoming occupied by a repton, and so on. Simplistically, the relevant quantities for determining these values are the erosion probabilities of saltons and reptons and the bulk distribution of saltons and reptons:

$$\begin{bmatrix} P(\text{Er}(\text{Salton})) * \text{Salton Bulk} \% & P(\text{Er}(\text{Salton})) * \text{Repton Bulk} \% \\ (P(\text{Er}(\text{Repton})) * \text{Repton Bulk} \%) + (1 - P(\text{Er}(\text{Repton}))) & P(\text{Er}(\text{Repton})) * \text{Salton Bulk} \% \end{bmatrix}$$

Using values from MGD simulations presented in Table 2.1, the matrix becomes:

$$\begin{bmatrix} 1 * 0.965 & 1 * 0.035 \\ ((0.2 * 0.035) + (1 - 0.2)) & 0.2 * 0.965 \end{bmatrix},$$

which yields:

$$\begin{bmatrix} 0.965 & 0.035 \\ 0.807 & 0.193 \end{bmatrix}$$

Using the initial surface concentrations of saltons and reptons used from the associated bulk distribution, the initial state matrix for the surface concentrations is:

$$\begin{bmatrix} 0.965 & 0.035 \end{bmatrix}$$

After one iteration of this Markov chain, the surface concentrations have changed to:

$$[0.93798 \quad 0.06202]$$

The Markov chain then reaches the stationary matrix:

$$[0.84649 \quad 0.15351]$$

This makes clear that the erosional conditions and bulk distribution are not in equilibrium with the initial surface conditions because the surface concentration increased rapidly despite no change in the bulk concentration. In fact, the equilibrium surface repton concentration is 439% of the bulk distribution. Clearly, the bulk distribution alone is not predictive of the surface distribution and there must also be some understanding of the relative erosion probabilities of the surface materials. In brief, this demonstrates that once a repton is present at the surface, it is more likely to remain there than a salton. This was also the case in MGD and is why repton surface concentrations immediately increased in all simulations. The simplified Markov chain representation of the evolving surface concentration of reptons compares very well with that observed in MGD during the first half of a typical simulation (Figure 4.4). After 5 000 iterations in MGD, however, it is evident that the exchange between subsurface and surface is no longer occurring at the same rate and that megariipple development allows for a rapid increase in repton surface concentration that is unaccounted for by this simple surface-bulk exchange rate. This rapid increase is thought to be the effect of the nucleation sites and the large shadow zones of megariipples discussed above. Of course, there is no three-dimensional simulation of evolving stratigraphy and topography in the Markov chain. Further, the Markov approach assumes that an eroded slab is always replaced by a subsurface slab, when the space vacated by the eroded slab may be filled by another surface slab transported from upwind or an avalanching slab. These processes affect the evolving surface concentration in ways which cannot be reliably accounted for in this simple statistical model.

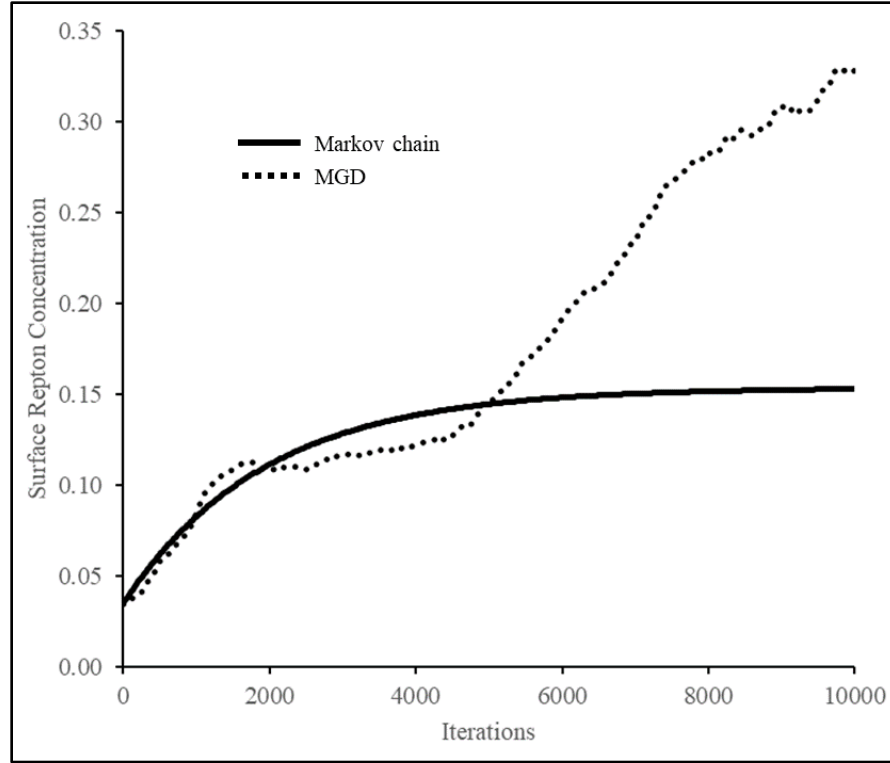


Figure 4.4: Comparison of an MGD simulation with initial repton concentration of 3.5% (same as shown in Figure 3.17) and Markov chain described in text. In the first 5000 iterations, the Markov chain is within 1.6% of the repton surface concentration measured in MGD. The disagreement between the two after approximately 5000 iterations is associated with megaripple stripe formation in the model space and the point at which topographic and shadow zone effects likely become more significant than the original bulk distribution and erosion probabilities. The Markov chain was adjusted to the MGD results so that one iteration of the chain was associated with 500 iterations in MGD.

As shown by MGD and the Markov chain model above, it is not solely the bulk distribution that results in megaripple formation, but a series of interactions and exchanges caused by the different behaviours of reptons and saltions (Lämmel et al. 2018). This is an important case study in the subtle but important distinction between *grain size* and *grain behaviour*. The former only requires knowledge of the GSD; the latter knowledge of GSDs and their transport environment. It is therefore more appropriate to distinguish between grain behaviour rather than grain size in bedform research. However, these distinctions are fraught with difficulty because of the inconsistencies and inaccuracies in estimating and measuring transport behaviour in natural environments (Barchyn et al. 2011). In MGD these inaccuracies

are removed because grain size is not explicitly modelled, and slabs are given consistent behaviours. However, this simplified conceptualization did not sufficiently account for the spatial variations in aeolian transport; one set of inaccuracies was simply replaced by another.

4.6. Megaripple Stripe Destruction: Oceano Case Study

The megaripple stripes at the Oceano Dunes are found directly downwind of large foredunes and there is evidence that strong winds in the area have caused frequent foredune blowouts, including one recently (Figure 4.5). This appears to have caused the destruction of several megaripple stripes which were present in 2011 satellite imagery but not in 2017 imagery. It is unclear whether all megaripple stripes in the area were destroyed and those seen in the 2017 image redeveloped or are the surviving stripes from the blowout event. The small scale of the features and the resolution of the imagery make this difficult to determine definitively. If the stripes did redevelop, they did so relatively rapidly. Because of the small scale of megaripple stripes at the Oceano Dunes, the site's ease of access, and the frequency of above-threshold winds in the area (Namikas et al. 2003; Adhikari 2017), this site is an excellent candidate for a field experiment similar to that conducted by Yizhaq et al. (2012a). For example, the stripes in the area could be flattened and revisited regularly to track the evolving re-emergence of the pattern and the evolution of the GSD. Lämmel et al. (2018) suggest that megaripples develop an increasingly bimodal distribution over time. If the megaripple stripes at Oceano were in fact destroyed and redeveloped, their relative youth may be a simple explanation for the lack of bimodality observed in the acquired samples. The two mechanisms that can destroy the megaripple stripe pattern is the influx of reptons causing crosswind expansion of megaripples or winds that exceed the transport threshold of the coarse grains and flatten the bedforms (Bagnold 1941; Isenberg et al. 2011). The former would be a very slow process, whereas the latter might occur in a matter of minutes in sufficiently strong wind.

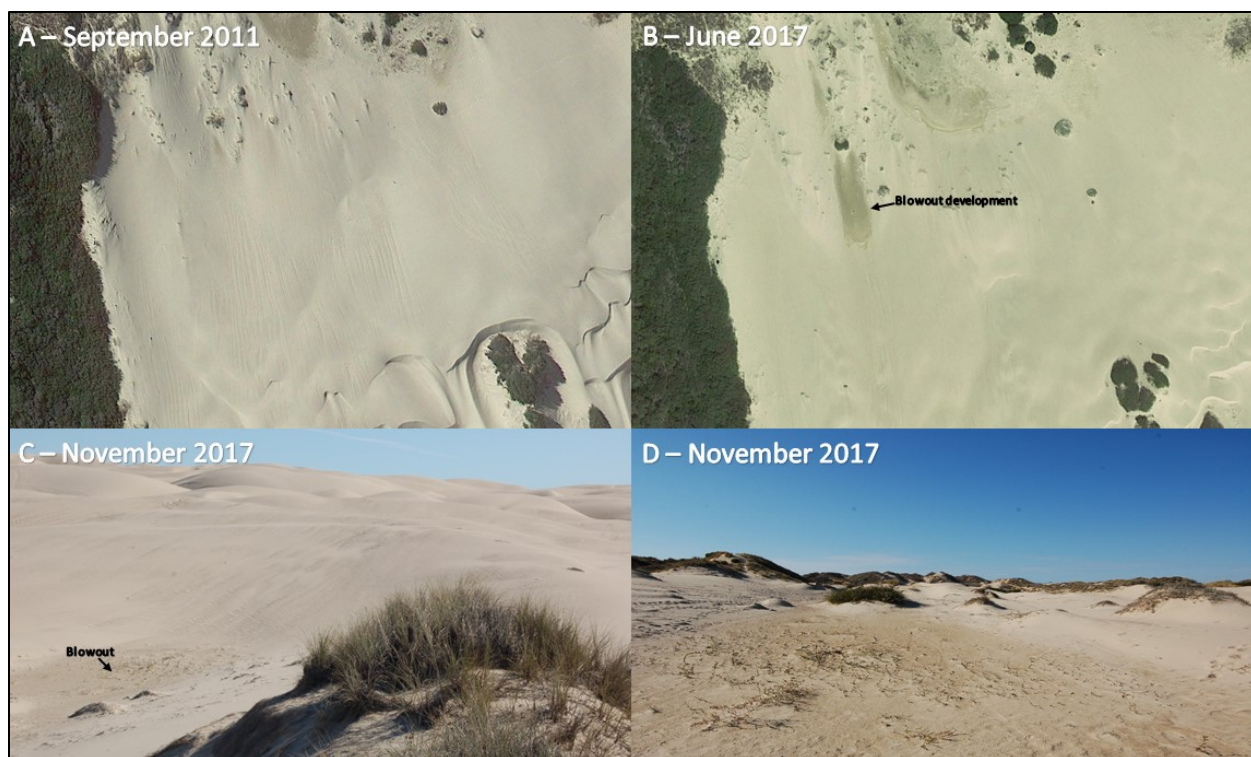


Figure 4.5: *A) View of the area where megariipple stripes are developing at the Oceano Dunes in 2011. B) The same location in 2017. A significant wind event or series of events likely caused the development and expansion of blowouts in the area. Although perhaps due to the different lighting and resolution of the two images, the image from 2017 appears to show fewer megariipple stripes than the 2011 image. C) Image of megariipple stripes and the recently developed blowout. D) The same blowout facing towards the coast and the foredune.*

4.7. Summary of Megariipple Stripe Formation and Development

In summary, the major factors that control megariipple stripe formation are thought to be:

1. Bulk-surface repton exchange determined by the rate of exhumation from the local bulk concentration and the transport of reptons from upwind sources. This presence of local concentrations of reptons causes the development of nucleation sites from which megaripples develop. The bulk and surface repton concentrations must be low (relative to megaripples) for megariipple stripes to develop.

2. The exchange of reptons between corridors is thought to be determined by spanwise transport and differential erosion probabilities. The rate of transport between corridor types differ because they are reliant on reptation and saltation, respectively.
3. Effects caused by megaripple development, including avalanching and ripple coalescence.
4. Changes in source material/upwind input.
5. The variability of the wind regime. Megaripple stripes are suspected to occur only in unimodal transport regimes.

The first three were modelled to some extent by MGD and the above statistical methods. The impacts and importance of the latter two remain uncertain. Megaripple stripes are clearly complex features dependent on many mechanisms and no one model used in this thesis can account for all the factors affecting their formation and development. Allen (1968) attempts to simplify the issues of bedform formation by reducing the fluid-sediment system in question to three problems: “(1) the type of force causing instability: (2) the kinematic structure of the developed unstable motion; and (3) the quantity or quantities which determine the physical scale (spatial periodicity or wave number) of the developed motion.” (p. 163). In the case of megaripple stripes, the first is simply the force of the wind exerted on the grains. The second illustrates why megaripple stripes are a difficult feature to analyze and are somewhat paradoxical: there are two structures, impact ripples and megaripples, which develop because of the same force. As demonstrated by the two-species model, the explanation for this is not that the nature of the force is different in each corridor but rather that the properties of the grains interacting with the force vary spatially. This was shown to be the case by the difference in observed grain size between the two corridor types and by the success of a two-species approach in a model with no explicit airflow component. The nature of the transport in each corridor, reptation and saltation, explains the third point of the quantities which determine the observed difference in wavelength between the corridor types. Reptation leads to the formation of megaripples, and saltation to the formation of impact ripples. In addition to sorting caused by reptation, the evolution of topography and the exhumation of coarse grains from the subsurface are

additional conditions promoting megaripple development. The only fundamental difference between megaripples and megaripple stripes is that the GSD of the latter must have a limited supply of reptating grains, where the ‘demand’ for such grains in this case is defined as the potential surface area of megaripples. If this hypothesis is extended to megaripple stripes on Mars, then these features represent an interesting test case for the typical assumption of reptation-driven megaripple formation and the more recently developed ‘fluid-drag hypothesis’ for large martian ripples (Lapotre et al. 2016; Lapotre et al. 2018). Although this hypothesis matches the scaling of large martian ripples and provides an explanation for the superimposition of impact ripples and megaripples on Mars, it does not offer a mechanism to explain such crosswind segregation.

4.8. Megaripple Stripe Classification

Megaripple stripes, along with sand strips, ripple streaks, and perhaps some fields of linear dunes, fall under the broad definition of ‘wind streaks’ presented by Greeley and Iversen (1985) because they are a “lineal surface pattern of aeolian origin” (p. 302). As Cohen-Zada et al. (2017) rightly point out, however, this definition is broad and primarily suited to remote sensing approaches rather than actual morphological origin (e.g., Zimbelman and Williams 1996). Further, simply classifying all these features as wind streaks does not allow for any further distinction based on the presence or absence of bedforms, grain size properties, and other characteristics. In other words, although a lineal pattern may be diagnostic of certain features, it does not always have explanatory power to elucidate the conditions that led to the development of the features or their morphology. Megaripple stripes represent an interesting case because although they do have a photographic similarity to wind streak features, the mechanism of their formation and their GSD is more typical of megaripples. This is because wind streaks typically form as the result of differential erosion/deposition in the lee of an obstacle and the differences in surface coloration that result from these processes, whereas megaripple formation is driven by saltation and reptation processes (Greeley and Iversen 1985).

Megaripple stripes are notable because they have largely escaped description in the literature to date. To the author's knowledge, megaripple stripes or features similar to megaripple stripes as they are described in this thesis have been mentioned only four times in assorted publications (Newell and Boyd 1953, Haney and Grolier 1991; Durán et al. 2011; Silvestro et al. 2015). These reports have not gone into any depth in studying the pattern and all have used different terminology. Megaripple stripes have been described by Newell and Boyd (1955) as 'sand streams', by Haney and Grolier (1991) as 'streamers', by Silvestro et al. (2015) as a 'longitudinal ribbon pattern', and by Durán et al. (2011) as 'chiflones'. These terms are used to describe other features that do not match the characteristics of megaripple stripes as presented in this thesis. 'Streamer' is typically used only as a term for the 'sand snakes' that can develop in the saltation layer during transport (Baas and Sherman 2005; Baas 2008). Streamers are not bedforms, but an ephemeral feature in the saltation cloud occurring only during active transport. 'Ribbons', although they do form longitudinally to the direction of flow, do not display a pattern with two distinct wavelengths of features with crestlines transverse to the transport direction. Further, 'ribbon' is a term typically reserved for subaqueous features (e.g., Allen 1968; Kenyon 1970; McLean 1981) and is seldom used in aeolian literature. Sand ribbons in fluvial settings and sand strips in aeolian settings form when there is a limited supply of readily transportable material and a large supply of non-erodible material. In megaripple stripes, this situation is inverted. To further the confusion regarding this term, Baas (2008) states that sand streamers are also referred to as 'ribbons' by some workers.

Haney and Grolier (1991) describe the megaripple stripes in Peru as "curvilinear bands parallel to wind direction; overprinted by transverse ripples". Describing the pattern as 'overprinted' by transverse ripples suggests that the features evolved in two distinct stages (the formation of wind streaks followed by the development of ripples), when there does not appear to be evidence for this at any of the sites observed. In other words, megaripple stripes are not interpreted in this thesis as a multigenerational feature. Rather, they are a megaripple-type feature which emerges from the bed given the appropriate GSD and transport environment.

Durán et al. (2011) refer to the individual “crescent-shaped structures” (p. 267), which are the features that compose the megaripple corridors of the stripes, as “chiflones” (p. 267). ‘Chiflone’ is an obscure and antiquated term which has been adapted from Spanish used in some literature to refer to chains of dunes (e.g., Broggi 1952; Norris and Norris 1961). Outside of the usage by Durán et al. (2011), ‘chiflone’ has never, to the author’s knowledge, been used to describe ripple-scale features. Durán et al. (2011) assess that these ripple-scale chiflones are a type of megaripple which form only in environments where coarse grains are in limited supply, but do not expand on their description of the features or their origins. With all of this considered, it is clear that megaripple stripes are largely undocumented, poorly understood, and that no consistent terminology exists to characterize the pattern. ‘Wind streak’, ‘ribbons’, ‘chiflones’, and ‘streamers’ are inadequate as terms to describe these features because they already refer to different types of bedforms. It is suggested that ‘megaripple stripes’ is a simple, unambiguous term that encapsulates both the nature of the bedforms and their pattern.

Chapter 5: Conclusion

5.1. Summary of Site Observations and Hypotheses

The observations at each site suggest some common properties of megaripple stripes. There is some variation in the pattern between sites, but the similarity of the features at each site is remarkable. The relative rarity of megaripple stripes suggests that there is a rather strict set of environmental conditions that lead to their formation. The distinguishing properties of megaripple stripes are thought to be:

1. A poorly-sorted GSD with a spanwise sorting of grains into distinct corridors. The coarse grains for which reptation is the dominant transport mode are supply-limited so that they cannot provide a megaripple armour layer throughout the entire bedform field.
2. Alternating crosswind megaripple corridors with larger megaripple features and relatively coarser grains, and smaller bedform corridors with relatively smaller grains and ripples.
3. Although most sites lack strong meteorological data, the orientation of other features (e.g., barchans, yardangs), small datasets, and anecdotal reports from each site suggest a largely unimodal regime of above-transport-threshold winds for saltons at all megaripple stripe locations. Additionally, the features were successfully reproduced in a numerical model using a single transport direction.
4. A correlation between crosswind wavelength of the corridors and downwind wavelength of the megaripples (approximately 2:1). By extension, this likely means a positive relationship between grain size and wavelength (Katra and Yizhaq 2015).

This thesis was centred on two hypotheses about megaripple stripes. The first was that the corridors in megaripple stripes are characterized by distinct grain sizes, with larger grains present in the corridors of megaripples and finer grains in the corridors of impact ripples. This was shown to be the case using data acquired from physical samples at the Oceano Dunes, California and photosieving data acquired from

Abra Pomez, Argentina. The second hypothesis was that megaripple stripe development is dependent on a limited supply of reptons. Using a modelling approach with a repton species and a salton species, it was demonstrated that a narrow range of bulk repton concentrations in the model space produced megaripple stripes. Below this range, only impact ripples developed. Above this range, megaripples developed rapidly throughout the model space because the reptons were not in short supply.

In addition to these two hypotheses, several additional findings were made. This includes insight into the concept of nucleation sites, which are local concentrations of reptons from which megaripples develop and extend downwind. Local and global spatial autocorrelation of reptons was demonstrated as a cause of megaripple formation and development. A simple random-walk model and Markov chain were used to show that crosswind sorting is likely an important mechanism in maintaining the megaripple stripe pattern. This spanwise sorting mechanism could not be reproduced in MGD because of the lack of location-based erosion probability. The same Markov chain approach was used to show how the exchange rate of reptons and saltons between the surface and subsurface in the early stages of the model could be determined using the relative erosion probabilities and concentrations of each slab type.

In conclusion, environments conducive to megaripple development and megaripple stripes are very similar, with the essential difference being that megaripple stripes form in environments with a limited supply of reptons. A hypothesis for megaripple stripe formation is that they arise from nucleation sites of high local concentrations of reptons that develop into corridors of megaripples. These corridors migrate slowly downwind and the rate of their downwind expansion is limited by the availability of reptons. Some megaripple stripes develop on the stoss slopes of dunes and others develop on otherwise largely featureless deposits. The majority of stripes have megaripple corridors that thin or disappear entirely downwind. Once nucleation sites develop and megaripple stripes begin to form, it becomes increasingly unlikely for new nucleation sites to develop because the majority of reptons are in the already-formed megaripples. This prevents the development of new nucleation sites and the formation of new megaripple corridors in the middle of a field of megaripple stripes. Reptons become relatively stable

on the upper stoss slopes of megaripples, where they are far less likely to be impacted and transported by saltating grains. Consequently, reptons that are not found in these areas are more likely to be transported. This means that there exists a differential rate of transport for reptons in an environment where they are supply-limited, and that reptons will continue to be transported at a higher rate until they find themselves on a megaripple. This sorting is caused by spanwise reptation. If the reptons at the surface remain supply-limited, the megaripple stripes will persist. If the concentration of reptons at the surface increases, the megaripple stripes will begin to grow crosswind until the megaripple corridors have connected and the entire field consists of megaripples. Given that these analyses relied on satellite imagery, field work from only two sites, and limited data from other publications, these are of course not yet definitive statements of conditions and processes. Rather, they provide a basis for further research into megaripple stripes.

5.2. Future Work

Megaripple stripes are poorly documented in the literature and consequently are poorly understood. The need for further research on megaripple stripes is clearly stated by Durán et al. (2011): “As there is no real understanding of the segregation processes [that lead to their development], these structures have not received any correct explanation so far” (p. 267). Given that this thesis is the first in-depth investigation of this bedform pattern, it is clear that they need to be more comprehensively investigated and documented. This thesis has endeavoured to begin the process of summarizing their morphologic characteristics and establishing working hypotheses for their formation. However, megaripple stripes may escape full classification and tidy characterization based on morphometric properties alone because of the unpredictable evolution and inconsistent GSDs of megaripples. This was summarized effectively by Lämmel et al. (2018), who comment that “measurements of megaripples will thus always retain an anecdotal character... at best capturing some more or less typical (not necessarily average) behaviour” (p. 761). Nevertheless, these features are an interesting geomorphological phenomenon and merit further investigation.

Field work and sample collection at the other terrestrial sites are logical next steps to further develop the hypotheses presented in this work. It is very probable that the pattern is found at multiple other locations on Earth and Mars and a search for these features has been an ongoing objective of this research. This search could also be extended to other planetary bodies with aeolian activity. Of course, the current limitation to discovering more of these features is image resolution, as any features with downwind wavelength of less than a few metres are extremely difficult to detect in most imagery.

A wind tunnel study would be an appropriate next step in the experimental investigation of megaripple stripes. This thesis has presented data and conditions required for the development of megaripple stripes that could be tested in a controlled environment. However, the obvious limiting factor is that there is no wind tunnel that, to the author's knowledge, is of sufficient width to reproduce the corridor pattern because a minimum width of two metres is likely required to generate these features. Experimental verification of these features is therefore a limiting factor in our understanding of them, and until such time that they can be reproduced in a controlled environment the testing of these hypotheses and the observation of these features is limited to the relatively few examples available in the field and from imagery, in addition to modelling efforts such as the ones presented here.

References

- Ackert, R. P. (1989). The origin of isolated gravel ripples in the western Asgard Range, Antarctica. *Antarctic Journal of the United States*, 24(5), 60-62.
- Adhikari, P. (2017). *Assessment of Wind Regime and Sediment Transport Activity at Oceano Dunes, California*. Master's Thesis. University of Nevada, Reno.
- Allen, J. R. L. (1968). The nature and origin of bed-form hierarchies. *Sedimentology*, 10(3), 161-182.
- Almeida, M. P., Parteli, E. J., Andrade, J. S., & Herrmann, H. J. (2008). Giant saltation on Mars. *Proceedings of the National Academy of Sciences*, 105(17), 6222-6226.
- Anderson, R. S. (1987). A theoretical model for aeolian impact ripples. *Sedimentology*, 34(5), 943-956.
- Anderson, R. S. (1990). Eolian ripples as examples of self-organization in geomorphological systems. *Earth-Science Reviews*, 29(1-4), 77-96.
- Anderson, R. S., & Bunas, K. L. (1993). Grain size segregation and stratigraphy in aeolian ripples modelled with a cellular automaton. *Nature*, 365(6448), 740-743.
- Andreotti, B. (2004). A two-species model of aeolian sand transport. *Journal of Fluid Mechanics*, 510, 47-70.
- Andreotti, B., Claudin, P., & Pouliquen, O. (2010). Measurements of the aeolian sand transport saturation length. *Geomorphology*, 123(3-4), 343-348.
- Baas, A. C. W., & Sherman, D. J. (2005). Formation and behavior of aeolian streamers. *Journal of Geophysical Research: Earth Surface*, 110, F03011.
- Baas, A. C. (2007). Complex systems in aeolian geomorphology. *Geomorphology*, 91(3), 311-331.
- Baas, A. C. (2008). Challenges in aeolian geomorphology: investigating aeolian streamers. *Geomorphology*, 93(1), 3-16.
- Báez, W., Arnosio, M., Chiodi, A., Ortiz-Yañes, A., Viramonte, J. G., Bustos, E., & López, J. F. (2015). Estratigrafía y evolución del Complejo Volcánico Cerro Blanco, Puna Austral, Argentina. *Revista mexicana de ciencias geológicas*, 32(1), 29-49.
- Bagnold, R. A. (1941). *The physics of blown sand and desert dunes*. London: Methuen.

- Balme, M., Berman, D. C., Bourke, M. C., & Zimbelman, J. R. (2008). Transverse aeolian ridges (TARs) on Mars. *Geomorphology*, 101(4), 703-720.
- Barchyn, T. E., Hugenholtz, C. H., & Ellis, J. T. (2011). A call for standardization of aeolian process measurements: moving beyond relative case studies. *Earth Surface Processes and Landforms*, 36(5), 702-705.
- Barchyn, T. E., & Hugenholtz, C. H. (2012). A new tool for modeling dune field evolution based on an accessible, GUI version of the Werner dune model. *Geomorphology*, 138(1), 415-419.
- Barchyn, T. E., Martin, R. L., Kok, J. F., & Hugenholtz, C. H. (2014). Fundamental mismatches between measurements and models in aeolian sediment transport prediction: The role of small-scale variability. *Aeolian Research*, 15, 245-251.
- Barchyn, T. E., & Hugenholtz, C. H. (2015). Yardang evolution from maturity to demise. *Geophysical Research Letters*, 42(14), 5865-5871.
- Bridges, N. T., Spagnuolo, M. G., de Silva, S. L., Zimbelman, J. R., & Neely, E. M. (2015). Formation of gravel-mantled megaripples on Earth and Mars: Insights from the Argentinean Puna and wind tunnel experiments. *Aeolian Research*, 17, 49-60.
- Broggi, J. A. (1952). Migracion de arenas a lo largo de la costa Peruana. *Boletín de la Sociedad Geológica del Perú*, 24(1), 1-25.
- Buscombe, D. (2013). Transferable wavelet method for grain-size distribution from images of sediment surfaces and thin sections, and other natural granular patterns. *Sedimentology*, 60(7), 1709-1732.
- Clark, C. D. (1993). Mega-scale glacial lineations and cross-cutting ice-flow landforms. *Earth Surface Processes and Landforms*, 18(1), 1-29.
- Claudin, P. & Andreotti, B. (2006). A scaling law for aeolian dunes on Mars, Venus, Earth, and for subaqueous ripples. *Earth and Planetary Science Letters*, 252(1-2), 30-44.
- Cofaigh, C. Ó., Stokes, C. R., Lian, O. B., Clark, C. D., & Tulaczyk, S. (2013). Formation of mega-scale glacial lineations on the Dubawnt Lake Ice Stream bed: 2. Sedimentology and stratigraphy. *Quaternary Science Reviews*, 77, 210-227.

- Cohen-Zada, A. L., Maman, S., & Blumberg, D. G. (2017). Earth aeolian wind streaks: Comparison to wind data from model and stations. *Journal of Geophysical Research: Planets*, 122(5), 1119-1137.
- Colombini, M., & Parker, G. (1995). Longitudinal streaks. *Journal of Fluid Mechanics*, 304, 161-183.
- de Silva, S. L. (1989). Altiplano-Puna volcanic complex of the central Andes. *Geology*, 17(12), 1102-1106.
- de Silva, S. L. (2010). The largest wind ripples on Earth: Comment. *Geology*, 38(9), e218.
- de Silva, S. L., Spagnuolo, M. G., Bridges, N. T., & Zimbelman, J. R. (2013). Gravel-mantled megaripples of the Argentinean Puna: A model for their origin and growth with implications for Mars. *GSA Bulletin*, 125(11-12), 1912-1929.
- Diniega, S., Kreslavsky, M., Radebaugh, J., Silvestro, S., Telfer, M., & Tirsch, D. (2017). Our evolving understanding of aeolian bedforms, based on observation of dunes on different worlds. *Aeolian Research*, 26, 5-27.
- Durán, O., Claudin, P., & Andreotti, B. (2011). On aeolian transport: Grain-scale interactions, dynamical mechanisms and scaling laws. *Aeolian Research*, 3, 243-270.
- Durán, O., Claudin, P., & Andreotti, B. (2014). Direct numerical simulations of aeolian sand ripples. *Proceedings of the National Academy of Sciences*, 111(44), 15665-15668.
- Favaro, E. A., Hugenholtz, C. H., & Barchyn, T. E. (2017). Evolution and diagnostic utility of aeolian rat-tails: A new type of abrasion feature on Earth and Mars. *Aeolian Research*, 28, 91-98.
- Feller, W. (1968). *An introduction to probability theory and its applications*. Wiley, New York.
- Fenton, L. K. (2006). Dune migration and slip face advancement in the Rabe Crater dune field, Mars. *Geophysical Research Letters*, 33, L20201.
- Ferguson, R. I. & Church, M. (2004). A simple universal equation for grain settling velocity. *Journal of Sedimentary Research*, 74(6), 933-937.

- Francou, B., Méhauté, N. L., & Jomelli, V. (2001). Factors controlling spacing distances of sorted stripes in a low-latitude, alpine environment (Cordillera Real, 16° S, Bolivia). *Permafrost and Periglacial Processes*, 12(4), 367-377.
- Fryberger, S. G., Hesp, P., & Hastings, K. (1992). Aeolian granule ripple deposits, Namibia. *Sedimentology*, 39(2), 319-331.
- Gay Jr., S. P. (2005). Blowing sand and surface winds in the Pisco to Chala Area, Southern Peru. *Journal of Arid Environments*, 61(1), 101-117.
- Getis, A., & Ord, J. K. (1992). The analysis of spatial association by use of distance statistics. *Geographical Analysis*, 24(3), 189-206.
- Gillies, J. A., & Etyemezian, V. (2014). Wind and PM10 Characteristics at the ODSVRA from the 2013 Assessment Monitoring Network. *California Department of Parks and Recreation, Pismo Beach, California*.
- Goldthwait, R. P. (1976). Frost Sorted Patterned Ground: A Review. *Quaternary Research*, 6(1), 27-35.
- Greeley, R., & Iversen, J. D. (1985). *Wind as a Geological Process On Earth, Mars, Venus and Titan*. Cambridge: Cambridge University Press.
- Greene, L. L. (1995). *Eolian landforms in the Central Andes: implications for the long-term stability of atmospheric circulation*. Master's Thesis. Cornell University, New York.
- Hallet, B. (1990). Spatial self-organization in geomorphology: from periodic bedforms and patterned ground to scale-invariant topography. *Earth-Science Reviews*, 29(1), 57-75.
- Haney, E. M., & Grolier, M. J. (1991). *Geologic map of major Quaternary eolian features, northern and central coastal Peru* (No. 2162). United States Geological Survey.
- Hu, G., Jin, H., Dong, Z., Lu, J., & Yan, C. (2013). Driving forces of aeolian desertification in the source region of the Yellow River: 1975–2005. *Environmental Earth Sciences*, 70(7), 3245-3254.
- Hugenholtz, C. H., Barchyn, T. E., & Favaro, E. A. (2015). Formation of periodic bedrock ridges on Earth. *Aeolian Research*, 18, 135-144.

- Hugenholtz, C. H., & Barchyn, T. E. (2017). A terrestrial analog for transverse aeolian ridges (TARs): environment, morphometry, and recent dynamics. *Icarus*, 289, 239-253.
- Ibbeken, H., & Schleyer, R. (1986). Photo-sieving: A method for grain-size analysis of coarse-grained, unconsolidated bedding surfaces. *Earth Surface Processes and Landforms*, 11(1), 59-77.
- Isenberg, O., Yizhaq, H., Tsoar, H., Wenkart, R., Karnieli, A., Kok, J. F., & Kutra, I. (2011). Megaripple flattening due to strong winds. *Geomorphology*, 131(3), 69-84.
- Jackson, P. S., & Hunt, J. C. R. (1975). Turbulent wind flow over a low hill. *Quarterly Journal of the Royal Meteorological Society*, 101(430), 929-955.
- Jerolmack, D. J., Mohrig, D., Grotzinger, J. P., Fike, D. A., & Watters, W. A. (2006). Spatial grain size sorting in eolian ripples and estimation of wind conditions on planetary surfaces: Application to Meridiani Planum, Mars. *Journal of Geophysical Research: Planets*, 111, E12S02.
- Kutra, I., Yizhaq, H., & Kok, J. F. (2014). Mechanisms limiting the growth of aeolian megaripples. *Geophysical Research Letters*, 41(3), 858-865.
- Kenyon, N. H. (1970). Sand ribbons of European tidal seas. *Marine Geology*, 9(1), 25-39.
- Kessler, M. A., & Werner, B. T. (2003). Self-organization of sorted patterned ground. *Science*, 299(5605), 380-383.
- King, E. C., Hindmarsh, R. C., & Stokes, C. R. (2009). Formation of mega-scale glacial lineations observed beneath a West Antarctic ice stream. *Nature Geoscience*, 2(8), 585.
- Kocurek, G., & Ewing, R. C. (2005). Aeolian dune field self-organization—implications for the formation of simple versus complex dune-field patterns. *Geomorphology*, 72(1-4), 94-105.
- Kok, J. F., & Renno, N. O. (2009). A comprehensive numerical model of steady state saltation (COMSALT). *Journal of Geophysical Research: Atmospheres*, 114, D17204.
- Kok, J. F., Parteli, E. J., Michaels, T. I., & Karam, D. B. (2012). The physics of wind-blown sand and dust. *Reports on progress in Physics*, 75(10), 106901.
- Lämmel, M., Rings, D., & Kroy, K. (2012). A two-species continuum model for aeolian sand transport. *New Journal of Physics*, 14(9), 093037.

- Lämmel, M., Meiwald, A., Yizhaq, H., Tsoar, H., Katra, I., & Kroy, K. (2018). Aeolian sand sorting and megaripple formation. *Nature Physics*, 14, 759-765.
- Lancaster, N. (1995). *Geomorphology of desert dunes*. Routledge.
- Landry, W., & Werner, B. T. (1994). Computer simulations of self-organized wind ripple patterns. *Physica D: Nonlinear Phenomena*, 77(1-3), 238-260.
- Lapotre, M. G. A., Ewing, R. C., Lamb, M. P., Fischer, W. W., Grotzinger, J. P., Rubin, D. M., & Banham, S. G. (2016). Large wind ripples on Mars: A record of atmospheric evolution. *Science*, 353(6294), 55-58.
- Lapotre, M. G. A., Ewing, R. C., Weitz, C. M., Lewis, K. W., Lamb, M. P., Ehlmann, B. L., & Rubin, D. M. (2018). Morphologic diversity of Martian ripples: Implications for large-ripple formation. *Geophysical Research Letters*, 45(19), 10-229.
- Makse, H. A. (2000). Grain segregation mechanism in aeolian sand ripples. *The European Physical Journal E*, 1(2-3), 127-135.
- Martin, R. L., & Kok, J. F. (2018). Distinct thresholds for the initiation and cessation of aeolian saltation from field measurements. *Journal of Geophysical Research: Earth Surface*, 123(7), 1546-1565.
- McKenna Neuman, C. & Bédard, O. (2017). A wind tunnel investigation of particle segregation, ripple formation and armouring within sand beds of systematically varied texture. *Earth Surface Processes and Landforms*, 42(5), 749-762.
- McLean, S. R. (1981). The role of non-uniform roughness in the formation of sand ribbons. *Marine Geology*, 42(1-4), 49-74.
- Milana, J. P. (2009). Largest wind ripples on Earth? *Geology*, 37(4), 343-346.
- Milana, J. P., Forman, S., & Kröhling, D. (2010). The largest wind ripples on earth: REPLY. *Geology*, 38(9), e219-e220.
- Moran, P.A.P. (1950). Notes on continuous stochastic phenomena. *Biometrika*, 37, 17-23.
- Namikas, S. L. (2003). Field measurement and numerical modelling of aeolian mass flux distributions on a sandy beach. *Sedimentology*, 50(2), 303-326.

- Narteau, C., Zhang, D., Rozier, O., & Claudin, P. (2009). Setting the length and time scales of a cellular automaton dune model from the analysis of superimposed bed forms. *Journal of Geophysical Research: Earth Surface*, 114, F03006.
- Newell, N. D., & Boyd, D. W. (1955). Extraordinarily coarse eolian sand of the Ica desert, Peru. *Journal of Sedimentary Research*, 25(3), 226-228.
- Nield, J. M., & Baas, A. C. (2008). Investigating parabolic and nebkha dune formation using a cellular automaton modelling approach. *Earth Surface Processes and Landforms*, 33(5), 724-740.
- Norris, R. M., & Norris, K. S. (1961). Algodones dunes of southeastern California. *Geological Society of America Bulletin*, 72(4), 605-619.
- O'Brien, P., & McKenna Neuman, C. (2016). PTV measurement of the spanwise component of aeolian transport in steady state. *Aeolian Research*, 20, 126-138.
- O'Brien, P., & McKenna Neuman, C. (2018). An experimental study of the dynamics of saltation within a three-dimensional framework. *Aeolian Research*, 31, 62-71.
- Pye, K., & Tsoar, H. (2009). *Aeolian Sand and Sand Dunes*. Springer Berlin Heidelberg.
- Qian, G., Dong, Z., Zhang, Z., Luo, W., & Lu, J. (2012). Granule ripples in the Kumtagh Desert, China: Morphology, grain size and influencing factors. *Sedimentology*, 59(6), 1888-1901.
- Rasmussen, K. R., Valance, A., & Merrison, J. (2015). Laboratory studies of aeolian sediment transport processes on planetary surfaces. *Geomorphology*, 244, 74-94.
- Rubin, D. M. (2004). A simple autocorrelation algorithm for determining grain size from digital images of sediment. *Journal of Sedimentary Research*, 74(1), 160-165.
- Sagan, C., & Bagnold, R. A. (1975). Fluid transport on Earth and aeolian transport on Mars. *Icarus*, 26(2), 209-218.
- Schmerler, E., Katra, I., Kok, J. F., Tsoar, H., & Yizhaq, H. (2016). Experimental and numerical study of Sharp's shadow zone hypothesis on sand ripple wavelength. *Aeolian Research*, 22, 37-46.
- Shao, Y., & Lu, H. (2000). A simple expression for wind erosion threshold friction velocity. *Journal of Geophysical Research: Atmospheres*, 105(D17), 22437-22443.

- Shao, Y. (2008). *Physics and modelling of wind erosion*. Springer Science & Business Media.
- Sharp, R. P. (1963). Wind ripples. *The Journal of Geology*, 71(5), 617-636.
- Silvestro, S., Vaz, D. A., Di Achille, G., Popa, I. C., & Esposito, F. (2015). Evidence for different episodes of aeolian construction and a new type of wind streak in the 2016 ExoMars landing ellipse in Meridiani Planum, Mars. *Journal of Geophysical Research: Planets*, 120(4), 760-774.
- Siminovich, A., Elperin, T., Katra, I., Kok, J. F., Sullivan, R., Silvestro, S., & Yizhaq, H. (2019). Numerical study of shear stress distribution over sand ripples under terrestrial and Martian conditions. *Journal of Geophysical Research: Planets*, 124(1), 175-185.
- State of California (2018). Wind Data Collected at S1 Tower. Hourly Data 2011-2017. Retrieved August 5, 2018 from http://ohv.parks.ca.gov/?page_id=26819.
- Sullivan, R., & Kok, J. F. (2017). Aeolian saltation on Mars at low wind speeds. *Journal of Geophysical Research: Planets*, 122(10), 2111-2143.
- Tirsch, D., Jaumann, R., Pacifici, A., & Poulet, F. (2011). Dark aeolian sediments in Martian craters: composition and sources. *Journal of Geophysical Research: Planets*, 116, E03002.
- Valance, A., Rasmussen, K. R., El Moutar, A. O., & Dupont, P. (2015). The physics of Aeolian sand transport. *Comptes Rendus Physique*, 16(1), 105-117.
- Vitton, S. and Sadler, L., Particle-Size Analysis of Soils Using Laser Light Scattering and X-Ray Absorption Technology. *Geotechnical Testing Journal*, 20(1), 1997, 63-73
- Walker, J. D. (1981). *An experimental study of wind ripples*. Master's Thesis. Massachusetts Institute of Technology, Cambridge.
- Weitz, C. M., Sullivan, R. J., Lapotre, M. G., Rowland, S. K., Grant, J. A., Baker, M., & Yingst, R. A. (2018). Sand grain sizes and shapes in eolian bedforms at Gale crater, Mars. *Geophysical Research Letters*, 45(18), 9471-9479.
- Westoby, M. J., Brasington, J., Glasser, N. F., Hambrey, M. J., & Reynolds, J. M. (2012). 'Structure-from-Motion' photogrammetry: A low-cost, effective tool for geoscience applications. *Geomorphology*, 179, 300-314.

- Werner, B. T. (1995). Eolian dunes: computer simulations and attractor interpretation. *Geology*, 23(12), 1107-1110.
- Werner, B. T., & Hallet, B. (1993). Numerical simulation of self-organized stone stripes. *Nature*, 361(6408), 142.
- Wilson, I. G. (1972). Aeolian bedforms—their development and origins. *Sedimentology*, 19(3-4), 173-210.
- Yizhaq, H., Balmforth, N. J., & Provenzale, A. (2004). Blown by wind: nonlinear dynamics of aeolian sand ripples. *Physica D: Nonlinear Phenomena*, 195(3-4), 207-228.
- Yizhaq, H., Isenberg, O., Wenkart, R., Tsoar, H., & Karnieli, A. (2009). Morphology and dynamics of aeolian mega-ripples in Nahal Kasuy, southern Israel. *Israel Journal of Earth Sciences*, 57, 149-165.
- Yizhaq, H., Kutra, I., Isenberg, O., & Tsoar, H. (2012a). Evolution of megaripples from a flat bed. *Aeolian Research*, 6, 1-12.
- Yizhaq, H., Kutra, I., Kok, J. F., & Isenberg, O. (2012b). Transverse instability of megaripples. *Geology*, 40(5), 459-462.
- Yizhaq, H., & Kutra, I. (2015). Longevity of aeolian megaripples. *Earth and Planetary Science Letters*, 422, 28-32.
- Zimbelman, J. R., & Williams, S. H. (1996). Wind streaks: geological and botanical effects on surface albedo contrast. *Geomorphology*, 1(17), 167-185.
- Zimbelman, J. R., Williams, S. H., & Johnston, A. K. (2012). Cross-sectional profiles of sand ripples, megaripples, and dunes: a method for discriminating between formational mechanisms. *Earth Surface Processes and Landforms*, 37(10), 1120-1125.

Appendix A: Oceano Dunes Sample Grain Size Data

Table A.1: Summary of all 70 samples acquired from the Oceano Dunes. Grain sizes in μm .

SAMPLE ID	SITE ID	MR/SB	DEPTH/SURFACE	MEAN	D10	D50	D90
1	1	MR	Surface	685	445	655	963
2	1	MR	Surface	707	452	673	1005
3	1	SB	Surface	590	335	554	896
4	1	SB	Surface	588	330	552	901
5	1	MR	Depth	677	347	634	1072
6	1	MR	Depth	697	347	648	1119
7	1	MR	Depth	632	321	594	1003
8	1	MR	Depth	647	338	609	1017
9	1	SB	Depth	510	230	470	851
10	1	SB	Depth	550	243	503	926
11	1	SB	Depth	456	197	415	779
12	1	SB	Depth	494	207	457	838
13	1	MR	Surface	714	444	678	1033
14	1	MR	Surface	734	449	692	1072
15	1	MR	Surface	713	413	665	1075
16	1	MR	Surface	713	409	656	1049
17	1	SB	Depth	286	152	251	453
18	1	SB	Depth	429	156	316	879
19	1	SB	Depth	397	160	300	786
20	1	SB	Depth	573	179	493	1089
21	1	MR	Depth	601	230	562	1017
22	1	MR	Depth	637	225	594	1094
23	1	MR	Depth	666	261	620	1121
24	1	MR	Depth	653	265	612	1087
25	2	MR	Surface	725	485	694	1002
26	2	MR	Surface	713	477	683	988
27	2	SB	Surface	615	325	573	968
28	2	SB	Surface	606	328	569	940
29	2	MR	Depth	745	460	704	1083
30	2	MR	Depth	765	467	720	1121
31	2	MR	Depth	712	454	676	1016
32	2	MR	Depth	720	445	681	1047
33	2	SB	Depth	512	239	475	842
34	2	SB	Depth	511	241	474	840
35	2	SB	Depth	413	186	362	720
36	2	SB	Depth	395	184	352	672
37	3	MR	Surface	820	547	783	1140

38	3	MR	Surface	809	545	776	1114
39	3	MR	Depth	756	406	698	1187
40	3	MR	Depth	759	391	703	1216
41	3	MR	Depth	804	445	746	1249
42	3	MR	Depth	806	447	747	1252
43	3	SB	Surface	528	310	499	790
44	3	SB	Surface	522	319	497	761
45	3	SB	Depth	318	180	295	490
46	3	SB	Depth	313	177	290	480
47	3	SB	Depth	386	200	356	620
48	3	SB	Depth	373	197	345	591
49	3	Transition	Depth	325	186	305	495
50	3	Transition	Depth	401	189	358	682
51	4	MR	Surface	647	162	618	1226
52	4	MR	Surface	705	167	684	1291
53	4	Transition	Depth	300	146	235	431
54	4	Transition	Depth	234	150	223	331
55	4	SB	Depth	243	156	232	345
56	4	SB	Depth	244	157	233	346
57	4	Transition	Depth	240	156	230	340
58	4	Transition	Depth	250	153	236	365
59	4	MR	Depth	601	171	519	1171
60	4	MR	Depth	536	166	422	1069
61	4	MR	Depth	831	406	793	1337
62	4	MR	Depth	822	457	786	1272
63	4	Transition	Depth	242	155	230	344
64	4	Transition	Depth	235	152	225	331
65	4	SB	Depth	231	156	223	318
66	4	SB	Depth	235	152	225	332
67	4	Transition	Depth	240	156	230	338
68	4	Transition	Depth	259	156	240	375
69	4	MR	Depth	805	265	775	1322
70	4	MR	Depth	811	301	778	1335

Appendix B: Repton Score

As a supplement to the main text of this thesis, a simple alternative characterization of megaripple stripes in terms of grain behaviour rather than grain size is presented here. As a consequence of the low reliability of the wind data and the complexities of transport of grains of different densities, these data were not of sufficient quality to be included in the main text. Nevertheless, the simple ‘repton score’ model developed offers a simple and novel way to pair grain size to wind data to assess the nature of transport.

B.1. Meteorological Data

Wind data were acquired from the Oceano Dunes and Argentina. The Oceano Dunes data was collected from the Oceano Dunes State Vehicular Recreation Area S1 tower and spans 2011–2017 (State of California 2018). The wind data for Argentina were acquired from Bridges et al. (2015), which were collected from March to November 2013. The anemometer used in their study was located at Salar de Incahuasi, 45 km northwest from the megaripple stripe field site at Abra Pomez. These data are currently the most reliable estimate of wind speeds available for the area.

B.2. Repton Score Model

Given that grain size data and wind data were available for Argentina and Oceano, a simple model was developed to compare the fluid thresholds of the grains present on the surface to the transport capacities of the wind. Using Equations 2 and 3 presented above, wind speeds necessary to initiate transport of grains was determined for all observed grain sizes. This yields a probability density function of the fluid thresholds for the grains. A probability density function of the observed maximum daily gust speeds was also created for the data from Oceano and Argentina. These two distributions can be used to generate a ‘repton score’ for any given grain size by determining the probability that that grain size will not have its transport threshold exceeded by the maximum gust on any given day:

$$RS_x = P(u_{tx} > u) \quad [11]$$

where u_{tx} is the transport threshold of a given grain size x , and u is the maximum daily gust. The repton score is the cumulative frequency of threshold values of surface grains greater than a given wind speed. As grain size data are typically collected as discrete, binned categories, the mean repton score for an entire sample acquired can simply be calculated as the weighted mean repton score for all n grain size bins x in a sample:

$$RS = \frac{\sum_{x=0}^n w_x RS_x}{\sum_{x=0}^n w_x} \quad [12]$$

where w_x is the percentage mass, or count depending on the nature of the data, of the given grain size bin. The sum of the weights is normalized to 1. In the case of photosieved data for which individual grain sizes are known, a simple arithmetic mean can be calculated in place of the weighted mean.

A sample from which all grains would be transported by every observed maximum daily gust would have a repton score of 0. Conversely, a sample from which all grains would never be transported by every observed maximum daily gust would have a repton score of 1. Note that any available wind data could be used to calculate the repton score, but maximum daily gust has been found to especially highlight the difference between samples used in this thesis. Standardization of wind measurements and sediment transport for the purposes of understanding aeolian sediment transport remains an issue in aeolian research (Barchyn et al. 2014). Because of this, repton score is presented as a relative metric and does not purport to quantify the true nature of transport on a surface. Repton score is not intended to be equivalent to other metrics such as drift potential or flux equations. Rather, its purpose is to convey a simple statistical distinction between several sediment samples paired to the same wind data.

B.3. Repton Score Results

The calculated fluid threshold probability density curves for both smaller bedform and megaripple corridors at the Oceano Dunes and Abra Pomez, along with observed maximum daily gusts,

are shown in Figure B.1 and Figure B.2. The results of the repton score probability model are shown in Figure B.3 and Figure B.4. The separation between the two curves demonstrates the relative frequency with which surface grains on megaripple and smaller bedform corridors are transported, showing that the latter are far more active than the former at both locations. Although the repton score is limited in its capacity as a direct estimate of sediment transport, the results suggest that there is, relatively, much more transport at the Oceano Dunes than at Abra Pomez. The results suggest that the repton score cumulative frequency graphs for megaripple corridors have an exponential curve and the smaller bedform corridors a logarithmic curve. The area between these curves represents a ‘transport behaviour gap’ that effectively summarizes the distinction between the reptation-dominant megaripple corridors and the saltation-dominant smaller bedform corridors.

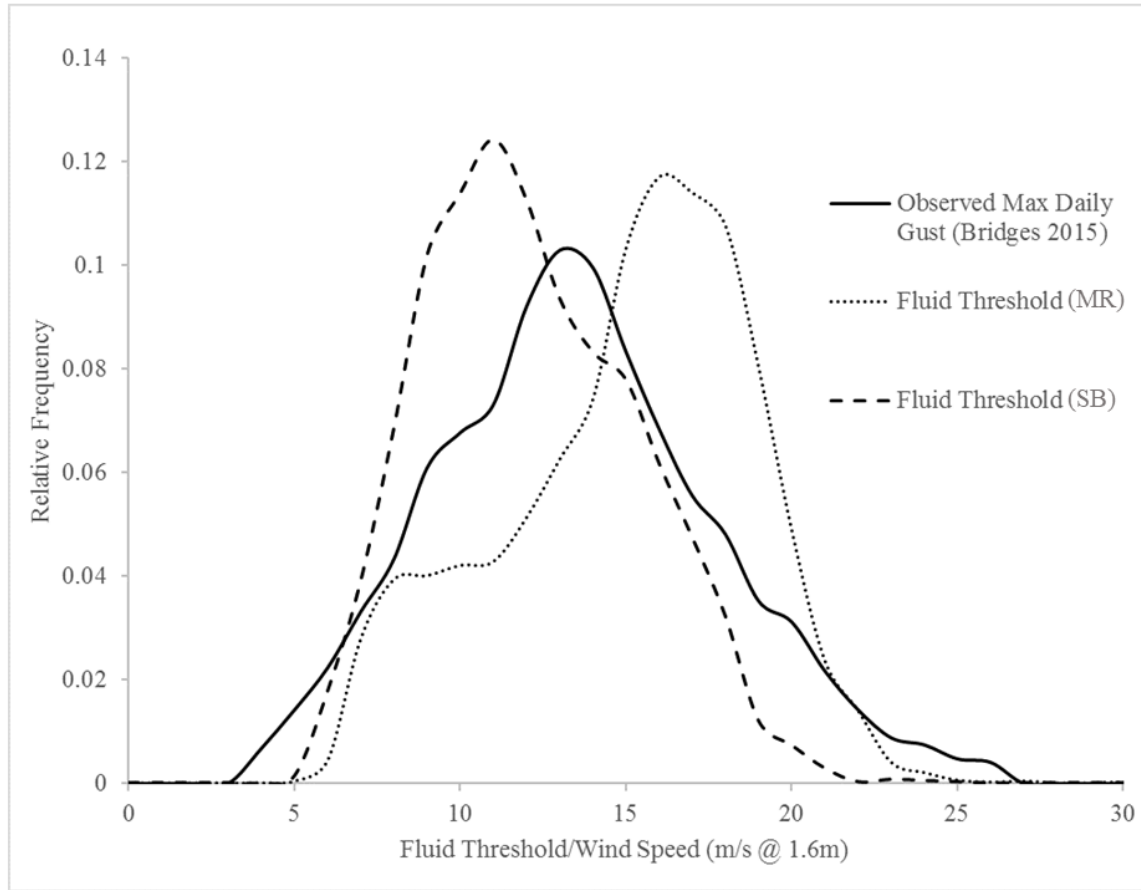


Figure B.1: Wind speed thresholds of the observed surface grain size distribution on the megaripple and smaller bedform corridors from photosieved data and the observed maximum daily gusts collected at an anemometer height of 1.6 m by Bridges et al. (2015).

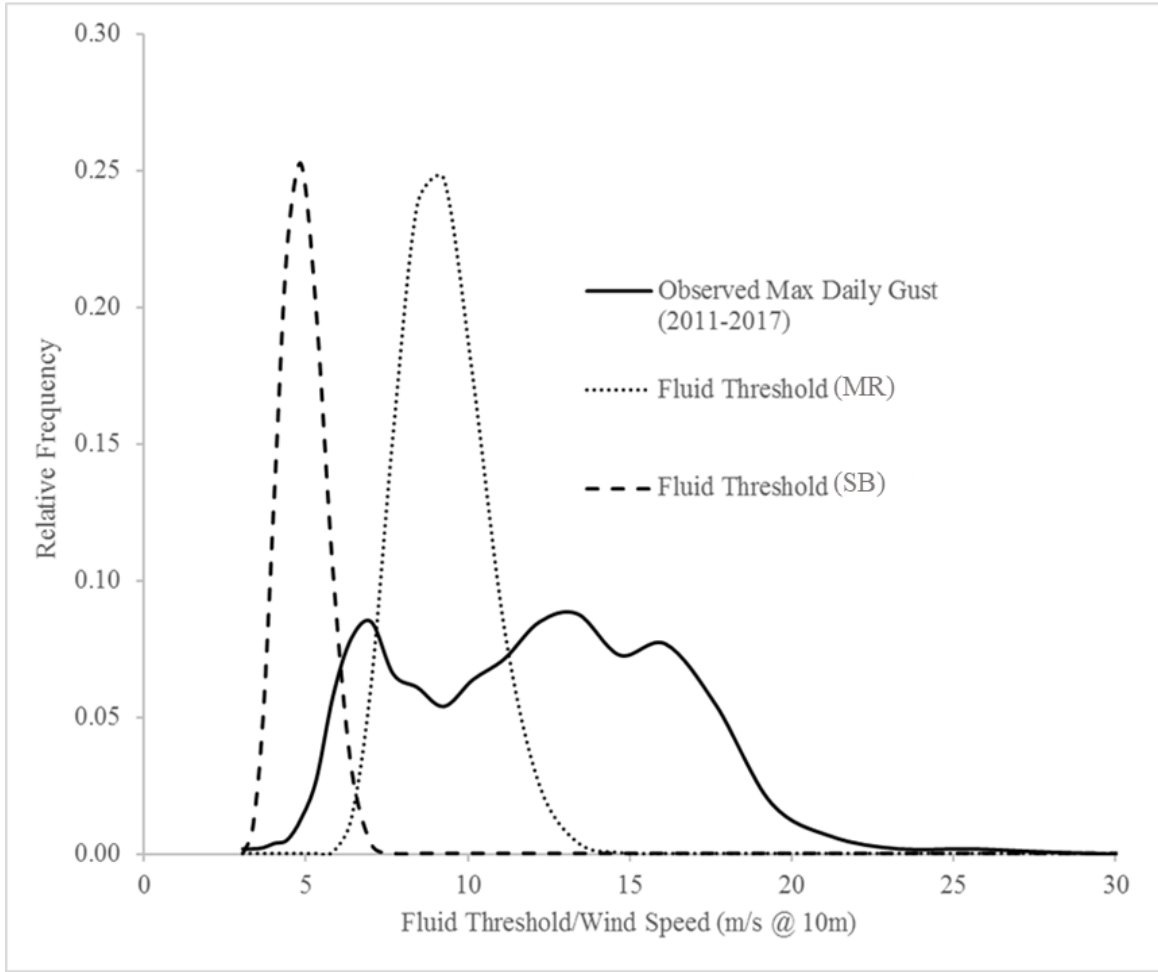


Figure B.2: Wind speed thresholds of the observed surface grain size distribution on the megaripple and smaller bedform corridors from LPSA data gathered from samples at megaripple stripe site C (1 cm depth) and the observed maximum daily gusts collected from State of California (2018). These data offer some similarity to the findings of Adhikari (2017), who observed transport events occurring between 5.18 and 8.49 m/s.

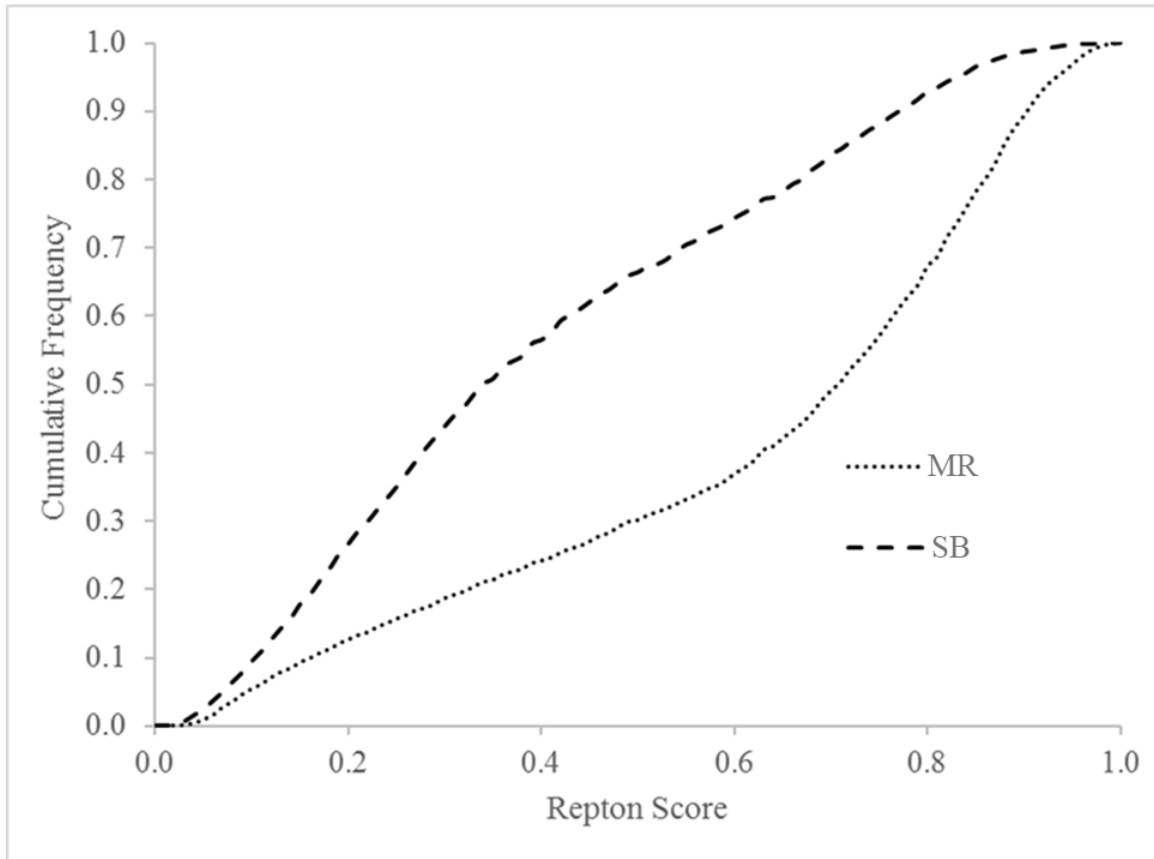


Figure B.3: Cumulative frequency of repton score distribution for the megaripple and smaller bedform data from Argentina. The area between the curves is a 'behaviour gap' that represents the difference in the nature of transport between corridor types.

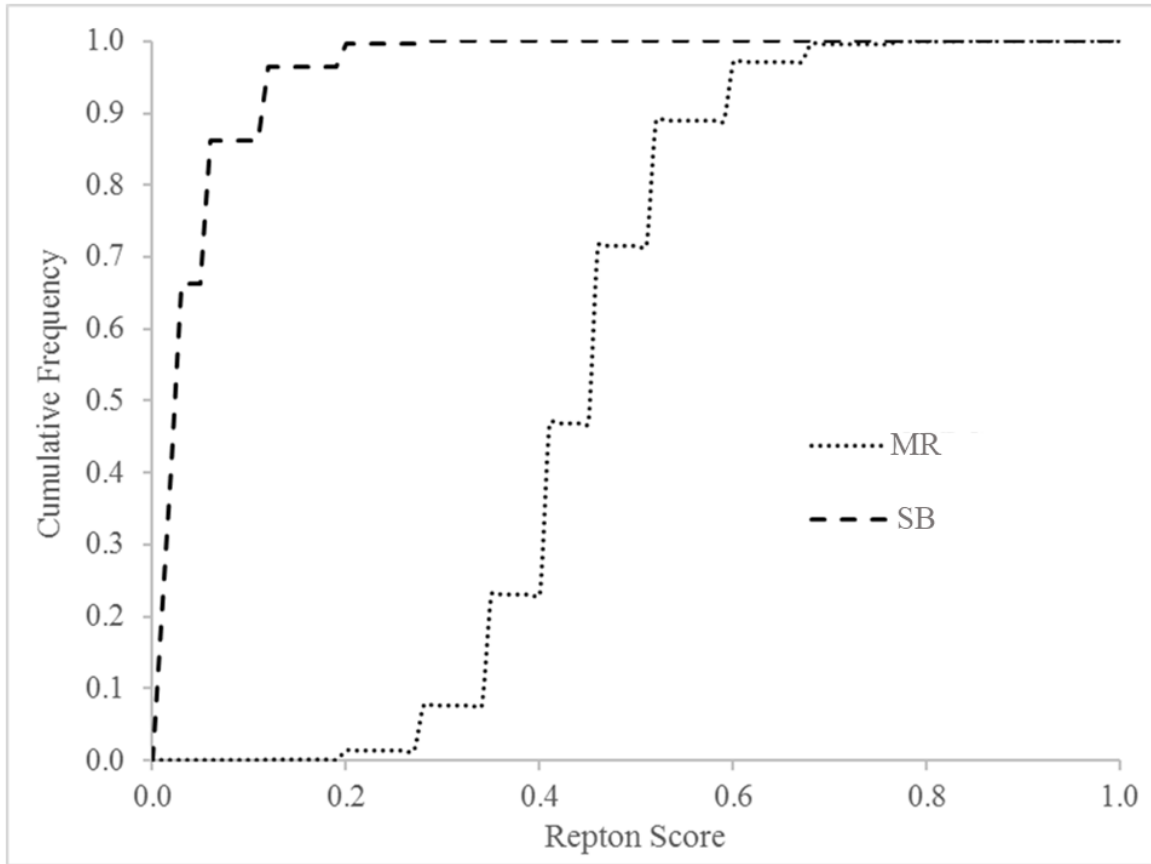


Figure B.4: Cumulative frequency of repton score distribution for the megaripple and smaller bedform data from Oceano. The rapid rise of the smaller bedform curve shows that the majority of the surface grains in these corridors is likely to have their fluid thresholds exceeded by the maximum daily gusts on more than 90% of days.